Unusual Retrograde Condensation and Asphaltene Precipitation in Model Heavy Oil Systems Using X-ray Imaging

by

Jalal Abedi

A thesis submitted in conformity with the requirements
for the degree of Doctor of Philosophy
Graduate Department of Chemical Engineering and Applied Chemistry
University of Toronto

National Library of Canada
Acquisitions and Bibliographic Services
395 Wellington Street
Ottawa ON K1A 0N4
Canada

Bibliothèque nationale du Canada
Acquisitions et services bibliographiques
395, rue Wellington
Ottawa ON K1A 0N4
Canada

Your file Votre référence

Our file Notre référence

0-612-35093-2

Canada

ABSTRACT

Unusual Retrograde Condensation and Asphaltene Precipitation in Model Heavy Oil Systems Using X-ray Imaging

Ph.D. 1998

Jalal Abedi

Graduate Department of Chemical Engineering and Applied Chemistry

University of Toronto

In this thesis, an accurate partial phase diagram for the model heavy oil system athabasca bitumen vacuum bottoms (ABVB) (24.6 wt. % / 2 mole %) + dodecane (73.8 wt. % / 47 mole %) + hydrogen (1.6 wt % /51 mole %) was constructed in the temperature range 425 K to 725 K and the pressure range 2 MPa to 7 MPa using a novel x-ray view cell apparatus. This model heavy oil fluid system is shown to exhibit L_1V and L_1L_2V phase behaviour over parts of this P-T region. The phase boundaries separating these regions are shown to be reversible within 2 K and 0.03 MPa. The shape of the low temperature boundary between the L_1V and L_1L_2V zones is characteristic of dilute asymmetric mixtures where on

isothermal compression a heavy liquid phase, L_2, appears then disappears within the light liquid phase, L_1. Such phase behaviour is referred to as unusual retrograde condensation and is of both practical and theoretical interest. For this mixture the retrograde condensation extends over a 75 K and 2 MPa temperature and pressure range, respectively. This is only the second reported large scale example of such phase behaviour.

Of equal importance is the finding that irreversible phase transitions involving asphaltene precipitation arise within the L_1L_2V region and not in the L_1V region - even at higher temperatures. Transitions between the multiphase regions were found to be reversible at temperatures less than 655 K, in all cases. At higher temperatures irreversible "asphaltene precipitation" arose within the L_2 phase. "Asphaltene precipitation" did not arise in the absence of the L_2 phase, i.e.: within the L_1V region, even at temperatures in excess of 700 K. These data provide a strong link between "asphaltene precipitation" and multiphase behaviour, and demonstrate a physical rather than a purely kinetic basis for asphaltene precipitation at elevated temperatures. This result compels one to rethink the approach to the modelling of such systems from both a phase behaviour and reaction kinetics perspective.

A third important result for this work is the development of a variable volume view cell suitable for studying the phase behaviour of opaque hydrocarbon systems and other systems. This device, created in collaboration with D. B. Robinson Ltd., greatly simplifies phase behaviour experiments and allows one to work with small volumes of fluid over a broader range of temperatures and pressures (0.1-27.5 MPa, 290-750 K). The apparatus is being considered for commercialization.

ACKNOWLEDGMENT

This project would not have been a success without the assistance and support of many people. Professor John Shaw, my Thesis Supervisor, stood by me and never gave up hope in me, especially during the most difficult periods of my studies. I would like to thank him for his insight, encouragement, and support throughout this entire project. Professors Jane Phillips and Charles Mims had sympathetic ears, gave most constructive criticism, and had my best interests at heart at all times.

Thanks also go to Professor Ali Mansoori for his helpful discussions and constructive suggestions. Without the help of my colleagues in our research group this undertaking would not of have been as much fun. I thank all my colleagues Leisl, Homayoun, Soheil, and Clive. The members of the Support Staff of the Department of Chemical Engineering especially Jackie Briscoe, Julie Mendonca, Dan Tomchyshyn, Leticia Gutierrez, and those in the machine shop also receive my thanks for their seemingly inexhaustible help.

Love to my wife, Cimin, my son, Armin, whose company, patience, and tolerance through the last few years have made this thesis possible.

As always, I am in debt to my parents and my sisters for their sacrifices and for giving me the opportunity to pursue higher education. Their inspiration and incessant moral support have proven invaluable for the success of this work.

I gratefully acknowledge financial assistance from CANMET -ERL, the NSERC Postgraduate Scholarship Program, and the Ontario Graduate Scholarship Program.

TABLES OF CONTENTS

LIST OF FIGURES

LIST OF TABLES

List of Symbols

C	Number of components
C_A	Concentration of A, mol . cm^{-3}
D	Dispersed phase
E	Energy of incident beam, keV
E_{act}	Energy of activation, cal. mol^{-1}
F	Degree of freedom
G	Gibbs free energy
h_c	Abbreviation for n-decylbenzene
I_o	Intensity of the incident beam
k	Number of phases critical
k_i	Reaction rate constant for case i, $(mol/cm^3)^{1-n}$ $.s^{-1}$
K point	point where L_1 and V become critical in the presence of L_2
L_1	Light liquid phase
L_2	Heavy liquid phase
L point	point where L_1 and L_2 become critical in the presence of V
m_i	Mass of component i, g
M	Molecular Mass, $g.mol^{-1}$
n	Order of reaction
P	Pressure, Pa
r_A	Rate of reaction, moles A formed.cm^{-3}. sec^{-1}
R	Universal gas constant, 8.314 m^3 Pa .mol^{-1} K^{-1}

S	Solid phase
T	Temperature, K
T_b	Boiling temperature, K
T_c	Critical temperature, K
T_r	Reduced temperature, T/T_c
v_i	Volume fraction of component i
V	Vapour phase
W_i	Weight fraction of element i
x_i	Mole fraction of component i

Greek letters

ρ	Density, g. cm^{-3}
λ	Wavelength of x-ray beam, nm
λ_e	Effective wavelength of polychromatic X-ray beam, nm
μ	Mass absorption coefficient,
μ_i	Chemical potential of species i
π	Number of phases

Subscripts

c	Critical property
i	Component number
j	Component number

Chapter 1

INTRODUCTION

1.0 Introduction

Over forty years ago, A. W. Francis, 1954 [1] stated that quantitative data are meager for the mutual solubilities of liquid carbon dioxide and other liquids. He then provided numerous examples of the wealth of multiphase liquid-liquid-vapour phase behaviour that occurs in systems containing carbon dioxide. His goal was solvent extraction, i.e., the exploitation of the separability of species between carbon dioxide-rich and carbon dioxide-lean liquid phases [2]. Since that time the occurrence of multiphase behaviour has become an important consideration in the design and operation of many processes.

For many chemical processes and separation operations that are conducted at high pressures, knowledge of pertinent phase behaviour is of special interest. There are many ways to obtain information about the phase behaviour of fluid mixtures. The direct measurement of phase equilibrium data remains an important source of information. Experimental equilibrium data are important, even when thermodynamic models are used to calculate the phase behaviour of a mixture (experimental data are always needed to obtain or to adjust interaction parameters within thermodynamic models).

Limited supplies of light, conventional crude oils have forced the petroleum industry, worldwide, toward the exploration, drilling, production and processing of heavy oils and bitumen. Unfortunately, many of these heavy crude oils are rich in asphaltenes which are often

responsible for major problems in production and processing. For example, downtime, cleaning and maintenance costs are considerable factors in the economics of producing crude oils from reservoirs prone to asphaltene deposition. In order to deal more effectively with the problem we need to be able to control asphaltene precipitation with some confidence.

Asphaltene deposition problems are often encountered during miscible flooding of petroleum reservoirs by carbon dioxide, natural gas and other injection fluids. In general, the introduction of a miscible solvent in a reservoir alters the system thermodynamics and reservoir rock characteristics. One major change is asphaltene precipitation which affects productivity by causing plugging or a reversal of wettability in the reservoir. Asphaltene problems are not, however, limited only to petroleum reservoirs. Deposition may occur on the well site, in wells, tubing, or piping, or in any of the refinery vessels used to upgrade the crude oil.

There has been growing interest in the processing and fractionation of petroleum residues such as vacuum bottoms which contain nearly 40 % asphaltenes [3]. Active areas include selective removal of fractions with a high heavy metal content, and the separation of asphaltenes or some fraction of asphaltenes from otherwise readily processed fluids. One of the viable commercial resid upgrading technologies, catalytic hydrogenation, has been used to convert vacuum resid to lower-boiling products without generating large coke yields. Regrettably, hydrogenation catalysts deactivate quickly with organic deposits and the reactors and associated equipment eventually clog with organic deposits [4]. As a result of this and the remedial measures imposed industrially which limit reactor throughput, the economics of resid hydrogenation are less attractive than expected, Figure 1.0.1 [5,6].

Phase behaviour is a key starting point in the search for solutions to these problems. Asymmetric hydrocarbon mixtures such as those found in hydrogenation processes exhibit multiphase behaviour [7-13] and such multiphase behaviour has been linked to fouling problems through the deposition of second liquid phases which can react to form coke [11-13].

This was shown in the pioneering work of Dukhedin-Lalla [12], e.g. Figure 1.0.2, where the multiphase region of a model heavy oil intersects the processing region for real heavy oil upgrading. Her data were largely qualitative in nature, and raised a number of issues including whether all of the phase transitions observed were reversible. However, bulk

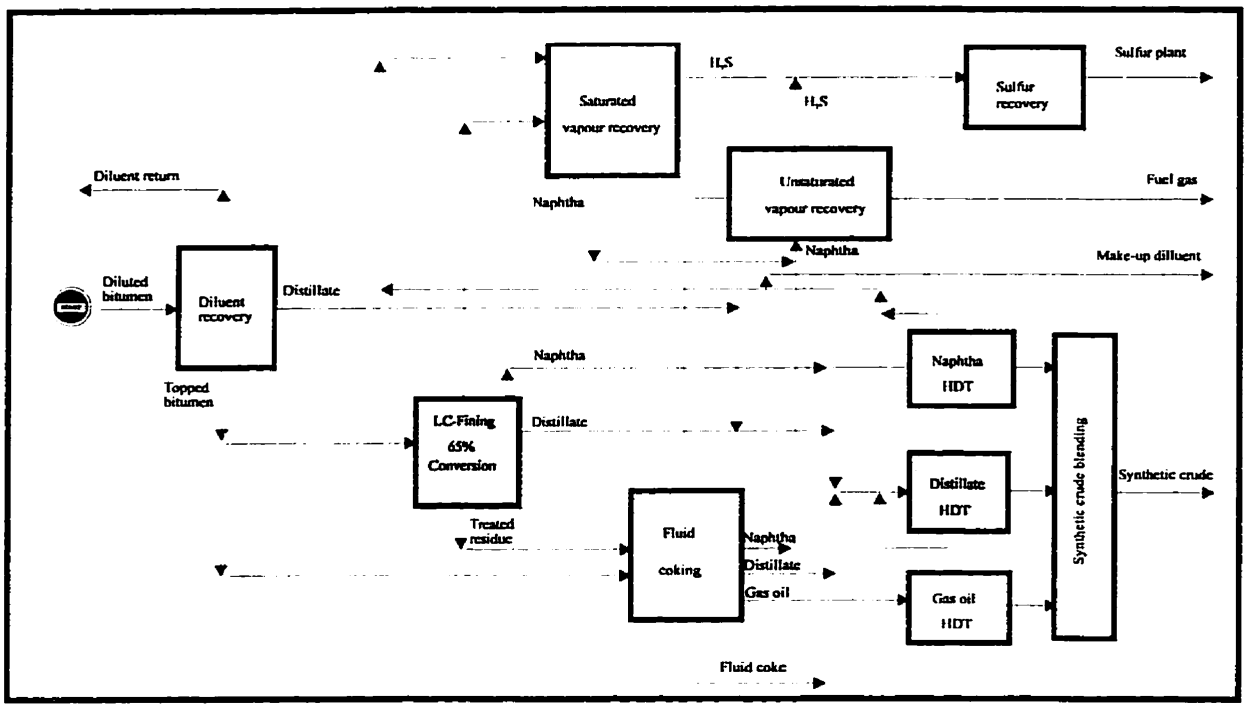

Figure 1.0.1 Schematic for the LC-Fining hydrogenation process, Syncrude Canada Ltd. [6].

asphaltene phases were among the phases observed and this result links with the work of Weihe [14,15] and Storm et al. [16,17] who observe a transition from colloidal or micellular asphaltene phases to bulk asphaltene phases at below ~ 670 K.

1.1 Objectives

This thesis constitutes an effort to move from qualitative to quantitative assessment of the phase behaviour of asymmetric mixtures of aromatic and paraffinic hydrocarbons relevant to heavy oil processing. Liquid-liquid-vapour and other multiphase behaviour are common phenomena in the critical and subcritical region of such mixtures and it is these conditions that are the focus of this study. The main aims of the thesis are to improve and simplify the apparatus employed previously and to categorize the phase behaviour of model heavy oils in the presence of light gases as a step toward quantitative modeling of the phase behaviour of

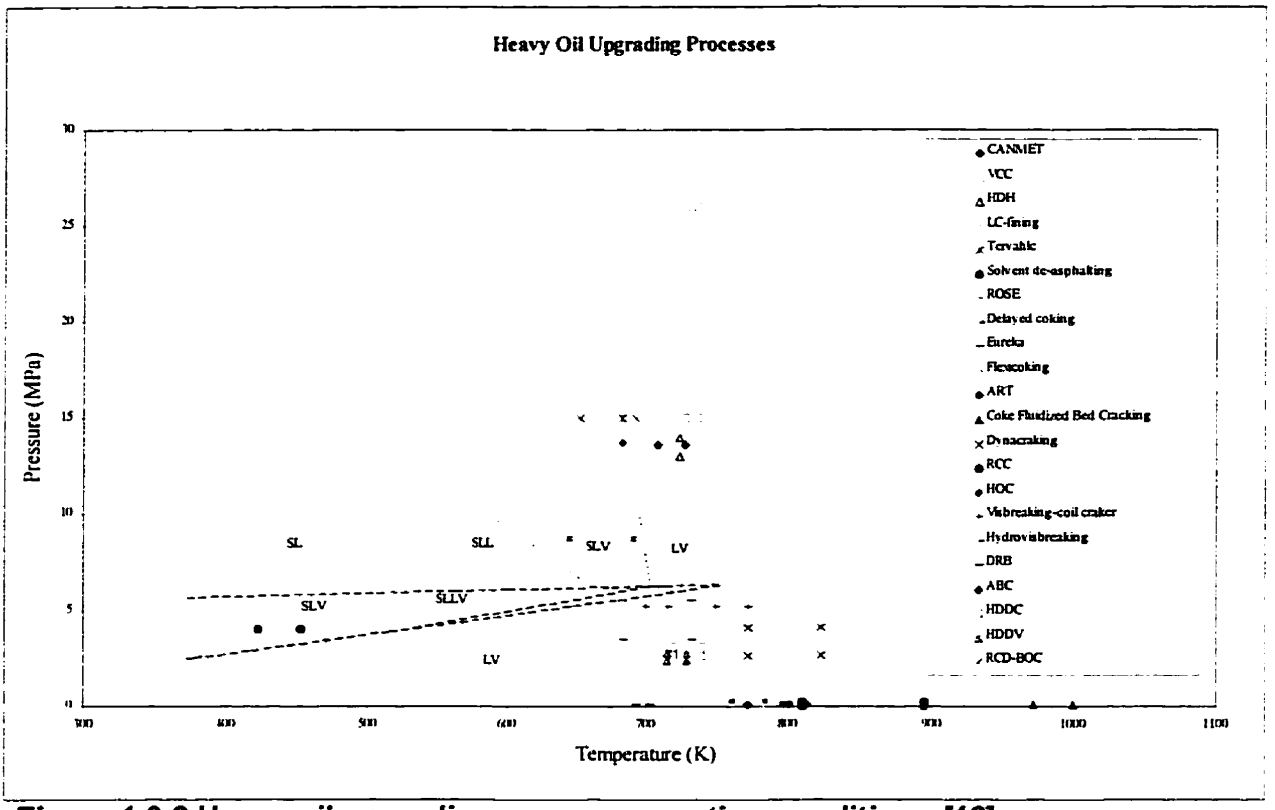

Figure 1.0.2 Heavy oil upgrading process operating conditions [12].

bitumen and heavy oil mixtures. Previous studies [12] have shown that Athabasca bitumen vacuum bottoms + dodecane in the presence of hydrogen exhibit liquid-liquid-vapour-solid phase behaviour at elevated temperatures and pressures. The specific objectives of this work are:

- to observe and quantify the phase behaviour of the system athabasca bitumen vacuum bottoms (ABVB) (24.6 wt. % / 2 mole %) + dodecane (73.8 wt. % / 47 mole %) + hydrogen (1.6 wt % /51 mole %) among others,
- to link observed phase behaviour of heavy oil/bitumen containing mixtures to simple but realistic physical model(s) for phase behaviour,
- to distinguish reversible from irreversible phase behaviour transitions.

- to meet the thermodynamic objectives above it is essential to improve the experimental technique:
  (a) by improving the image quality so that quantitative phase density data can be obtained (densities data allow one to distinguish L_2V from L_1V phase behaviour),
  (b) by developing a small variable volume view cell (facilitates experiments, reduces fluid required).

1.2 Outline of the Thesis

In Chapter 2 background materials that are necessary for the understanding and appreciation of this thesis are presented. In Section 2.1 the Gibbs phase rule is discussed in detail. For an understanding of the fundamentals of processing with near-critical fluids, a thorough knowledge of the phase behaviour of the mixtures involved is necessary. This topic is discussed in Sections 2.2 and 2.3. The different types of fluid phase behaviour are identified and the transitions among them are discussed. In Section 2.4 the basic features of fluid phase equilibria in ternary mixtures are addressed briefly. The retrograde condensation phenomenon is discussed in section 2.5. The importance and relevance of these reviews becomes clear in Chapter 5 where experimental results are discussed .

The x-ray imaging apparatus which was used in the experiments is described in Chapter 3. Details of the general layout, experimental setup, calibrations, and challenges are also provided. Our experience with the previous experimental set-up revealed that for reliable density measurements, the image quality must be improved. Further, an improved image quality would enable us to distinguish phases with very small density differences (less than 0.04 g/cm^3). Sections 3.1, 3.2 and 3.3 concern the calibration of the improved view cell facility. The procedure followed for the preparation of the mixtures is also outlined. The way the measurements are performed is discussed in Chapter 3. This Chapter closes with information on the chemicals that were used.

One of our more important achievements has been the development of a variable volume view cell suitable for studying the phase behaviour of opaque hydrocarbon systems (Chapter 4) which is installed in our laboratory. This device, created in collaboration with D.

B. Robinson Ltd., will greatly simplify our experimental program and allow us to identify critical phenomena directly and to operate with much smaller samples of fluid.

The results of the phase equilibria studies with a series of model heavy oil mixtures are reported in Chapter 5. Work on phase behaviour showed that retrograde condensation can occur at elevated temperatures. Retrograde condensation of a heavy liquid phase in the presence of a lighter liquid phase and a gas phase is a very important phenomenon in the field of reservoir engineering and has been researched by others [9]. This understanding is exploited in the interpretation of the data obtained as part of this study. The experimental work and results which are related to this phenomenon are presented in Chapters 3 and 5, respectively and summarized in the form of a paper for publication[1]. The issue of reversible versus irreversible phase behaviour is addressed in Section 5.2. Results from our recent efforts to identify parameters suitable for modelling the complex phase behaviour of vacuum bottoms + diluent + hydrogen mixtures are reported in Section 5.10. Finally, conclusions and recommendations are drawn in Chapters 6 and 7.

[1] It was presented at the recent AIChE Spring Meeting in Houston, March 1997, and will appear in a special issue of Petroleum Science and Technology later this year [18].

Chapter 2

BACKGROUND

2.0 Introduction

In this chapter, background materials that are necessary for the understanding and appreciation of this thesis are presented. In section 2.1 the Gibbs phase rule is discussed in detail. For an understanding of the fundamentals of processing with near-critical fluids, a thorough knowledge of the phase behaviour of the mixtures involved is necessary. This topic is discussed in section 2.2.

The classification scheme of van Konynenburg and Scott, 1980 [19] was the first systematic categorization of different types of fluid phase behaviour in binary systems. These authors predicted all the experimentally known types of phase diagrams using the van der Waals equation of state and revealed the mechanisms of transitions among these diagrams, when the characteristic parameters of the two components were changing. Section 2.3 contains a more detailed description of their work. A brief overview of complex phase behaviour in ternary mixture is also provided in Section 2.4. The retrograde condensation phenomenon is discussed in section 2.5 and the Chapter closes with x-ray sorption.

2.1 The Gibbs phase rule

Let us consider a system of C components distributed over π separate phases at equilibrium. In general each phase contains every component in a different proportion than any other phase containing the same component. Also the overall composition of the system is in general different from the specific composition of any phase. There are several variables which describe the equilibrated system. Following the definition of Griffiths and Wheeler, 1970 [20] we recognize as "fields" the variables having the same value for all the coexisting phases and as "densities" the variables which have a different value from phase to phase. Fields are the temperature, T, the pressure, P, and the chemical potentials of the various components, μ_i (i=1,2,...,C), which are identical in every phase. Densities are the compositions, x_i^j (i=1,2,...C and j=α, β,..., π), the mass densities, ρ^j, the molar volumes, V^j, the molar entropies, S^j, etc., which differ from phase to phase.

Let F be the number of independent field variables that are free to change while the system still contains the same number of components distributed over the same number of phases. The number F is often called the number of degrees of freedom of the system. Notice that F=2 implies that only two variables, such as T and P, or T and μ_1, or μ_2, and μ_3 etc. can be chosen as independent. The Gibbs phase rule determines F as

$$F=C-\pi+2 \qquad (2.1.1)$$

If k is the number of critical -with each other- phases then the Gibbs phase rule can be formulated [21] as

$$F=C-\pi-2k+2 \qquad (2.1.2)$$

In equation 2.1.2 π and k are counted as observable phases, i.e., a critical phase -no matter how many phases become critical together in this phase- is counted as 1; k=1 always for critical phases. According to equation 2.1.2 a L=V equilibrium in binary system (C=2,

π=1 and k=1) has F=2-1-2+2=1 degrees of freedom and a L_2=L_1-V equilibrium in binary system (C=2, π=2 and k=1) has F=2-2-2+2=0 degrees of freedom.

For F=0 the system is characterized as invariant; for F=1 the system is monovariant; for F=2 bivariant; etc.. For a unary system C=1 and therefore if π=1 then F=2. The single-phase equilibrium situations are represented by surfaces (dimensionally =2) on a P, T plane as depicted in Figure 2.1.1. This is also true for any other equivalent plane, for example, T, μ or P, μ. If π=2 then F=1 and the two-phase equilibrium states are curves (dimensionally =1) on the P, T plane. If we have only 3 single phases, the solid (S), the liquid (L) and the vapour (V), then there are three possible two-phase equilibria, the LV, the SL, and the SV equilibrium which are forming the vaporization, the melting, and the sublimation curve, respectively. If π=3 then F=0, which means that the system is invariant and there is a unique value for all the fields in order to achieve such an equilibrium case (SLV).

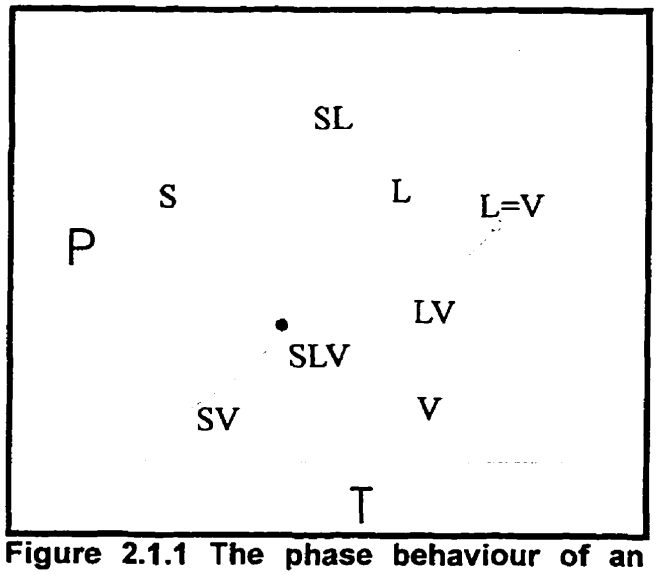

Figure 2.1.1 The phase behaviour of an unary system projected onto a P, T plane, •: triple point (SLV), ○: critical point (L=V).

This state is represented by a point (dimensionally =0) on the P, T plane, a triple point. Finally if π=1 but also k=1 (the state for a critical point) then F=0 again. The common

experimentally known case for such a state is the liquid-vapour critical point (L=V) of a single component system which terminates the vaporization curve.

For a binary system C=2 and, existing in a single phase, π=1 and F=3. In order to depict this case we need at least a three-dimensional field. A proper selection could be the P, T, μ space. In this space the one-phase equilibria will form closed volumes bordered by surfaces and curves which terminate these surfaces. Instead of the P, T, μ space, another popular and convenient but not equivalent space is the P, T, x space (x is the mole fraction of the less-volatile component, $x=x_2$).

In the case of the binary mixture, if the pressure, the temperature and the overall composition of the mixture are such that they determine a point inside the phase envelope (unstable point), then a phase split occurs creating two phases that are in stable equilibrium with each other. The compositions of these phases are such that the condition of equality of the chemical potentials of both components in the two phases is satisfied. These equilibrium points are situated on the two outer single-phase surfaces of the envelope and are connected by a straight segment which is called a tie-line.

For a binary system with π=1 and k=1, F=1. This is the case of critical points or critical locus (L=V) of a binary mixture. If we consider the liquid-vapour envelope of a binary system in the P, T, x space we already described how this is absorbed by the critical curve (L=V) towards high P and T. At extreme x values, x=0 or x=1, the same envelope terminates along the two pure component vaporization (saturation) curves where again x loses its dual character and the two outer surfaces, representing the liquid and the vapour, coincide. Towards the direction of low T the appearance of solid-liquid-vapour or liquid-liquid-vapour three phase equilibria terminates the liquid-vapour envelope in most cases. For a binary mixture with π=3, F=1. The three phase equilibria in a P, T, μ space are represented by a curve and in a P, T, x space by a set of 3 curves which enclose a surface (dimensionally F+1=2) of instability. When π=4 then F=0. This means that an equilibrium among four phases for a binary system is a nonvariant one and is represented by a point in the P, T, μ space or with a set of four points in the P, T, x space. This is the quadruple point.

2.2 Understanding Phase Diagrams

For an understanding of the fundamentals of processing with near-critical fluids and for the design of processes, a thorough knowledge of the phase behaviour of the mixtures involved is necessary. Often one is dealing with two-phase equilibria, i.e., solid-liquid or liquid-vapour equilibria, but also multiphase equilibria like solid-liquid-vapour or liquid-liquid-vapour equilibria play an important role. These equilibria are strongly influenced by pressure, temperature and the composition of these mixtures.

In order to predict qualitatively the phase behaviour of the system of interest at other than the experimental conditions, one should be aware of the basic concepts of phase diagrams and one should be aware of the possible types of phase behaviour. These predictions can help one to design additional experiments or to perform the right type of phase equilibrium calculations.

In practice mainly two-dimensional diagrams are used to represent phase equilibria. Projections of monovariant and invariant states on the P, T-plane and sections of P, T, x-space keeping one or more variables constant are most commonly used. For instance, for binary systems mainly P, x-sections at constant T and T, x-sections at constant P are used. Figure 2.2.1a gives the combined P, T and P, x-projections. Since in these projections only monovariant and invariant equilibria can be shown the information on the details of the two-phase equilibria are lost in the projections. The three phase equilibria, which in P, T, x-space are represented by three curves, are represented by one curve in the P, T-projection and by three curves in the T, x-projection. The reason for this is that at one temperature the three phases have different compositions but the same pressure, so in P, T-projection the three curves coincide. The P, T-projection also shows the two vapour-pressure curves of the two pure components. In the T, x-projection these curves are found along the axes x=0 and x=1. The critical curves are represented by a curve in both projections and the pure component critical points by a point. The critical endpoints are represented by one point in the P, T-projection and by two points in the T, x-projection.

Figure 2.2.1b represents schematically a two-phase equilibrium $\alpha\beta$ in a P, x-section. The Figure 2.2.1b shows two curves: the composition of phase α and of phase β as a function

of pressure. In Figure 2.2.1c the Gibbs energy as a function of composition is plotted for phase α and phase β at constant P and T. A common tangent can be drawn to both curves. These tangent points represent the coexisting phases α and β. It can easily be shown that for the tangent points the equilibrium condition $\mu^{\alpha}_{I} = \mu^{\beta}_{I}$ for I=1,2 is fulfilled [22]. In the left part of Figure 2.2.1c phase α is the stable phase since it has a lower Gibbs energy than phase β. In the right part of the diagram phase β is stable. Between the two common tangent points an equilibrium of phase α and phase β is more stable than homogeneous phase α or homogeneous phase β. The Gibbs energy of the two-phase equilibrium αβ is represented by the straight line through the two common tangent points, so the two-phase equilibrium always has a lower Gibbs energy than phase α or phase β. The consequence of this is that a mixture with a composition in between that of phase α and that of phase β will split into two phases with composition given by the curves $P(x^{\alpha})$ and $P(x^{\beta})$. To the left of the curve $P(x^{\alpha})$ there will be a region with the homogeneous phase α, to the right of the curve $P(x^{\beta})$ there will be a region with the homogeneous phase β.

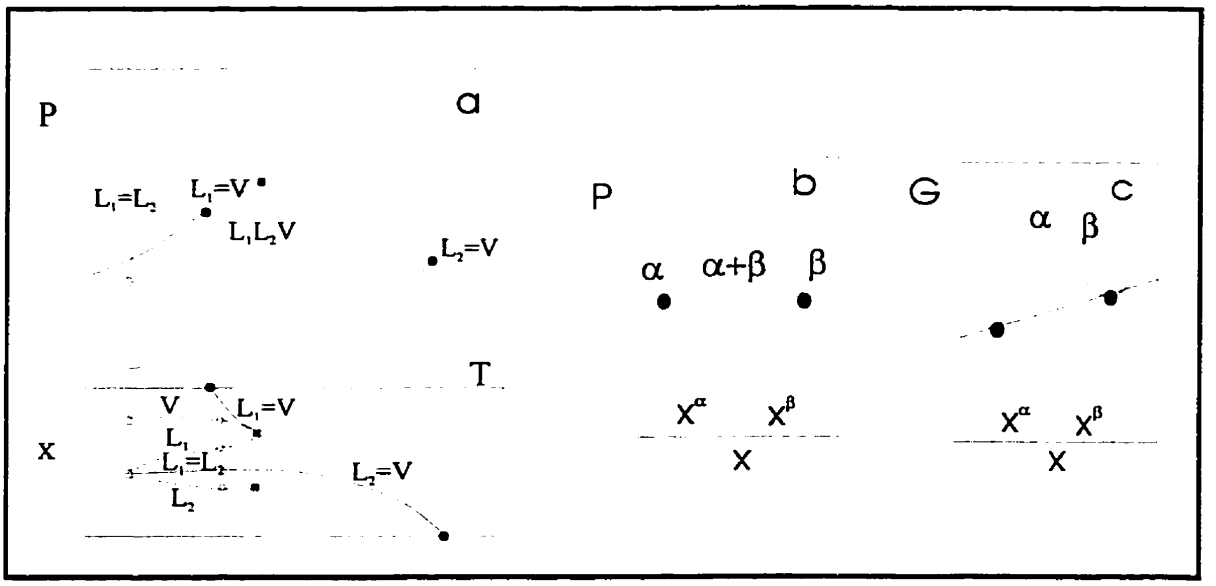

Figure 2.2.1 a: Combined P, T- and T, x-projections of type V fluid phase behaviour. b: P,x-section of a two-phase equilibrium αβ. Schematic. c: G,x-diagram for phases α and β at constant P and T.

2.3 Types of Fluid Phase Behaviour (The Classification of van Konynenburg and Scott [19])

In Figure 2.3.1a the projection of the P, T space for binary phase behaviour is shown. Instead of the three dimensional space its two dimensional projections and cross sections are used. The binary phase behaviour of Figure 2.3.1a is named type I in the classification scheme of van Konynenburg and Scott, 1981 [19]. In a type I system only one critical curve is found. This is the liquid-vapour critical curve L=V which runs continuously from the critical point of component 1 to the critical point of component 2. The two solid curves are the saturation curves or the vapour pressure curves of the two pure components. The dashed curve is the vapour-liquid critical curve of the mixture. Every point along that curve represents the critical points of a specific mole fraction from 0 to 1. In Figure 2.3.1b several isopleths are projected together with the saturation curves of the pure components and the vapour-liquid critical curve of the mixture. The isopleths are tangent to the critical curve at the critical point of the specific composition they represent. Inside an isopleth, for example $x=x_2$, at the point of conditions T^* and P^*, the mixture with that specific overall composition (x_2) exhibits vapour-liquid equilibrium. The high-pressure branch of the isopleth ending in the critical point is the bubble-point curve and the low-pressure branch starting at the critical point is the dew-point curve of the isopleth. For the isopleth $x=x_2$ at the equilibrium point (T^*, P^*) the vapour phase composition is x_1 because the dew-point curve of the isopleth x_1 is passing through the point (T^*, P^*) and the liquid phase composition is x_3 because the bubble-point curve of the isopleth x_3 is passing through the point (T^*, P^*). From the same point (T^*, P^*) it is not possible that any other bubble-point or dew-point curve passes because for a binary system the bubble or dew points of a specific composition are monovariant equilibria. If the temperature is fixed at T^* the pressure for a dew point with composition x_1 can only be P^* and the pressure for a bubble point with composition x_3 can only have the value P^*.

In Figures 2.3.1c and 2.3.1d some P, x- and T, x-sections are shown. In the T, x-sections the two-phase LV region has a reversed position compared with the P, x-section. Note that the T, x-section at P_2 shows two critical points, which is a consequence of the pressure maximum

of the critical curve in the P, T-projection. These pressure maxima are often found in type I systems.

In Figure 2.3.2a the P, T-projection of a type II system is plotted. Type II fluid phase behaviour has a continuous liquid-vapour critical curve just as in the case of type I. The difference between this type and type I bevaviour is the existence of a liquid-liquid immiscibility region at low temperatures. The liquid-liquid immiscibility region terminates along a liquid-liquid critical curve. The temperatures where the two liquid phases become indistinguishable are called upper critical solution temperatures (UCST's). The three phase L_2L_1V equilibrium curve terminates at a point where the two liquid phases are critical with each other. This point is an UCST and it is also the endpoint of the liquid-liquid critical curve. Therefore it is named upper critical endpoint (UCEP).

In Figure 2.3.2 four characteristic P, x-section are shown. At low temperature the P, x-sections show a L_2L_1V equilibrium. At higher pressure than the three-phase pressure the L_1V and L_2L_1 two-phase regions are found, and at lower pressure the two-phase region L_2V. With increasing temperature the compositions of the two liquid phases of the L_2L_1V equilibrium approach each other, as can be seen from the T, x-projection in Figure 2.3.2.

In Figure 2.3.3a the projections of a system with type III phase behaviour are depicted. In this binary system there is no continuous critical curve connecting the critical points of the two pure components. The critical curve starting from the critical point of the more volatile component finishes at a critical endpoint where a three phase L_2L_1V equilibrium curve terminates. This critical point is also an UCEP as in the type II behaviour, but the two critical phases are not the two liquids L_2 and L_1 but the vapour, V, and the liquid richer in the more volatile component, L_1 . In order to distinguish between these two UCEP's we characterize the type II UCEP as L_2=L_1 -V and the type III UCEP as L_2 - L_1=V. The critical curve starting from the critical point of the less volatile component goes to lower temperatures passing successively through a pressure maximum and a pressure minimum. Afterwards it turns back to higher temperatures and pressures.

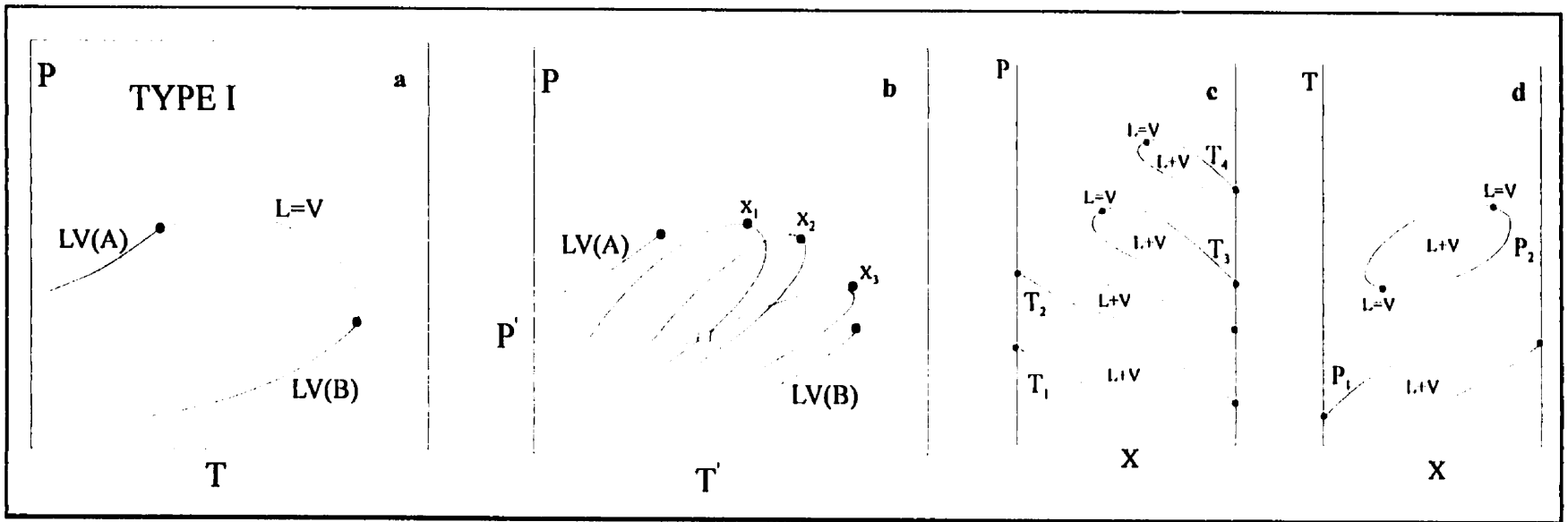

Figure 2.3.1 a: P-T projection of the monovariant fluid phase equilibria in binary mixtures of type I. b: P-T projection of the monovariant fluid phase equilibria for a type I binary system together with some selected isopleths. c: P,x-sections at constant T. d: T,x-sections at constant P.

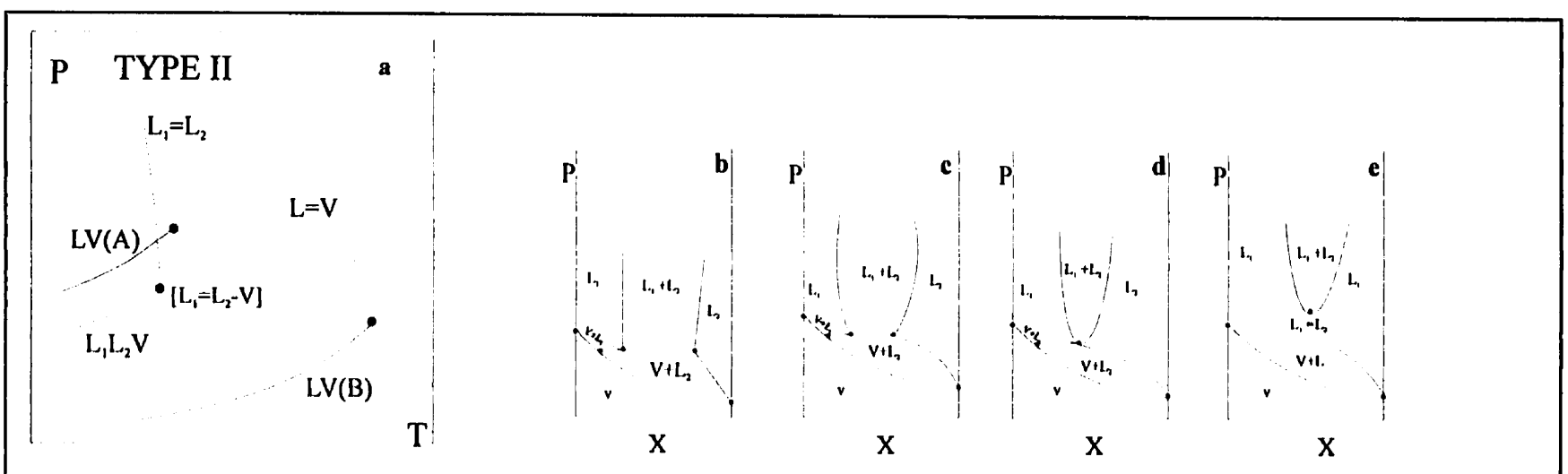

Figure 2.3.2 a: P-T projection of the monovariant fluid phase equilibria in binary mixtures of type II. b: P, x-sections at constant T. c:$T<(L_2=L_1V)$. d: $T=T(L_2=L_1V)$. e: $T(L_2=L_1V)<T<T(L=V)_{x=0}$.

In Figure 2.3.3b the projection for a type IV system is given. A type IV system shows like a type II system a L_2L_1V equilibrium curve with an UCEP [L_2=L_1 -V] but, in addition, at higher temperatures a second branch of the L_2L_1V equilibrium curve is found. Also in this type there is no continuous vapour-liquid critical curve. The branch of the critical curve starting from the critical point of the more volatile component finishes at an UCEP [L_2 -L_1 =V] of the high temperature branch of the L_2L_1V equilibrium curve as in type III. The branch of the critical curve originating from the critical point of the less volatile component goes to lower temperatures via a pressure maximum and ends in a lower critical endpoint of the high temperature branch of the L_2L_1V equilibrium curve where two liquid phases are critical with each other in equilibrium with the vapour phase. This critical endpoint is not the same as the UCEP [L_2=L_1 -V] of the type II behaviour. In this case the two liquids become critical with each other upon a temperature reduction, instead of a temperature increase as is happening in a type II system. Therefore this critical endpoint is characterized as a lower critical endpoint (LCEP) in contradiction to the upper critical endpoint of the type II behaviour. These UCEP and LCEP limit the high temperature branch of the L_2L_1V equilibrium curve in a type IV system.

The phase behaviour of the type V system is presented in P-T space in Figure 2.3.4a. The type V system may be considered as a special case of the type IV system where the lower branch of the three-phase equilibria as well as the related liquid-liquid immiscibility region has been shifted to negative temperature. Characteristic for this type of phase behaviour is a three-phase equilibrium L_2L_1V with a LCEP L_2 =L_1 -V and a UCEP L_2 -L_1 =V, and a discontinuous critical curve. The first branch of the critical curve connects the critical point of the more volatile component with the UCEP. The second branch runs from the LCEP to the critical point of the less volatile component.

In Figure 2.3.4, four P,x-sections are shown at temperatures $T(L_2=L_1-V) \leq T \leq T(L_2-L_1=V)$. At lower and at higher temperatures the P, x-sections are comparable with those of type I systems. In Figure 2.3.4c a P,x-section is shown at a temperature between the LCEP and the critical point of the more volatile component. On lowering the temperature, the composition of

the L_2 phase and of the L_1 phase of the L_2L_1V equilibrium approach each other and the pressure of the $L_2=L_1$ critical point approaches the three phase pressure. At the temperature of the LCEP (see Figure 2.3.4b) the L_2 and L_1 points of the three phase equilibrium and the critical point $L_2=L_1$ coincide. The L_2L_1 two phase region disappears and the L_1V and L_2V two phase regions join in one LV two phase region. The LV region shows a horizontal point of inflection at $L_2=L_1$ critical point. At higher temperatures of Figure 2.3.4c the L_1V region will detach from the axis x=0 (Figure 2.3.4d) and at even higher temperatures the composition of the L_1 phase and of the vapour phase of the L_2L_1V equilibrium approach each other. At the temperature of the UCEP the L_1 and V points of the three phase equilibrium and the $L_1=V$ critical point coincide (Figure 2.3.4e). At this temperature the L_1V two phase region disappears and the L_2V and L_2L_1 two phase regions again join in one LV two phase region.

If a third, miscible component, is added to a type V binary, the K-point and L-point will move to higher temperatures and converge at the tricritical point. At the tricritical point all three phases become critical with each other; ($L_2=L_1=V$). However, if the third component is immiscible with either of the binary pair, the K-point and L-point will diverge to lower temperatures and the size of the three phase region will become larger. If the third component is immiscible with both binaries, the divergence effect will be much more drastic.

Type VI phase behaviour demonstrates three phase equilibrium L_1L_2V with a LCEP $L_2=L_1-V$ and a UCEP $L_2-L_1=V$. In Figure 2.3.3c the LCEP and UCEP are connected by a $L_2=L_1$ critical curve which shows a pressure maximum. Another possibility is existence of a second $L_2=L_1$ critical curve at high pressure with a pressure minimum. This phenomenon is called high pressure immiscibility. Also the low pressure immiscibility region and the high pressure immiscibility region can be combined in one uninterrupted L_2L_1 region [23].

From the collection of P-x at constant temperature diagrams by turning them at their edge and taking the plane through them, P-T at constant composition diagrams can be constructed. An example is shown in Figure 2.3.4 for a type V binary when the composition asses for P-x. P-T at constant composition diagram is the one typically employed because normally, experiments are constructed over a range of pressures and temperatures at constant composition. This is the so-called synthetic method. In our treatment of ternary diagrams we go directly to a P-T at constant composition diagram without the intermediate construction itself.

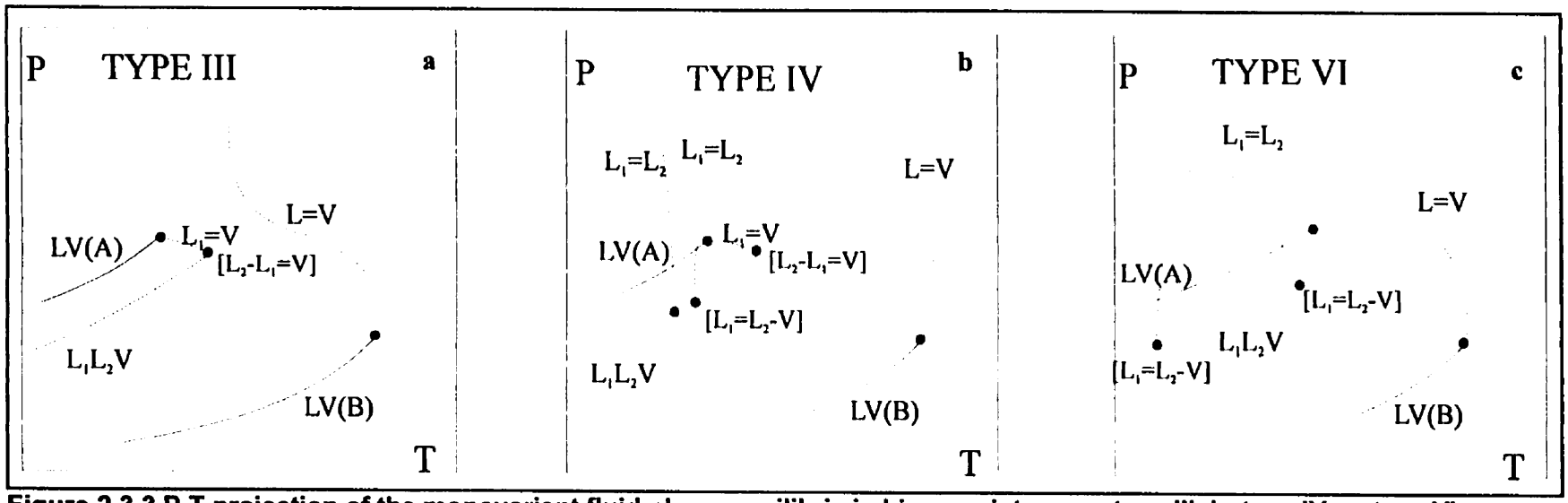

Figure 2.3.3 P-T projection of the monovariant fluid phase equilibria in binary mixtures a: type III. b: type IV. c: type VI.

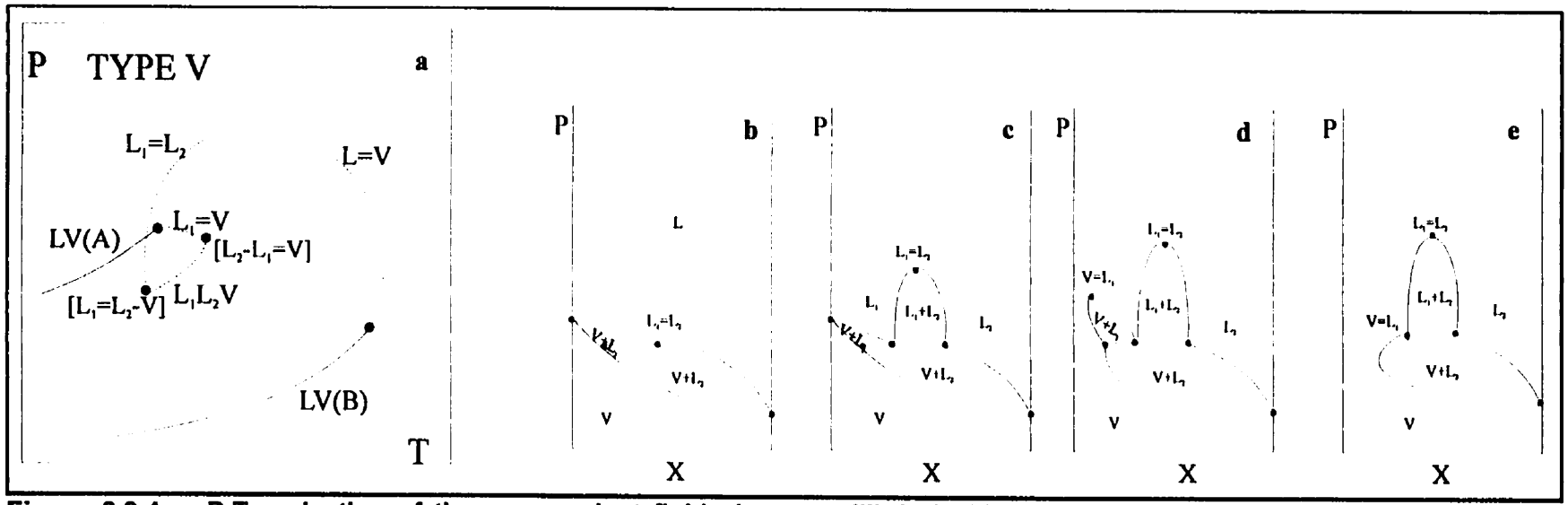

Figure 2.3.4 a: P-T projection of the monovariant fluid phase equilibria in binary mixtures of type V. b: P, x-sections at constant T. $T=T(L_2=L_1V)$. c: $T(L_2=L_1V) < T < T(L=V)_{x=0}$. d: $T(L=V)_{x=0} < T < T(L_2L_1=V)$. e: $T=T(L_2L_1=V)$.

2.4 Ternary Mixtures

The classification scheme of phase behaviour for binary fluids as proposed by van Koynenburg and Scott [19] provides a sound basis for understanding the phase behaviour of more complex mixtures. The interpolation of these six basic types of fluid behaviour has been utilized widely to predict and explain complex phase behaviour in systems with more than two components. One such example is the modelling of reservoir fluids [24,25], as found in the oil recovery processes, where retrograde phenomena have been addressed.

Retrograde condensation of a heavy liquid in the presence of a light liquid phase and a gas phase is an important phenomenon in reservoir engineering. In this situation, on decreasing the pressure at a constant temperature, the appearance and subsequent disappearance of a heavier liquid is observed in the three phase region (L_1L_2V). In order to explain this phenomenon a better understanding of the three phase region was needed.

Asymmetric binary mixtures of alkanes, which are models for oil recovery systems, with a heavy component (B) and a light component (A), have been shown to exhibit Type V phase behaviour [26] (see Figure 2.4.1). In type V phase behaviour a three phase region begins near the critical point of the light component A. It starts at a LCEP where component B rich heavy liquid phase (L_2) and component A rich light liquid phase (L_1) are critical in the presence of the gas and ends at the UCEP where the L_1 and the gas are critical in the presence of L_2. The critical curve is made up of two branches; one branch $L_1 = V$ which connects the critical point of component A to the UCEP and a second branch $L_1 = L_2$ which connects the critical point of component B to the LCEP.

As we now increase the number of components in this system from two to three the available degrees of freedom increase and, consequently, the L_1L_2V line becomes a region in the P-T space. Figure 2.4.1 shows the phase behaviour of an asymmetric binary mixture and Figure 2.4.2 a,b,c show the behaviour at mole fractions x_1, x_2 and x_3 where x is the mole fraction of the heavy component and $x_1 > x_2 > x_3$. For the highest concentration of the heavy component, x_1, the three-phase region starts at the point where the line x_1 =constant intersects the L_2 branch of the L_1L_2V curve and ends at the UCEP.

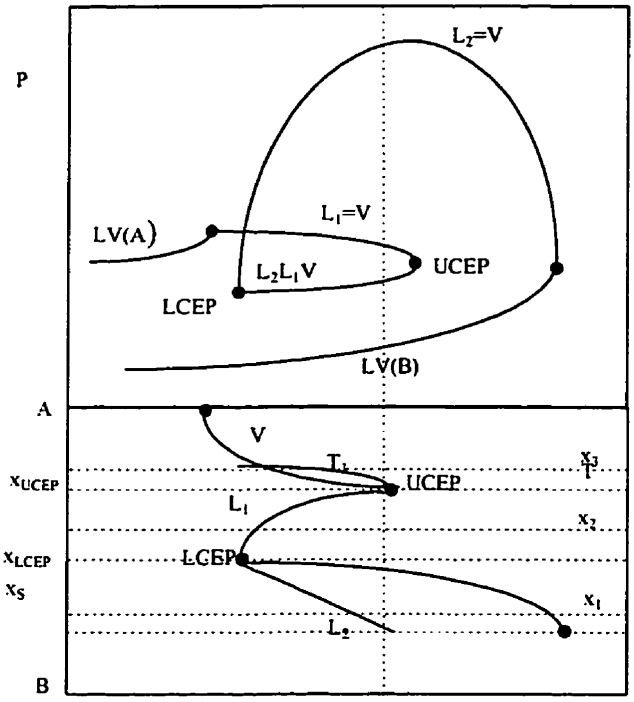

Figure 2.4.1 - Phase behaviour of asymmetric binary mixture showing Type V behaviour [24].

In this case only part of the L_1L_2V curve can be observed. For the mole fraction x_2 the whole L_1L_2V curve can be seen and for the mole fraction x_3 a part of the L_1L_2V curve can be seen. Figures 2.4.2 d, e and f show the expansion of this system to a ternary mixture where the third new component is miscible in both of the other two components. Notice that the L_1L_2V curve becomes a region. The addition of a miscible third component to a binary system has been shown [24] to shift the three phase region to higher temperatures and pressures. Furthermore, as the amount of the third component in the mixture increases, the L_2L_1V region shrinks. Eventually, the LCEP and the UCEP coincide at the tricritical point. In Figures 2.4.1 e and f phase diagrams the retrograde condensation of the heavier liquid L_2 is possible and appears in the vicinity of the LCEP.

If a third component which is immiscible in both constituents of the binary mixture is added then the three phase region is shifted to lower temperatures but higher pressures and

the L_1L_2V region is expanded. Figure 2.4.3 shows P-T diagrams of the binary mixture of n-decylbenzene + ethane with the addition of carbon dioxide (phase diagram I having the highest concentration of carbon dioxide and phase diagram IV showing just the binary). If the LCEP is present in the phase diagram with this particular mixture then retrograde condensation of the heavy liquid phase is possible. These findings were very significant and demonstrated that complex phase behaviour can be shifted in the pressure-temperature space by the addition of the appropriate component. For the present study, hydrogen acts in much the same manner as carbon dioxide except the three phase region would be shifted to higher pressures i.e., the pressure effect would be greater. The effect of adding light gases can be anticipated by looking at the critical temperature of the light gas. The critical temperatures of the following light gases are such that:

$$T_C\,(CO_2) > T_C\,(CH_4) > T_C\,(N_2) > T_C\,(H_2)$$

Hence, with n-decylbenzene + ethane + carbon dioxide, the three phase region is shifted to higher pressures and lower temperatures and the pressure "effect" and temperature "effect" are observed. As the critical temperature of the light gas decreases, the temperature "effect" is less dominant and the pressure "effect" becomes more dominant. If hydrogen replaces carbon dioxide as the light gas, the three phase region would be then shifted almost vertically up in pressure with very little shift in temperature.

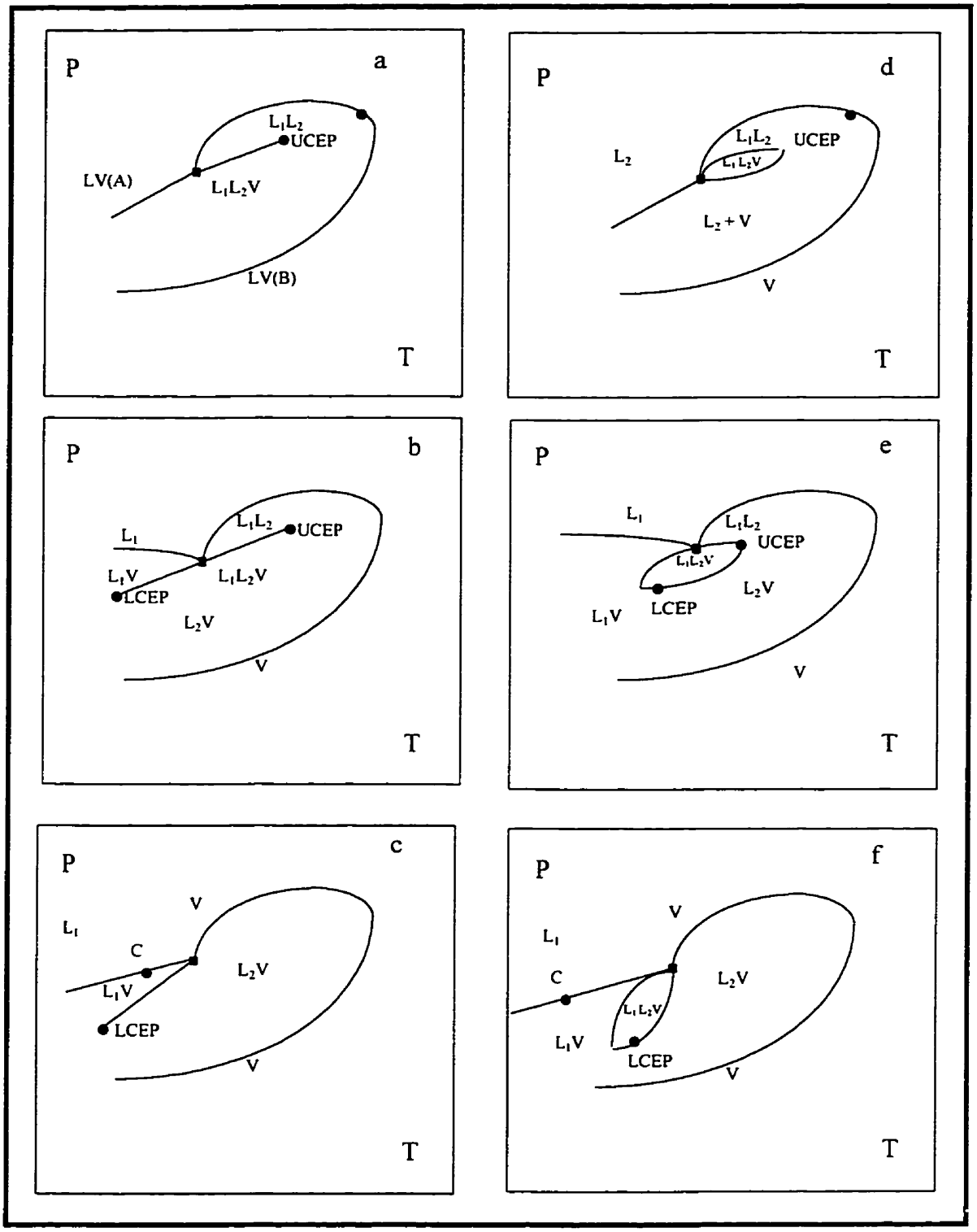

Figure 2.4.2 Expansion of P-T diagrams of Type V phase behaviour from binary mixtures to ternary mixtures [24].

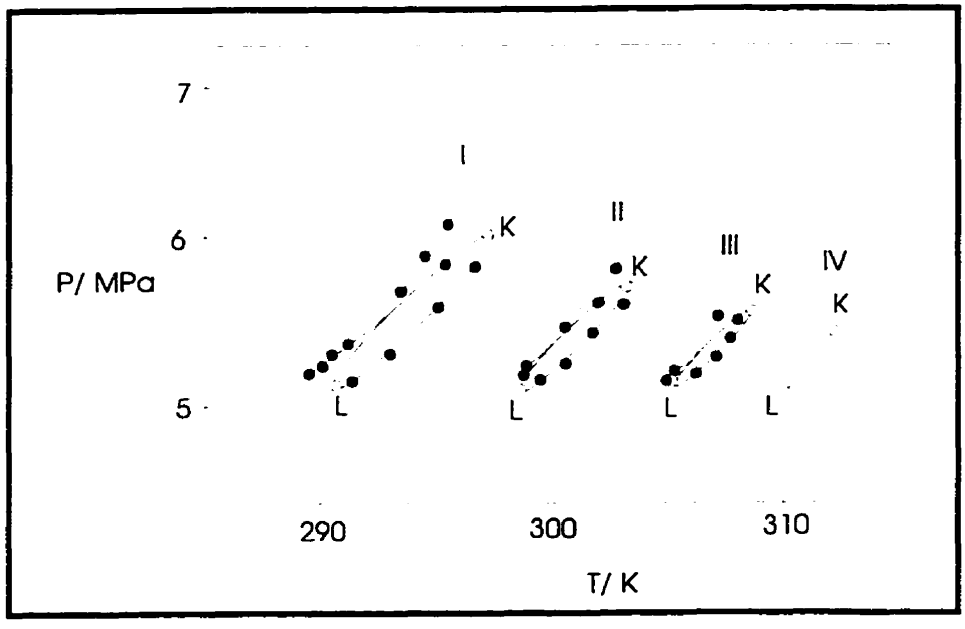

Figure 2.4.3 P-T diagrams of n-decylbenzne + ethane + carbon dioxide I) 40 mole % carbon dioxide, II) 20 mole % carbon dioxide, III) 10 mole carbon dioxide and IV) n-decylbenzene + ethane binary [9].

2.5 Retrograde Condensation

It was shown [26,27] that hydrocarbon condensates usually occur as a result of pressure reduction, even if the temperature remains constant. This phenomenon is known as retrograde condensation [28]. Kuenen,1906 [29] was the first who demonstrated the formation of a liquid in phase equilibrium experiments with decreasing pressures [30], i.e., observing the following sequence of phase transformations V→ L+V → V by reducing pressure. This phenomenon is shown in Figure 2.5.1, e.g. along the line segment FGH.

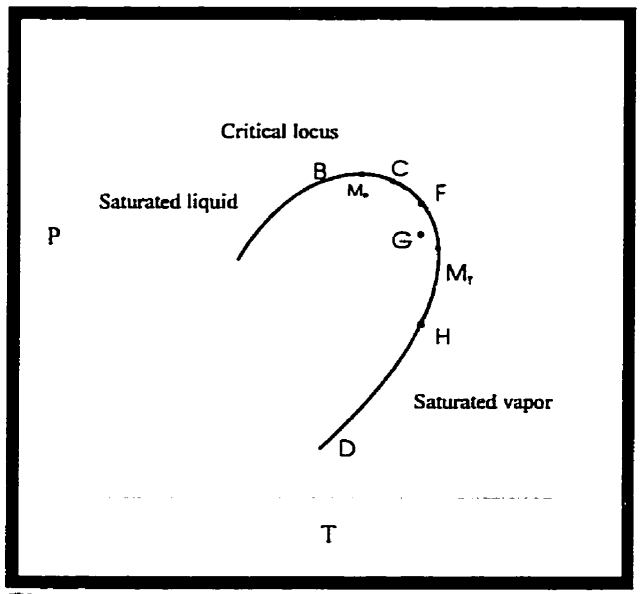

Figure 2.5.1 Portion of a P-T diagram in the critical region

2.5.1 Usual Retrograde Condensation

Consider the enlarged nose section of a single P-T loop shown in Figure 2.5.1 The critical point is at C. The points of maximum pressure and maximum temperature are identified as M_p and M_T. The dashed curves of Figure 2.5.1 indicate the fraction of overall system that is liquid in a two-phase mixture of liquid and vapour. To the left of the critical point C a reduction in pressure along a curve such as BD is accompanied by vaporization from the bubble point to

the dew point, as would be expected. However, if the original connection corresponds to point F, a state of saturated vapour, liquefaction occurs upon reduction of the pressure and reaches a maximum at G, after which vaporization takes place until the dew point is reached at H.

Retrograde condensation is of considerable importance in the operation of certain deep natural-gas wells where the pressure and temperature in the underground formation are approximately the conditions represented by point F. If one then maintains the pressure at the well head at a value near that of point G, considerable liquefaction of the product stream is accomplished along with partial separation of the heavier species of the mixture. Within the underground formation itself, the pressure tends to drop as the gas supply is depleted. If not prevented, this leads to the formation of a liquid phase and a consequent reduction in the production of the well.

In practice this phenomenon may take place in enhanced recovery processes. For example the exhibition of multiple liquid phases is known in mixtures of carbon dioxide and crude oil at temperatures not too far above the critical temperature of carbon dioxide, where this gas is used as a driving gas in low temperature reservoirs. The efficiency of a displacement of oil by carbon dioxide depends on a variety factors. It is particular importance, however, that the phase behaviour generated during the displacement should be known. Details of the phase behaviour of carbon dioxide and crude oil in low temperature reservoirs are given by Orr et al., 1981 [31] and Larsen et al., 1989 [32].

2.5.2 *Unusual Retrograde Condensation of Two Liquids*

The retrograde condensation of two liquids is a logical extension of the retrograde condensation of one liquid and generally occurs in fluids showing partial immiscibility in the liquid phase. Under certain conditions multicomponent hydrocarbon mixtures give quite complicated phase behaviour, as for example liquid-liquid-vapour (L_2L_1V) immiscibility. Moreover, it also has been observed that a second, heavier, liquid phase (L_2) can show retrograde condensation in the presence of a light liquid (L_1) and a vapour (V). From the phase rule, a mixture must have at least three components in order to exhibit unusual retrograde condensation of a second liquid phase. Extensive studies on this phenomenon by Shaw et al.,

[9] and Gregorowicz et al., [24,33] conclude that unusual retrograde condensation occurs with low fractions of the heavy component. Shaw et al., [9] also point out that unusual retrograde condensation is difficult to model. The modelled retrograde condensation is predicted at lower heavy component mole fractions than obtained experimentally; that is, the phase behaviour had to be modelled at an apparent composition.

The phenomenon of retrograde condensation of two liquid phases can easily be understood. In binary mixtures a three-phase equilibrium $L_1 + L_2 + V$ is represented by a line in the P, T-projection (Figure 2.5.2a). However in the multicomponent mixtures this three-phase line has to be replaced by a three phase region in the P, T-projection (Figure 2.5.2b). From Figure 2.5.2b it can be seen (vertical dashed line) that from higher to lower pressure the following sequence of phase behaviour occurs: $L_1 \rightarrow L_1 + V \rightarrow L_1 + L_2 + V \rightarrow L_1 + V \rightarrow V$, with L_2 denser than L_1 . Depending on the overall composition of the mixture other sequences of phase transformations are possible. However, all possibilities will have in common that two liquid phases will disappear with reducing the pressure.

Robinson [25] observed on pressure decrease the following sequence of phases: $V \rightarrow V+L_1 \rightarrow V + L_1 + L_2 \rightarrow V + L_1 \rightarrow V$. It is evident that this system also exhibits retrograde behaviour of the light liquid L_1. In the case of the Gregorowicz [33] experiment on ternary systems the following phase sequence was found: $L_1 \rightarrow L_1 + V \rightarrow L_1 + V + L_2 \rightarrow L_1 + V \rightarrow V$. The difference is due to the occurrence of a $L_1 = V$ critical point on the two phase boundary instead of a K-point. The latter is observed at lower ethane concentrations (point K and C in Figure 2.5.3a and 2.5.3b). Figure 2.5.3b illustrates the situation for Robinson's mixture, while Figure 2.5.3a shows the Gregorowicz [33] situation. A vapour-liquid critical temperature lower than the L-point temperature is a necessary condition for simultaneous light and heavy liquid retrograde behaviour.

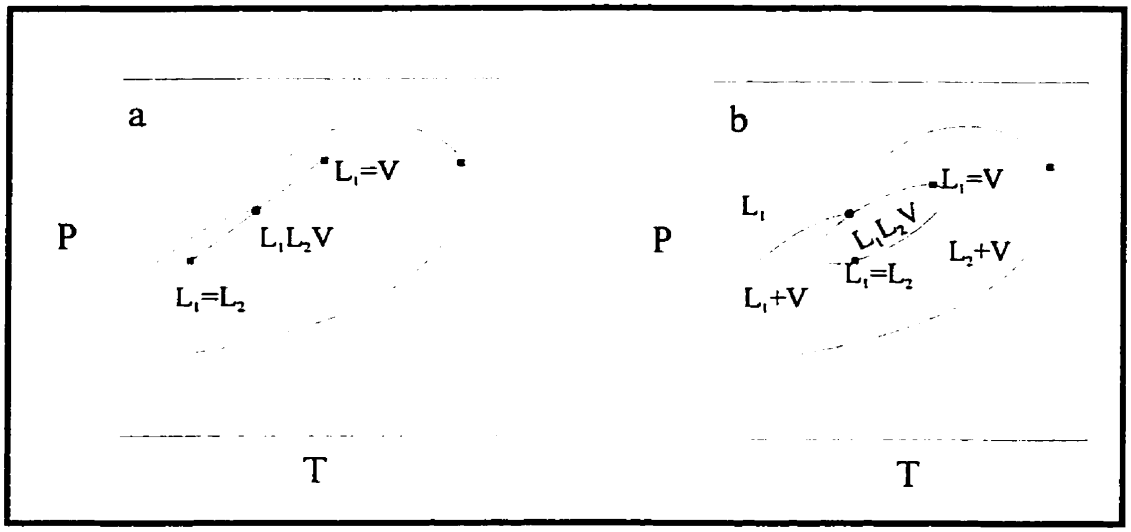

Figure 2.5.2 Expansion of P-T diagram from binary mixtures to ternary mixtures; a: binary mixtures, b: ternary mixtures.

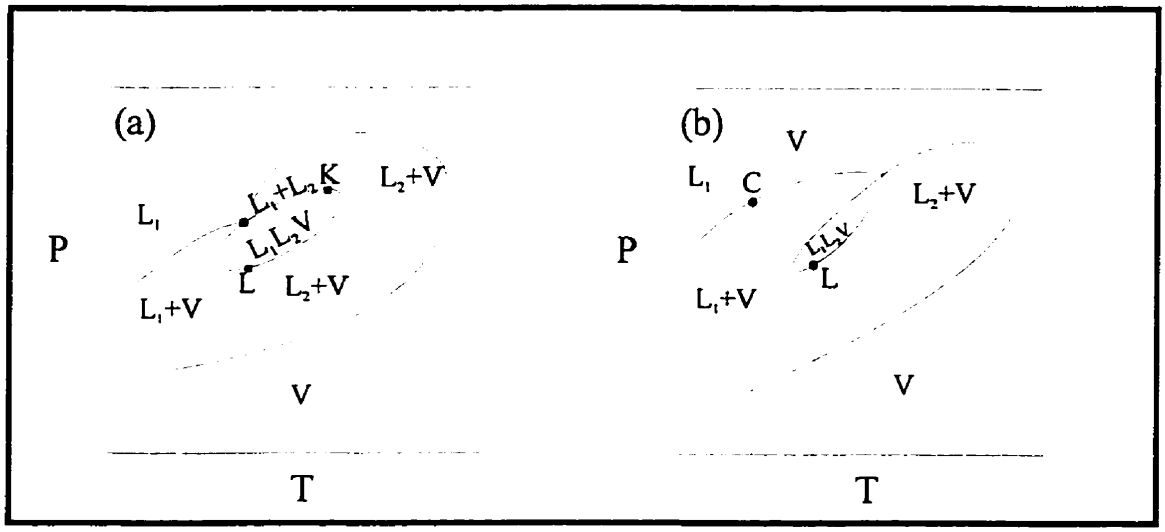

Figure 2.5.3 Three phase behaviour for the ternary system C_2+C_3+C_{20} : P, T-isopleth for different ethane concentrations; K: L_2+L_1=V; L: L_2=L_1+V; C: L_1=V, Gregorowicz et. al. [33].

2.6 Sensitivity of Equation of State to Input Parameter Values

The prediction of multiphase behaviour (L_1L_2V) for some three-component model reservoir fluids using the Peng-Robinson Equation of State (PR EOS) has been discussed by Shaw *et al.*, 1993 [9], and P.J. Smits, 1992 [34] among others. In cases studied where the third component is not miscible with the other two, the predicted LLV zones are shifted to lower pressures and temperatures than found experimentally, while the size, shape, and location of the zones were approximately correct as exemplified by Figure 2.6.1. The addition of a miscible third component yields small three phase regions which disappear as a tricritical point is approached.

Many studies concerning the ability of the PR EOS to model experimental phase behaviour have concentrated on fitting liquid-vapour (LV) or liquid1-liquid2 (L_1L_2) behaviour to obtain the following: optimum binary interaction parameters, correlations for binary interaction parameters, tri-critical point estimates, and critical point estimates. Cartlidge and Shaw 1994, [35] studied the effect of varying input parameters such as critical pressure, critical temperature , acentric factor (ω), binary interaction parameters (k_{ij}), and composition (x_i) on the predicted size, shape, and location of L_1L_2V zones.

They showed that the PR EOS was inflexible with respect to the general placement of boundaries for multiphase behaviour in the P,T plane for a model reservoir mixture of ethane + nitrogen + *n*-decylbenzene relative to the experimental boundaries. They showed that a ± 3.0 % variation in acentric factor of n-decylbenzene had a significant impact on the prediction of multiphase behaviour that was qualitatively similar to the impact of critical pressure variation, as shown in Figure 2.6.2. A decrease in this value resulted in an L_1L_2V region that was smaller and shifted to higher pressures but was relatively unchanged with respect to temperature. They also showed that a variation of ± 0.01 in the interaction parameter between ethane and *n*-decylbenzene did have a significant effect on the predicted L_1L_2V envelopes. As multiphase phase behaviour prediction is particularly sensitive to the value of the binary interaction parameter for the binary pair in which the multiphase behaviour originates, these values must be known with a precision generally greater than that currently obtained from less sensitive vapour liquid equilibrium data.

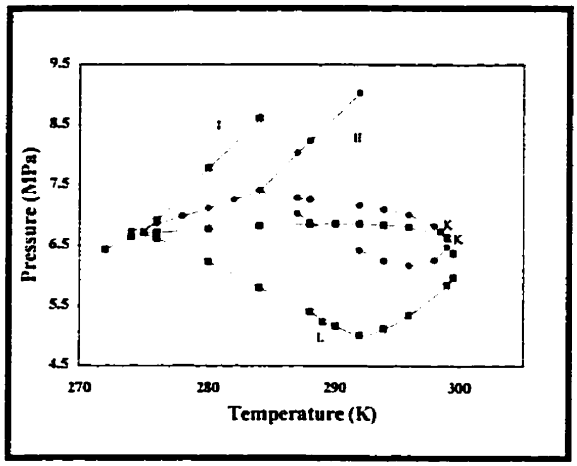

Figure 2.6.1 Predicted L_1L_2V phase boundaries (I, Peng - Robinson equation of state; II, experimental data [9]) for a model reservoir mixture: 94.09 mole% ethane + 3.00 mole % nitrogen + 2.91 mole% *n*-decylbenzene.

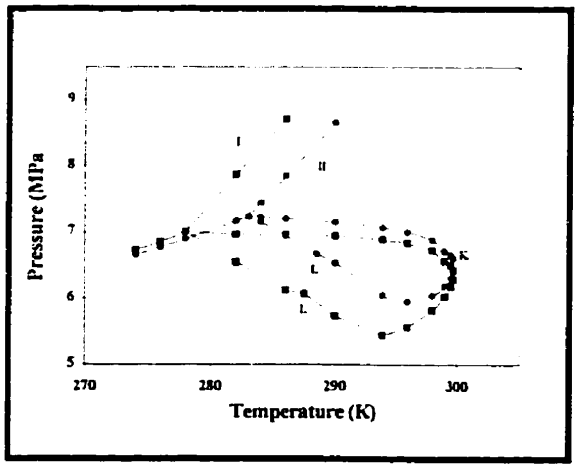

Figure 2.6.2 Predicted L_1L_2V phase boundaries using different values of acentric factor for *n*-decylbenzene (I, w = 0.68; II, w = 0.64), [35].

2.7 Nature and Characteristics of Asphaltene and Resin

The asphaltene is the most complex fraction of athabasca bitumen, as is the asphaltene fraction of any crude oil. The definition of asphaltenes is based upon the solution properties of petroleum residuum in various solvents. Asphaltene and resin were classified [36] as follows : (i) Neutral resins are defined as the insoluble fraction in alkalies and acids and are completely miscible with petroleum oils, including light fractions; (ii) Asphaltenes are defined as the insoluble fraction in light gasoline and petroleum ether. In contrast to resins, the asphaltenes are precipitated in the presence of an excess ether.

Asphaltene is defined by chemists as the part precipitated by addition of a low-boiling paraffin solvent such as n-pentane (although n-heptane has been recently proposed as a more appropriate precipitating agent) and benzene soluble fraction whether it is derived from carbonaceous sources such as petroleum, coal, or oil shale. There is a close relationship between asphaltenes, resins, and high molecular weight polycyclic hydrocarbons. In nature, asphaltenes are hypothesized to be formed as a result of oxidation of natural resins. On the other hand, the hydrogenation of asphaltic compound products containing neutral resins and asphaltene produces heavy hydrocarbon oils, i.e., natural resins and asphaltenes are hydrogenated into polycyclic aromatic or hydroaromatic hydrocarbons which differ, however, from polycyclic aromatic hydrocarbons by the presence of oxygen and sulfur in varied amounts.

On heating above 300-400^{o} C, asphaltenes do not melt, but decompose, forming carbon and volatile products. They react with sulfuric acid forming sulfonic acids, as might be expected on the basis of the polyaromatic structure of these components. The color of dissolved asphaltenes is deep red at very low concentration in benzene as 0.0003 % makes the solution distinctly yellowish. The color of crude oils and residues is due to the combined effect of neutral resins and asphaltenes. The black color of some crude oils and residues is related to the presence of asphaltenes which are not properly peptized.

Our knowledge of the asphaltenes is very limited. Asphaltenes are not crystallized and cannot be separated into individual components or narrow fractions. Thus, the ultimate analysis is not very significant, particularly taking into consideration that the neutral resins

are strongly adsorbed by asphaltenes and probably cannot be quantitatively separated from them. Not much is known of the chemical properties of asphaltenes.

A representative structure for asphaltene molecules was proposed by Altamirano, 1986 [37] and includes carbon, hydrogen, oxygen, nitrogen, sulfur as well as polar and non-polar groups as shown in Figure 2.7.1. Asphaltenes can assume various forms when mixed with other molecules depending on the relative sizes and polarities of the particles present. It has been shown that asphaltenes span a wide range of molecular weights as it is shown in Figure 2.7.1. A representative structure for resin and asphaltene molecules belonging to the Athabasca crude [37] includes carbon, hydrogen, oxygen, nitrogen, sulphur as well as polar and non-polar groups as shown in Figure 2.7.2. Their structure can vary from source to source as reported by Yen et. al., 1994 [38].

A great deal of experimental evidence suggests that asphaltenes consist of condensed polynuclear aromatic ring structures that bear alkyl side chains. The number of rings in a given system varies from six to fifteen, and perhaps up to twenty, as determined from

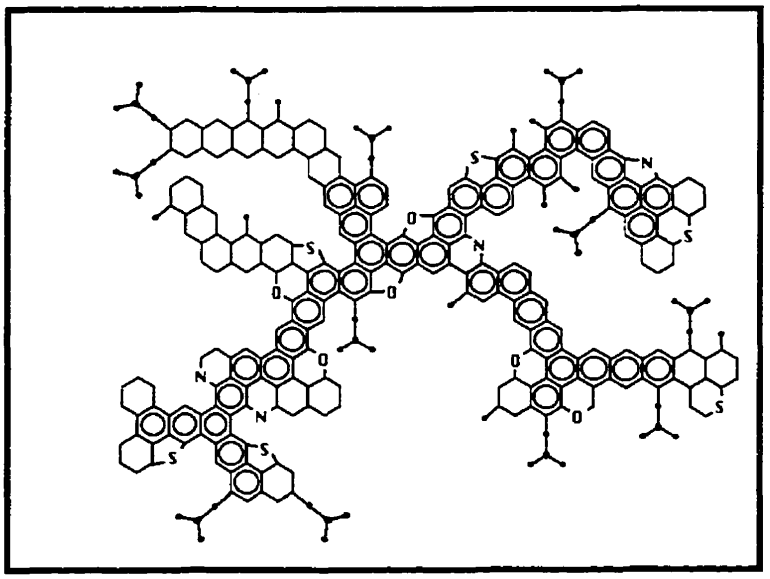

Figure 2.7.1 Molecular structure for asphaltene derived from Maya crude, proposed by Altamirano (1986) [37].

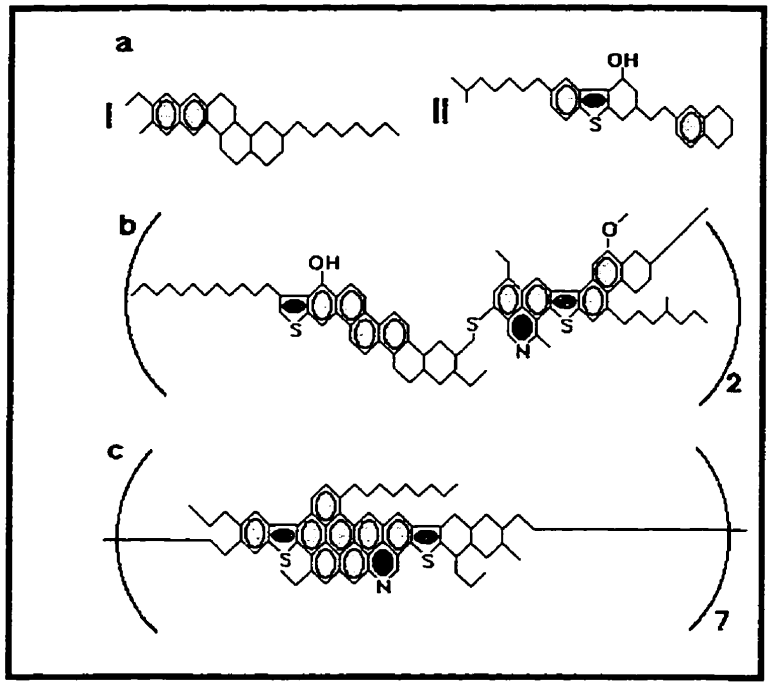

Figure 2.7.2 Average molecular structural models of the fractions of Athabasca tar-sand bitumen and petroleum bitumens; (a) resin fraction, (b) asphaltene fraction of tar-sand bitumen; (c) asphaltene fraction of petroleum bitumen proposed by Susuki et al., 1982 [39].

spectroscopic methods. However the average molecular weight of the asphaltene fraction is greater than 3000. In fact, it is almost 7000 for Cold Lake asphaltenes. The very high average molecular weight can be accounted for only if the condensed aromatic units are repeated several times in typical asphaltene molecules. Speight [40] reported that resins and oils may undergo polymerization reactions to produce asphaltene-type materials under mild reaction conditions within the McMurray formation. Ali [41] has verified the repetitions of condensed aromatic structures in an asphaltene molecule, in an attempt to develop a determination method for average molecular weight of aromatic compounds.

Asphaltene particles are therefore believed to exist in oil partly dissolved and partly in colloidal and/or micellar form. Whether the asphaltene particles are dissolved in crude oil, in steric colloidal state or in micellar form, depends, to a large extent, on the presence of other particles (paraffins, aromatics, resins, etc.) in the crude oil. The existence of various states of

asphaltenes in crude oil has been extensively discussed in numerous other publications[42-44]. Small asphaltene particles can be dissolved in a petroleum fluid, whereas relatively large asphaltene particles may flocculate out of the solution and then can form steric colloids in the presence of excess amounts of resins and paraffin hydrocarbons as demonstrated by the following Figure 2.7.3.

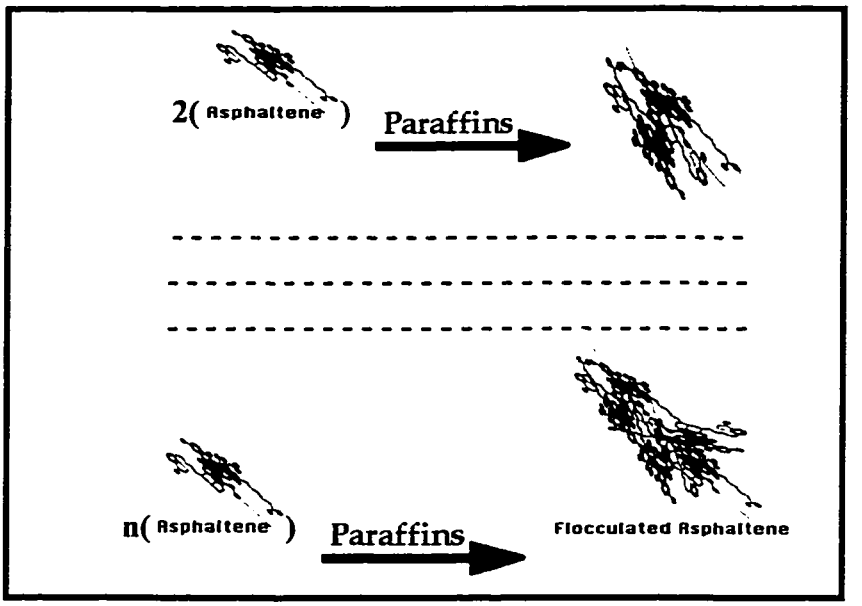

Figure 2.7.3 Various stages of asphaltene flocculation due to excess amounts of paraffins in the solution [36].

The flocculated asphaltene will precipitate out of the solution unless there is enough resin in the solution to cover the surface of asphaltene particles by adsorption forming steric-colloids as shown by Figure 2.7.4. The structures encountered in the four main constituent fractions (Saturates, Aromatics, Resins, and Asphaltenes) are very closely related. There is also a great deal of overlap of structures and properties between neighboring fractions. If we define the oil fraction to include the saturate and aromatic fractions, we observe, following the progression oils to resins, to asphaltene, an increase in aromaticity, average molecular weight, and sulfur and oxygen content. Variations in the relative amounts of the major fractions are

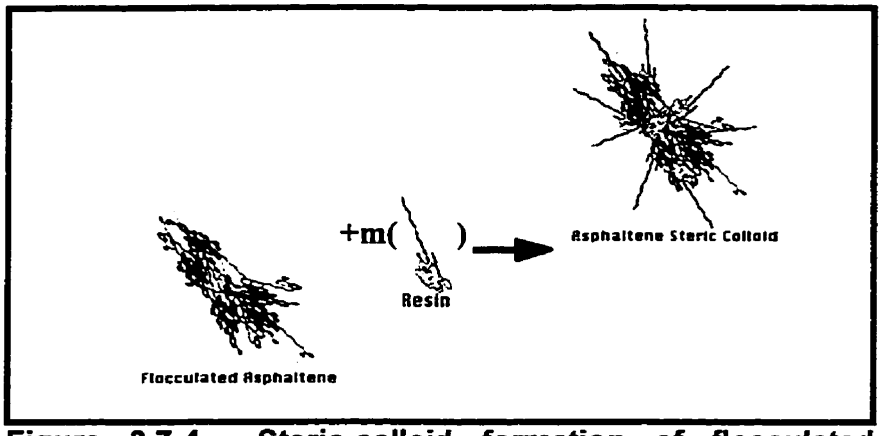

Figure 2.7.4 Steric-colloid formation of flocculated asphaltenes with resins [36].

accompanied by variations in the physical properties of bitumen. The API gravity falls with increased asphaltene content. Koots and Speight [45] observed that asphaltenes that had been separated from bitumen were not soluble in the oil fractions isolated from the same bitumen sample. The asphaltenes would dissolve in the oils only with the addition of the corresponding resin fraction. Attempts to dissolve asphaltenes in oils with the addition of resins from another type of crude eventually lead to dissolution. The resultant synthetic crude however was not stable and consequently experienced asphaltene precipitation on standing overnight.

Oils ➡ Resins ➡ Asphaltenes

- Increase in aromaticity
- Increase in average molecular weight
- Increase in sulfur and oxygen contents

2.8 X-ray Sorption: the Basis of Phase Behaviour and Phase Density Measurements

2.8.1 Absorptiometry with Polychromatic Beams

Absortiometry with polychromatic x-ray beams consists of an incident beam from an x-ray source which is passed through the sample (medium) to a detector (Figure 2.8.1). On passing through a medium, an x-ray beam loses energy mostly by photoelectric absorption and partly by scattering. The distance to which the beam penetrates the medium depends on the nature of the medium. Absorption increases very rapidly with increasing thickness and with increasing atomic number of the absorbing medium. This characteristic is used in absorptiometry.

Before examining the interaction of polychromatic beams with an absorber, let us review the simpler case of "monochromatic" beams (beams with one wavelength). For a monochromatic x-ray beam of wavelength λ, the loss of intensity follows the exponential law [46]

$$I(\lambda)=I_0\ e^{-\mu\rho\Delta x} \qquad (2.8.1)$$

where ρ and μ are, respectively, the density and mass absorption coefficient of the medium and I_0 is intensity of the incident beam (Figure 2.8.1). The mass absorption coefficient, μ, depends on the elemental composition and the energy (wavelength) of the x-ray beam. Mass absorption coefficient data of elements at available various wavelengths are tabulated [48]. For a chemical compound, a solution or a mixture, the mass absorption coefficient is simply the weighted average of the mass absorption coefficients of its constituent elements:

$$\mu = \sum_{i=1}^{n} \mu_i W_i \qquad (2.8.2)$$

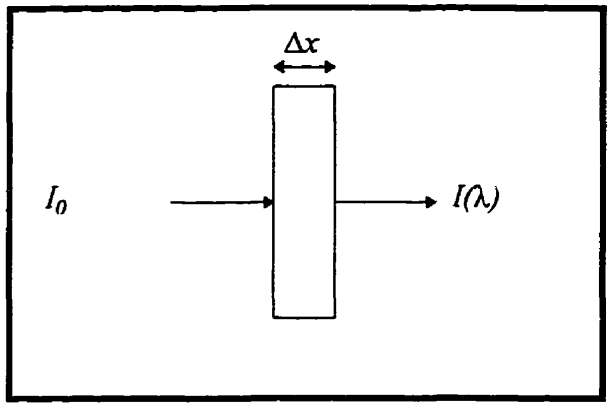

Figure 2.8.1 X-ray absorption phenomenon.

where μ_i and W_i are the mass absorption coefficient and weight fraction of element i, respectively. Thus, equation. 2.8.1 can be re-written as:

$$(1 / \rho \Delta x) \ln (I_0 / I(\lambda)) = \sum_{i=1}^{n} \mu_i W_i \qquad (2.8.3)$$

where the ratio $I_0 / I(\lambda)$ is referred to as transmittance.

With a polychromatic x-ray beam, equation 2.8.3 becomes very complicated (2.8.4) because an element like tungsten emits at numerous wavelengths [48]. In principal one could include the effect of these emissions because x-ray spectra are tabulated but in this work the

$$(1 / \rho \Delta x) \ln (I_0(\lambda_1) + I_0(\lambda_2) + \cdots + I_0(\lambda_i)) / (I(\lambda_1) + I(\lambda_2) + \cdots + I(\lambda_{ij})) =$$

$$+ W_a (\mu_a(\lambda_1) + \mu_a(\lambda_2) + \cdots + \mu_a(\lambda_i))$$

$$+ W_b (\mu_b(\lambda_1) + \mu_b(\lambda_2) + \cdots + \mu_b(\lambda_i))$$

$$+ \cdots\cdots$$

$$+ W_n (\mu_n(\lambda_1) + \mu_n(\lambda_2) + \cdots + \mu_n(\lambda_i)) \qquad (2.8.4)$$

overall mass absorption coefficient is not a strong function of composition (over the narrow range of compositions) at the single value of x-ray energy applied (carbon sorbs ~ 90% of the x-rays energy sorbed). Further an internal standard is employed with each experiment so one can make use of the effective wavelength concept as others have done [49] to obtain a correlation for density data.

2.8.2 *The Effective Wavelength*

The effective wavelength λ_e of a polychromatic x-ray beam is defined as the wavelength of a monochromatic beam which has an equivalent behaviour in an absorption measurement. It is useful in simplifying calculations as it allows one to use equation 2.8.1. The effective wavelength is a valuable guide to the behaviour of polychromatic beams. For example, the intensity of the transmitted beam from a sample can be predicted, with a good degree of accuracy, from effective wavelength.

Experimental measurement of effective wavelength can easily be performed by noticing that equation 2.8.1 can be rearranged as:

$$\ln I(\lambda_e) = \ln I_0 - \rho \mu \Delta x \qquad (2.8.5)$$

Therefore, the slope of a semi-log plot of transmitted intensity versus thickness at constant I_0 is equal to the negative product of mass absorption coefficient and density of the medium. With an x-ray exposure, the intensity variations are generated by passing the x-ray beam through a step-wedge made from a standard material such as aluminum. The differential attenuation caused by the step-wedge creates the required range of intensities. The variation in intensity is from the least amount of radiation which is transmitted through the top step of the staircase to the largest amount which is transmitted through the bottom step of the staircase.

It must be realized, however, that there is an alteration in the quality of the radiation as it is filtered by different steps of aluminum. If the steps have a constant increase in

thickness, the intensity changes in the beam do not also proceed in a constant relationship; the change in intensity per step is greater at the thin end of the wedge than at the thick end where the beam is more heavily filtered.

The use of such a step-wedge allows a single exposure from the x-ray beam to give to the detector a series of related exposures from the varied radiation intensities transmitted through the wedge. If the wedge has n steps it obviously gives n exposures. These related exposures from the steps can be plotted on the vertical axis of the graph versus the step thickness. This beam calibration method is effective as long as there are no absorption edges within the range of wavelengths, λ, of the polychromatic beam. This issue is addressed in detail in the Chapter which follows.

Chapter 3

EXPERIMENTAL

3.1 Design of Experiments

Experimental methods for the investigation of high-pressure phase equilibria can be divided into two classes, depending on how the composition is determined: analytical methods (or direct sampling methods) and synthetic methods (or indirect methods). Analytical methods involve the determination of the compositions of the coexisting phases. This can be done by taking samples from each phase and analyzing them outside the equilibrium cell at normal pressure.

Synthetic methods can be used where analytical methods fail, i.e., when a phase separation is difficult due to similar densities of the coexisting phases, e.g., near or even at critical points and in barotropic systems where at certain conditions the coexisting phases have the same density. With synthetic methods a mixture of known composition is prepared and the phase behaviour is observed in an equilibrium cell. No sampling is necessary. After known amounts of the components have been placed into an equilibrium cell, values of temperature and pressure are adjusted so that the mixture becomes homogeneous. Then the temperature or pressure is varied until the formation of a new phase is observed. Such experiments yield points on phase boundaries.

Since one of the objectives of this thesis is to observe the phase behaviour of ABVB/heavy oil + diluent + hydrogen mixture, accurate pressure, temperature, and composition measurements must be made in order for the data to be of use for modelling. Therefore the equipment was designed to eliminate as much error as possible in each of the three measurements mentioned above.

The general experimental set-up is shown schematically in Figure 3.1.1. The basic components are the same as those used by Dukhedin-Lalla, 1996 [47]. Two different types of cells were used for this series of measurements. The suffix A refers to the first set-up and B refers to the second. Our experience with the previous experimental set-up revealed that for a reliable density measurement, the image quality had to be improved. Further, an improved image quality enables us to distinguish phases with very small density differences (less than 0.02 g/cm^3). This goal was achieved and the next step was to calibrate the updated system. Calibration of the improved x-ray system is discussed in Sections 3.2 and 3.3.. Modification of imaging system is discussed in Section 3.4. Details of the general layout, individual components, experimental setup, operation and challenges are also provided in this Chapter.

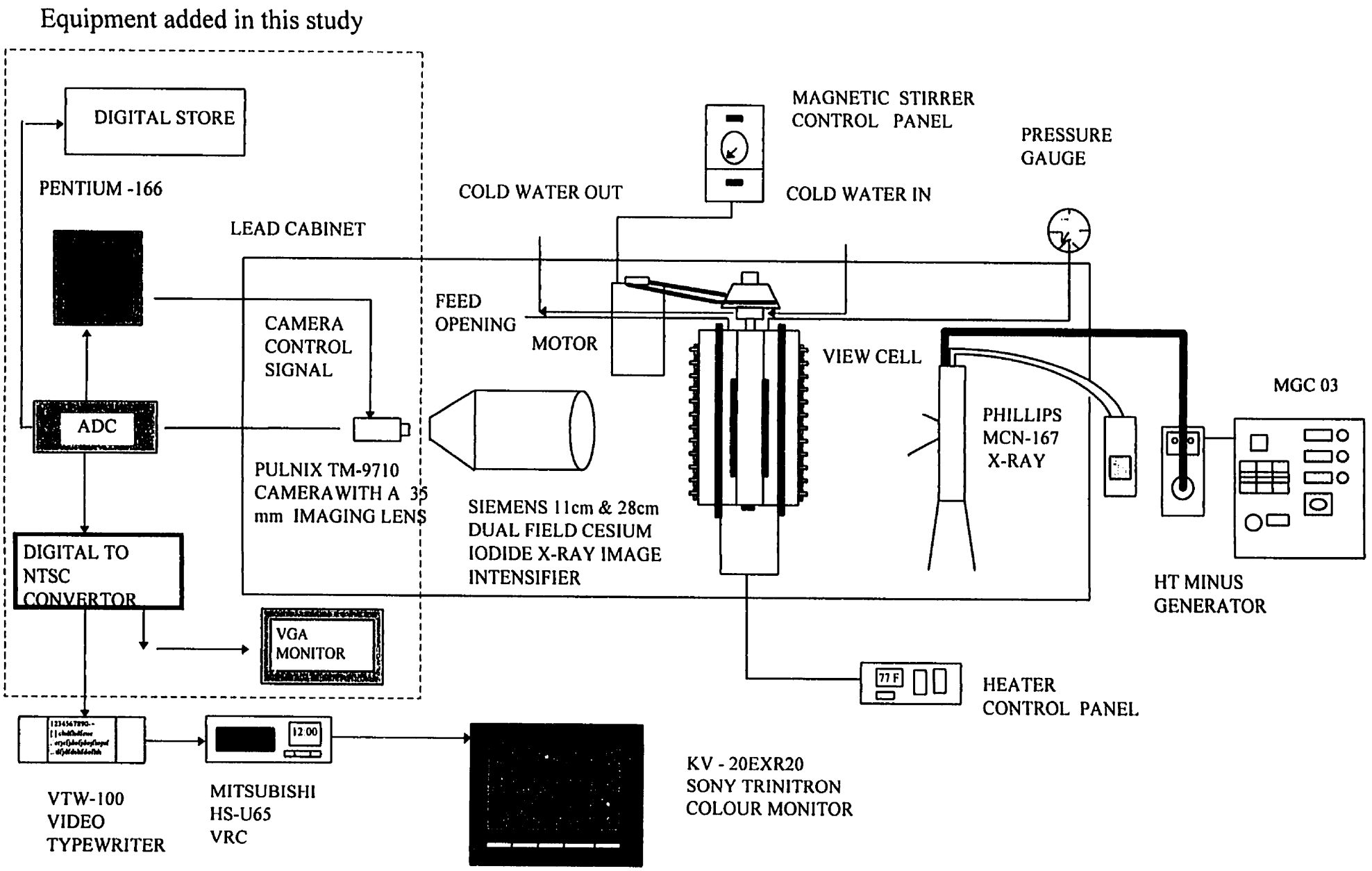

Figure 3.1.1 Experimental set-up

3.2 X-ray Calibrations

As mention in Section 2.8, the first step in the calibration of the x-ray tube is determining the effective wavelength of the x-rays. Experimental measurement of effective wavelength can be performed using equation 2.8.5 in conjunction with an aluminum step-wedge (Figure 3.2.1). This wedge possesses 15 steps, from 0.4 mm to 6.0 mm thick in 0.4 increments and was supplied by General Electric Medical System, serial number E6322HG. In a typical experiment the step wedge was placed between the source and the image intensifier and for each voltage five sets of reading were obtained. A total of 10 experiments were performed at two operating conditions. Data associated with these experiments are shown in Table 3.2.1. In the experiments of Figure 3.2.2, voltage was 45 kv. The data obtained permitted the estimation of mass absorption coefficients with fair accuracy for aluminum at two different voltages. Since the density of aluminum is given ($\rho_{Al} = 2.7\ g/cm^3$), the absorption coefficient for aluminum can be calculated at a specific voltage. The calculated data together with Table 3.2.2 make it possible to determine the effective wavelength for aluminum. In our experiments, the effective wavelength was found to be 0.38 A (slope= -2.379) at 45 kv.

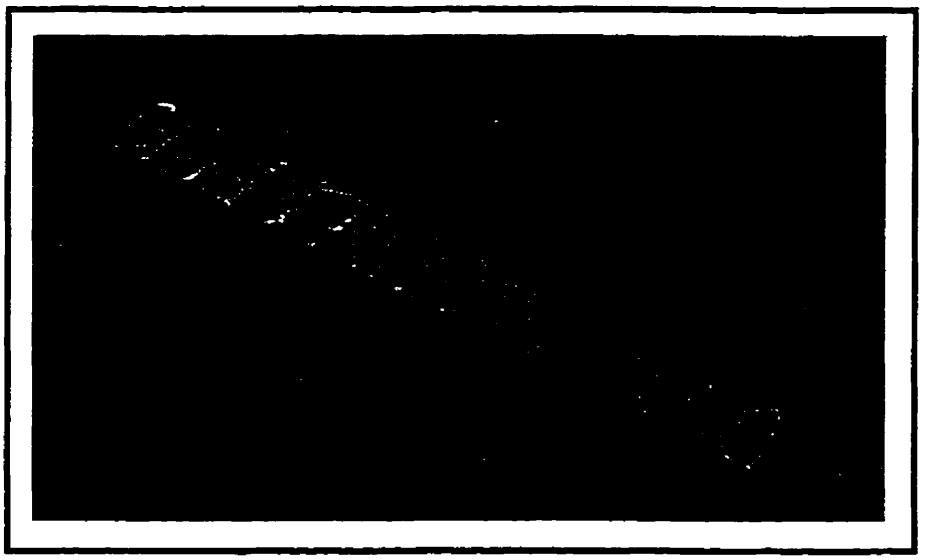

Figure 3.2.1 An aluminum step-wedge. 15 steps, from 0.4 mm to 6.0 mm thick in 0.4 mm increments

Table 3.2.1 X-ray intensity vs. aluminum thickness (45 kv, 30 mA).

Thickness (Cm.)	Intensity (Exp.)	Intensity (Exp.)	Intensity (Exp.)	Intensity (Exp.)	Intensity (Exp.)	Intensity (Exp.)
	Run # 1	Run # 2	Run # 3	Run # 4	Run # 5	Ave.
0.04	152.52	152.17	145.97	151.62	148.99	150.25
0.08	130.35	134.06	127.84	133.14	130.18	131.11
0.12	114.22	117.36	112.24	116.90	114.47	115.4
0.16	100.72	102.92	98.96	102.42	100.73	101.15
0.20	89.06	91.38	87.60	90.33	88.29	89.33
0.24	79.46	82.00	77.72	81.00	80.07	80.05
0.28	70.28	73.69	69.48	72.99	70.69	71.42
0.32	63.22	64.91	61.42	64.74	63.06	63.47
0.36	55.05	57.26	54.13	57.65	55.52	55.92
0.40	48.79	50.30	47.97	50.13	49.12	49.26
0.44	41.92	44.67	42.03	43.70	42.31	42.93
0.48	37.39	42.41	39.46	38.5	37.42	39.04

Table 3.2.2 Mass absorption coefficient for aluminum [48]

Effective Wavelength	0.2 A	0.25 A	0.3A	0.4A
Mass absorption coefficient cm^2 / g	0.277	0.38	0.525	0.97

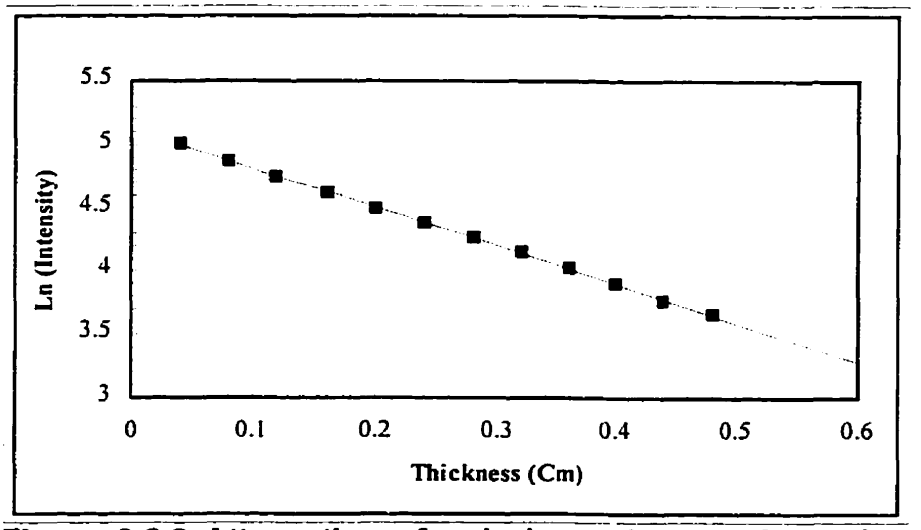

Figure 3.2.2 Attenuation of polychromatic x-ray beam by aluminum, 30 mA, 45 kv, standard deviation = 0.02

3.3 Phase Density Measurement

The analysis of hydrocarbon density under high temperature and pressure conditions has always been a difficult task. The purpose of the analysis was to devise a method by which density of heavy oil systems could be measured accurately. X-ray imaging as an analytical tool was found to be an adequate method in these types of systems. Since the heavy oil systems are opaque, typical experimental devices used in phase equilibria study are not adequate because they rely on simple visual observation. It was concluded that an x-ray device would make an effective experimental apparatus for determining density based on the fact that the amount of x-ray transmissions through an object is a function of the object's atomic density. Equation (2.1) illustrates how x-ray image intensity is a function of the density of an object. An important aspect of equation (2.1) is that there is one other variable (mass absorption coefficient, μ) in the equation aside from the intensity and density which are a function of atomic structure. In general the x-ray absorption coefficient of a material can be expressed as a sum of the contributions from the composing elements

$$\mu_\lambda = \sum_{i=1}^{n} \mu_{\lambda} W_i \qquad (3.3.1)$$

Once the equivalent wavelength (λ_e) is found one may calculate the mass absorption coefficient (μ) for chemical compounds using equation (3.3.1). Accordingly, one would like to know the absorption coefficient of all pure elements as a function of energy (kev). For x-ray spectrometry, the relevant energy is from 0.1 up to 100 kev. In the literature absorption coefficients can be found as a function of energy (Table 3.3.1). Energy can be calculated by

$$E\ (\text{kev}) = 1.24 / \lambda\ (\text{nm}) \qquad (3.3.2)$$

where E is the energy of incident beam and λ is the wavelength. In our experiments energy (E) was found to be 33 kev.

The next step is to calculate, by linear interpolation between (E, μ) pairs of absorption coefficients for each element at about the same energy value. Then using the mass absorption coefficient for each pure element, the mass absorption coefficient for any chemical compound can be calculated. The values of mass absorption coefficients for a variety of pure organic compounds are tabulated in Table 3.3.2. Data show that the mass absorption coefficient for organic compounds is constant as we expected (The hydrocarbons that were investigated were all similar in structures and components). Thus, the density of mixture can be estimated by measuring the ratio of transmitted to incident x-ray image intensity. Figure 3.3.1 is a semi-log plot of intensity versus density (calibration curve); the plot is satisfactorily linear (Appendix 1).

Table 3.3.1 Mass absorption coefficient for the elements at E=33 kev [48]

Atomic number, Z	1	6	7	8
μ (cm^2/g)	0.353	0.224	0.289	0.338

Table 3.3.2 Mass absorption coefficient using $\mu_\lambda = \sum_{i=1}^{n} \mu_\lambda^i W_i$, s=0.0041, s^2=1.7E-05

		w_H	w_C	w_O	w_N	μ_λ
1-phenyldecane	C6H5(CH2)9CH3	0.12	0.88			0.236
benzyl alcohol	C6H5CH2OH	0.07	0.78	0.15		0.243
ethylbenzyl	C6H5C2H5	0.1	0.9			0.233
dodecane	C12H26	0.15	0.85			0.240
toluene	C6H5CH3	0.09	0.91			0.232
heptane	C7H16	0.16	0.84			0.241
hexadecane	C16H34	0.15	0.85			0.240
o-xylene	C6H4(CH3)2	0.1	0.9			0.233
decane	C10H22	0.15	0.85			0.240
indene	C9H8	0.07	0.93			0.229
pyridine	C5H5N	0.06	0.76		0.18	0.235
butylbenzene	C6H5(CH2)3CH3	0.1	0.9			0.233
decahydronaphthalene	C10H18	0.13	0.87			0.237
cyclohexane	C6H12	0.14	0.86			0.239

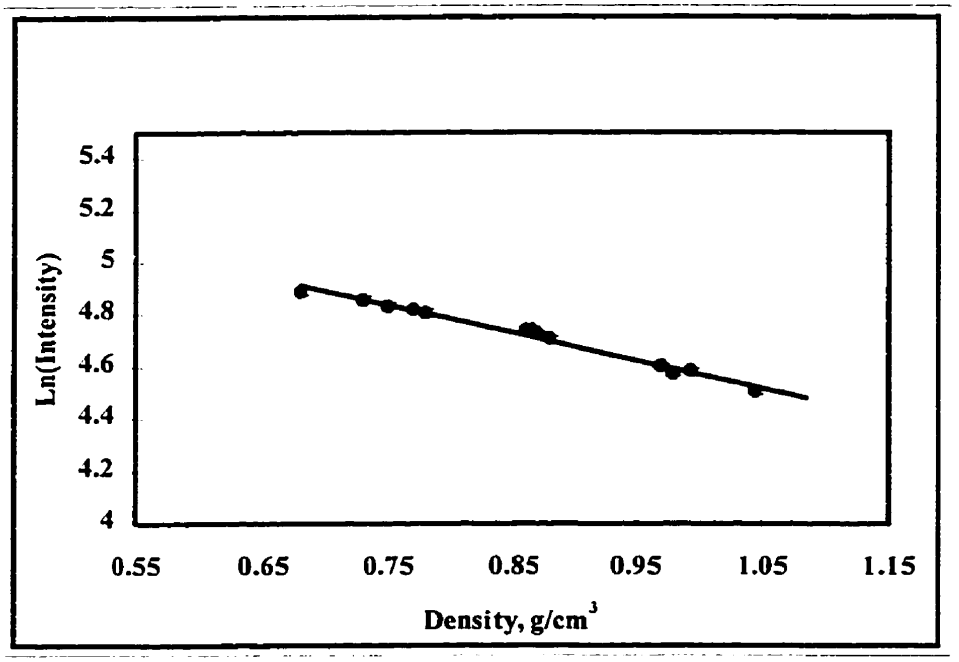

Figure 3.3.1 Liquid density measurements, calibration curve.

3.4 X-ray Imaging System

The x-ray imaging technique improved as part of this Ph.D. thesis program has been used to make direct observations of complex phase behaviour of opaque organic fluids at elevated temperatures and pressures. The x-ray imaging system has also proven to be an excellent method for determining densities of heavy oils at high temperatures and pressures, Figure 3.3.1. Small density differences between liquid hydrocarbon phases, in the order of magnitude of 0.02 g/cm^3, can be distinguished by this technique. For the experiments that we have done so far the density data are readily regressed. However the photoelectric absorption is made up of absorption in the various atomic levels and is an atomic number dependent function. A plot of μ against λ contains a number of discontinuities, called absorption edges, at wavelengths corresponding to the binding energies of the electrons in the various subshells. The absorption discontinuities are a main source of nonlinearity between x-ray intensity and composition in x-ray fluorescence; and concern was expressed about the generality of the density correlation. Polychromatic x-ray beams generated in the range 25 to

75 kv involve effective wavelengths in the range of about 0.23 to 0.64 A. Only those elements between atomic number 42[1] and 65[2] have absorption edges in this range of energies [49]. The absorption of polychromatic x-ray for hydrocarbons is an ideal application because the hydrocarbon matrices have very low absorption coefficients and because these coefficients do not change appreciably with changes in the hydrocarbon makeup of the matrix as absorption by hydrogen and by carbon is nearly at the same wavelengths [49].

3.5 Imaging System Modification

Conventional phase equilibrium apparatus, e.g. Cailletet cells and related equipment, cannot be used with opaque fluids as this relies on direct visual observation for determining the number of phases present. Phase equilibrium apparatus based on sampling has proven unreliable for fluids which exhibit more than two phases. Recently, Dukhedin-Lalla and Shaw J.M., (1993) have assembled a view cell apparatus based on x-ray radiography. A detailed description of the x-ray view cell facility is given elsewhere [47]. Briefly, this facility consists of a beryllium view cell (equipped with a magnetically driven stirrer, thermocouples and ribbon heaters), an x-ray source (a Phillips MG-161 x-ray generating system, Figure 3.5.1), and a KP113 Hitachi CCD camera mounted to the back end of the image intensifier (a Siemens 11 cm x 28 cm dual field cesium iodide x-ray image intensifier, Figure 3.5.2).

During a typical experiment, black and white images from the CCD camera are sent to a video recorder (a Mitsubishi Twin Digital/Swift Servo VHS video recorder). Our experience with this experimental set-up revealed that for a reliable density measurement, the image quality required improvement. Further, an improved image quality enabled us to distinguish phases with very small density differences (0.02 g/cm^3). Figure 3.5.3 is a representation of the types of images obtained from the x-ray imaging system. This goal was achieved through the following steps:

---

[1] Molybdenum
[2] Terbium

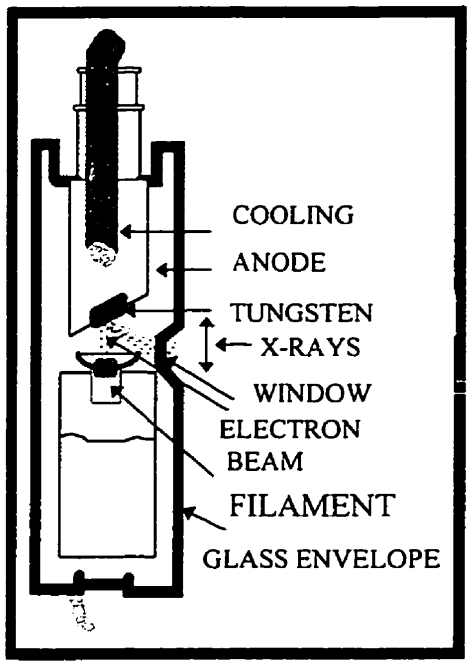

Figure 3.5.1 X-ray tube

- **Determining the image quality bottleneck:** Image resolution after image intensifier and CCD camera was measured (see Table 3.5.1) using two Resolution Phantoms (from Nuclear Associates).

Table 3.5.1 clearly revealed that the old CCD camera degraded image quality and significant improvement could be obtained by replacing it.

Table 3.5.1 Image resolution of the original x-ray view cell apparatus.

	Image Resolution (Lines/mm)	
	Horizontal	Vertical
After Image Intensifier	4.0	3.1
After Hitachi Camera (old)	1.0	0.9
After Pulnix Camera (new)	1.8	1.6

- **Replacing an equipment bottleneck:** After examining available cameras in the market, a Pulnix camera (TM-9701 progressive scanning full frame shutter) was selected. This camera has a resolution of 768(H)X484(V) (the KP113 CCD camera had a resolution of 430(H)X350(V)). As depicted in Figure 3.1.1, the improved x-ray view cell facility replaces the original CCD camera with the equipment enclosed by the dashed line. The shutter speed of the Pulnix camera is controlled via a P-120 computer. A frame grabber (Coreco, Oculus-F/64) enables us to record images digitally for further image analysis and intensity measurement.

- **Calibrating the improved view cell apparatus for density measurement:** This issue is discussed in detail in sections 3.2 and 3.3.

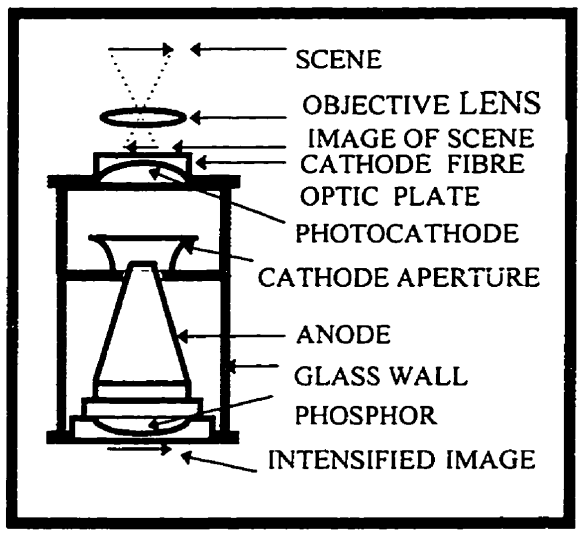

Figure 3.5.2 Image intensifier

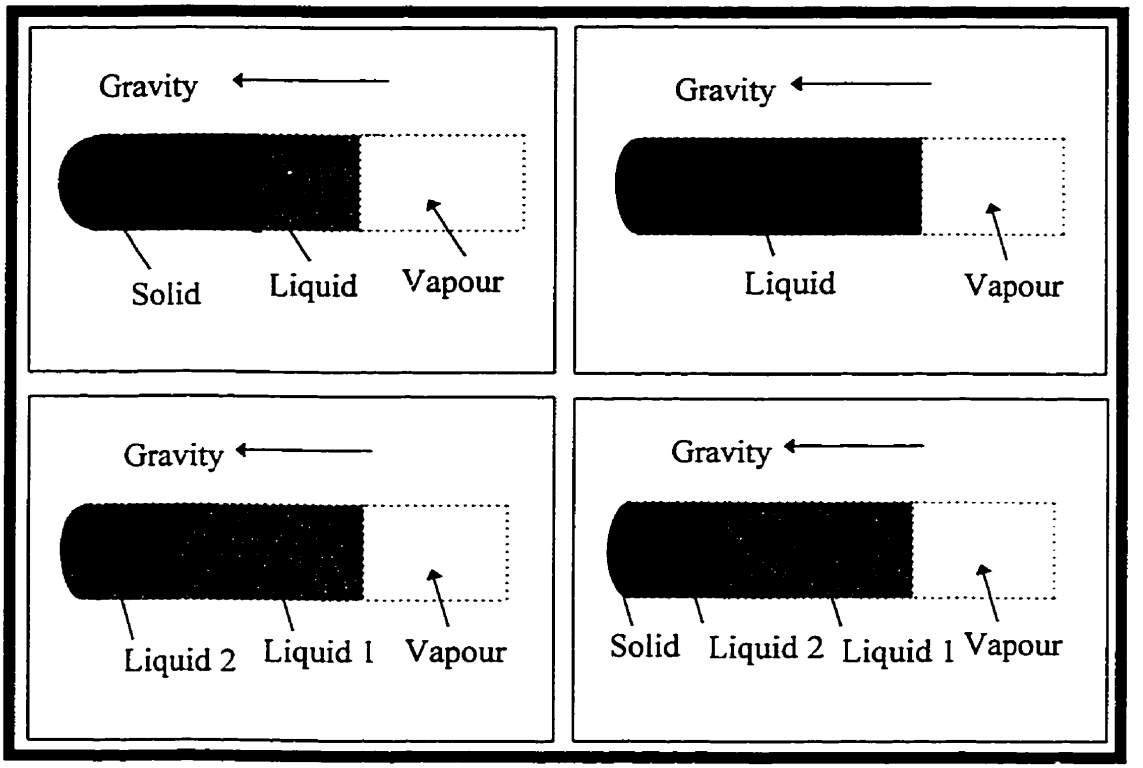

Figure 3.5.3 Schematic of various types of phase behaviour as observed with the imaging system

3.6 Beryllium Cell A

The beryllium cell A is a flat-sided "sandwich" style pressure vessel with a total volume of 1.5 L. The interior dimensions of the reactor are height - 30 cm, width - 10 cm and depth - 5 cm. The cell is equipped with 0.635 cm thick beryllium plates that allow x-rays to pass through (i.e., the mass absorption coefficient of beryllium is very low). The plates are attached to the front and the back sides of the reactor and provide a window that is 30 cm high and 2.5 cm wide. The vessel has a maximum allowable working pressure and temperature of 6.9 MPa and 725 K respectively. The beryllium cell is equipped with an Autoclave Engineering Magna Drive II magnetic stirrer. The stirrer is fitted with two sets of propellers. This double propeller design provides excellent mixing. One set of propellers is located about 2.54 cm from the bottom of the cell and the second set is approximately 12.5 cm from the bottom of the reactor. Two ribbon heaters provide approximately 4.5 kW of power to the cell and its contents.

3.7 Loading the Cell

During a typical experiment, the prepared sample of the athabasca bitumen vacuum bottoms is heated past its melting point. A certain volume (which is estimated from knowing roughly the loading necessary for three-phase coexistence) is withdrawn by use of a beaker. The beaker with the sample is then cooled and weighed on a balance. The beaker is warmed to melt the sample which was then poured into the cell through the top port. The beaker is weighed after cooling and the number of moles of hydrocarbon added to the cell is calculated from the weight difference. The cell is loaded with solvent and is then degassed via the vacuum line. The cell is purged and then pressure-tested with hydrogen to the desired pressure. If leaks are detected, or if the pressure does not hold, the source of the leak must then be found and corrected. This may involve disassembling of the cell to replace sample lines, fittings or gaskets.

At this point the system is ready to commence heating and the heater is switched on. Once the temperature in the view cell reaches about 373 K the magnetic stirrer is switched

on. The agitator is then turned off and the number of phases counted. The temperature is then raised again and so on. Typically, the stirrer is switched off every fifteen minutes during the course of the experiment and the system allowed to equilibrate for approximately five minutes (depending on the experiment).

Results from several experiments are combined to produce complete pressure vs. temperature phase diagrams for individual compositions. The view cell is limited to pressures less than 6.9 MPa and temperatures less than 725 K. Such a limitation is not serious as it was shown that athabasca bitumen vacuum bottoms and hydrogen exhibit liquid-liquid-vapour behaviour within these bounds [50].

3.8 Safety/Environmental Concerns

3.8.1 X-ray

The entire set-up of x-ray gun, view cell, image intensifier and video camera is housed in a lead lined box which is equipped with a series of fail-safe switches. This safety set-up ensures that the x-ray gun is immediately deactivated once any of the doors of the lead-lined housing is opened.

3.8.2 Liquid Trap

Since an aspirator was present in the system, a liquid trap was necessary.

3.8.3 Fumehood

During an accident, the fumehood would have removed any airborne mixtures of hydrogen and organic compounds.

3.8.4 Hydrogen Gas and Rupture Disc

The use of hydrogen gas requires care. When moving cylinders, ensure that the valve caps are in place and secure the cylinder when in location. Vent hydrogen slowly as static electricity, generated by the hydrogen flow, can ignite the gas. Purge the view cell thoroughly

with nitrogen before introducing the hydrogen. The cell should not be heated above 700 K as the structure of the stainless steel could be compromised, lowering its yield strength. The initial hydrogen pressure in the cell should not exceed 3.9 MPa in order to avoid approaching the rupture disc pressure. The pressure rises substantially during the experiment.

3.9 Computer Assisted Measurements

3.9.1 Recording Images

Video images detailing the position of the interfaces were recorded on video tape. Once captured on video tape, an image could be copied from the VCR and saved as a digital image file by the frame grabber software.

3.9.2 Image Analysis Software

A captured image consisted of various shades of gray ranging from white to black. The bands of shade were then adjusted by the user for each overlay. An overlay was a shaded area that was captured by the user by adjusting the range of intensity. By adjusting the bands differently to capture each phase the user selected and counted the pixels of both the gas and liquid phases. This information was used to calculate the volumes of gas and liquid phases in the view cell.

3.10 Cleaning Procedure

Research grade tetrahydrofuran (THF) is the solvent used for the less volatile hydrocarbons. Both cell A and cell B are cleaned by alternately injecting and siphoning THF through the sampling port. The lines are cleaned by applying a vacuum and drawing THF through them. Pentane is injected through the bleed screw in the bottom of the pressure transducer to rinse the diaphragm. After each cleaning, the cell was evacuated for at least a couple of hours, preferably overnight, to get rid of remaining solvent. The lines were also cleaned occasionally by passing ethane through them under pressure. The glass syringe used for injecting the less volatile components into the cell was also cleaned with THF. The

cleanliness of the syringe was verified by checking the reproducibility of its weight to within 0.5 mg when clean and dry.

3.11 Materials

Athabasca Bitumen Vacuum Bottom samples were supplied by CANMET (Table 3.11.1). Hydrocarbons listed in Table 3.11.2 were obtained from Sigma and Fluka and were of research grade purity. Gases listed in Table 3.11.2 were obtained from CANOX and were also of research grade purity. The physical properties of the gases and solvents, obtained from various suppliers, are given in Table 3.11.3.

Table 3.11.1 Physical properties of ABVB

Specific gravity	1.046 (24 ° C)
Carbon	84.3
Hydrogen	10.9
Nitrogen	0.80
Oxygen	0.3
Sulfur	3.5
Pentane insoluble (wt %)	38.4
H/C	1.54
Aromatic carbon	35.4
524 + Resid	99.3

Table 3.11.2 Chemicals used, their formula, molecular weight, and purity

	Formula	Molecular Weight
cyclohexane	C_6H_{12}	84.162
heptane	C_7H_{16}	100.205
benzyl alcohol	$C_6H_5CH_2OH$	108.15
hexadecane	$C_{16}H_{34}$	226.448
dodecane	$C_{12}H_{26}$	170.34
anthracene	$C_{14}H_{10}$	178.24
decane	$C_{10}H_{22}$	142.29
o-xylene	C_8H_{10}	106.17
toluene	$C_6H_5CH_3$	92.14
pyridine	C_5H_5N	79.1
indene	C_9H_8	116.16
butyl Benzene	$C_6H_5(CH_2)_3CH3$	134.22
decahydronaphthalene	$C_{10}H_{18}$	138.26
tetralin	$C_{10}H_{12}$	132.21
ethyl Benzene	$C_6H_5C_2H_5$	106.17
hydrogen	H_2	2.016
nitrogen	N_2	28.013

Table 3.11.3 Physical properties of miscellaneous chemicals.

	ρ (g/cm^3)	T_b (K)	T_m (K)	T_c (K)	P_c (MPa)
cyclohexane	0.779	353.8	279.6	553.6	4.07
heptane	0.684	371.6	182.6	540.3	2.74
benzyl alcohol	1.049	478.3	257.7	641.65	4.18
hexadecane	0.733	560.0	291.0	722.0	1.41
dodecane	0.749	489.5	263.4	658.2	1.82
anthracene	1.2	613	485	869.3	2.9
decane	0.73	446	243.55	617.55	2.11
o-xylene	0.88	417	248	630.3	3.73
toluene	0.866	383	178	593.95	4.22
pyridine	0.983	389	231	619.95	
indene	0.999	457	271.35		
butyl Benzene	0.86	455	185	658.68	2.81
decahydronaphthalene	0.87	465	230	691	2.91
tetralin	0.967	478	243		
ethyl Benzene	0.867	409	178	517.05	3.74
hydrogen		20.3	14.0	33.2	1.297
nitrogen		77.4	63.3	126.2	3.39

3.11.1 Heavy Oil Characterization

Limited data are available for athabasca bitumen vacuum bottoms. Bitumen is a natural asphaltic residue made up of many different and unknown compounds, and athabasca bitumen is simply this natural material as obtained from the Athabasca oil sands located in northern Alberta. Using conventional vacuum distillation, materials which boil at temperatures as high as 797 K can be separated [3]. The remaining materials are the vacuum bottoms. Beyond 797 K, the bitumen degrades; thus, the fractions of ABVB cannot be obtained by conventional vacuum distillation. Therefore, a boiling curve for this mixture does not exist. Recently, narrow fractions of ABVB have been prepared by Syncrude Canada Ltd. using supercritical fluid extraction. Supercritical fluid extraction (SCFE) is capable of separating narrow fractions of ABVB because, unlike vacuum distillation, SCFE operates at temperatures much lower than the cracking temperature of ABVB. This new technology allows for much more insight into the chemistry and properties of ABVB. The molecular weights of the ABVB narrow fractions have been determined by Syncrude and the ABVB molecular weight distribution is presented in Figure 3.11.1.

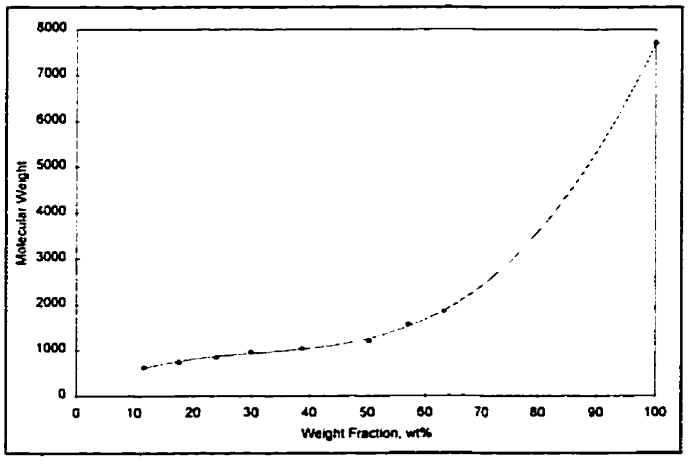

Figure 3.11.1 Molecular weight distribution of ABVB [3].

As shown in Figure 3.11.1, in the first nine fractions, a gentle increase in molecular weight (from 500 to 1500) indicates that 60 wt % of the residue is composed of relatively small molecules while large molecules are concentrated in the 40 wt % end cut. Besides the molecular weight distribution of ABVB, the only other useful available properties of ABVB are tabulated in Table 3.11.1.

3.12 Error Analysis

During the entirety of this project, error was continuously being considered. The variables that needed to be known to calculate molar volume were: pressure, temperature, mass of ABVB, mass of dodecane, density of ABVB, density of dodecane, and the volume of each section of the apparatus. The mass measurements and the density of dodecane were accurate to four significant figures, thus they did not contribute significantly to error. The ABVB density, on the other hand, was not as well known but since the volume added was small when compared with the total volume of the system, one can conclude that the error involved due to this quantity is also insignificant. That left temperature, pressure, and number of moles which were direct inputs into the Peng-Robinson equation. By treating the Peng-Robinson equation when considering the sensitivity error of the results, it was found that pressure temperature and number of moles became very important. That was why the pressure transducer was ordered to be accurate to three significant figures. It was also the reason why a great effort was expended to calculate the exact volume of all fittings and stainless steel tubing (Appendix D). It was only in this manner that the hydrogen mass could be obtained accurately.

Chapter 4

NOVEL VARIABLE VOLUME VIEW CELL DESIGN

4.0 Introduction

A novel variable volume view cell design is described in this chapter. This device, created in collaboration with D. B. Robinson Ltd., will greatly simplify our experimental program because smaller samples of fluid is required and few experiments are required per phase diagram. Thus, this new cell allows us to collaborate with other laboratories when only limited quantities of fluids are available. Additional distinguishing features include: (a) the broad range of pressures and temperatures available, the upper extremes are 725 K and 27.5 MPa, (b) the pressure of the mixture can be continually adjusted at a fixed composition and temperature. This is a much broader range of operating conditions than the sandwich cell could address. One of the major obstacles with the view cell described in Chapter 3 is the limitation imposed by the design pressure of the view cell. Details of the general layout, individual components, view cell setup, operation and challenges are also provided in this Chapter.

4.1 Development of a Variable Volume View Cell Suitable for Studying the Phase Behaviour of Opaque Hydrocarbon Systems

During the course of this study a new apparatus has been developed to observe the phase behaviour of opaque organic fluids at elevated temperatures and pressures. Our goal of duplicating the key features of the now classical Cailletet cell [51] was achieved where volume, pressure and temperature could be varied independently over a broad range of temperatures and pressures. Cailletet cells cannot be used with opaque organic fluids as it is not possible to make direct visual assessments of the phases present. Furthermore, the upper temperature limit of the cells is too low to assess key features of the diagrams for many fluids of interest such as mixtures including heavy oil and bitumen among the components [13]. The new apparatus does not suffer from these deficiencies because it makes use of transmitted x-rays instead of visible light as the basis for phase detection and a stainless steel bellows rather than a mercury column to vary cell volume. Key features of the apparatus include: a maximum operating pressure of 27.5 MPa, maximum operating temperature of 725 K, and a variable cell volume ranging from 10 cm^3 to 175 cm^3. Condensed phase densities are resolved to within +/- 0.02 g/cm^3, and phase boundaries are resolved to within +/- 3 K and +/- 0.035 MPa. The appearance of dispersed solid phases can also be detected [18]. The x-ray view cell apparatus, was built with the assistance and collaboration of AMOCO Oil (USA), CANMET, NSERC, and D. B. Robinson & Associates Ltd.. The variable volume view cell is described briefly below. Further details can be found in the view cell equipment manual [52].

4.2 High Temperature Beryllium X-ray View Cell

The high temperature beryllium x-ray cell (Figure 4.2.1) was designed and manufactured to assist the study of heavy bitumen oil coking behaviour. Sample observations with x-rays are taken on a plane coincident with the cylinder axis and may be made over the entire cell length. The maximum window aperture width is limited to the distance between adjacent steel tension bolts - about 2 cm.

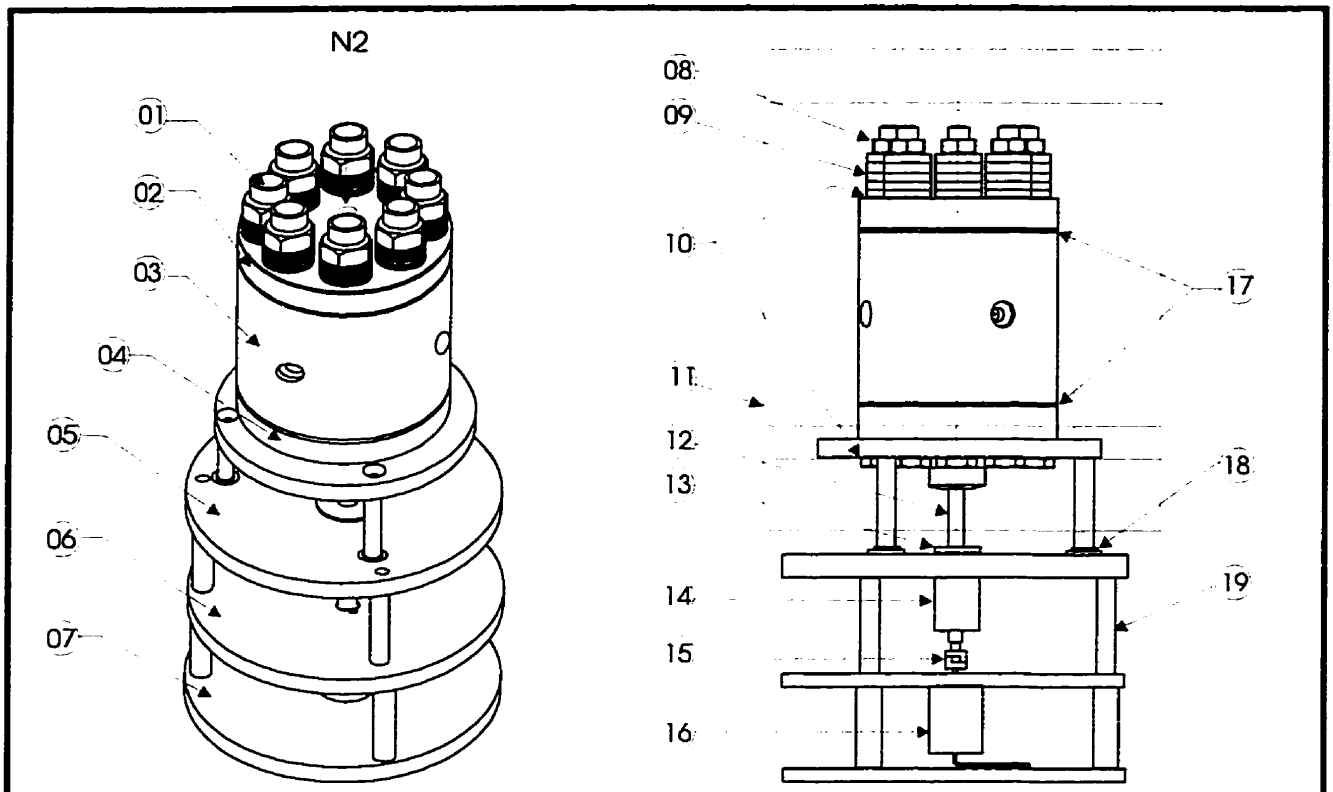

Reference Drawing	Description	Material
01	Capscrews 5/8-11 UNC x 9-1/2 Special	SA-193 Gr B16
02	Bellows Cap Assembly (w/Top Cap)	316 SS
03	Cylinder	Beryllium
04	Magnetic Drive Cap	316 SS
05	Locating Plate for Cell Bottom	316 SS
06	Motor Mount Plate	316 SS
07	Base Plate	316 SS
08	Hex Nut 5/8-11 UNC	SA-194 Gr B16
09	Belleville AFB 2-60	Alloy Steel
10	Washer 5/8 Seastrom SS T304	304 SS
11	Heating Jacket	
12	Upper Locating Arm	316 SS
13	Insulating Collar	Celazole PBI
14	Magnet	
15	Lovejoy Coupling I-035 3/16'	
16	Motor DC-GLOBE 100A821BL-HI-TEMP	
17	Gasket- Spiral Wound	316 SS
18	Mixer Cage Base Plate With Spacer Rods	316 SS
19	Stepped Standoff	304/316 SS

Figure 4.2.1 High temperature beryllium cell

There are five ports on the cell: one on top and four around the cell body. The ports have been carefully arranged with their lines and fittings, and allow a clear view of the x-ray window aperture. The top port is for the nitrogen gas supply, and has been drilled and threaded to a standard HIP AF2 profile with a 1/16" port into the cell body. The remaining four ports around the cell are set 90° apart and outside the x-ray view plane. The largest of these is the "Flush" port. It has been drilled and threaded to a standard HIP AF2 with a 1/8" port into the cell body. With the nitrogen gas port on top, and working clockwise around the cell body from the "Flush" port, the remaining ports are "Thermocouple", "Injection" and "Process". These three ports have been drilled and threaded to standard HIP AF2 profile, and each has been drilled with a 1/16" diameter hole into the cell body.

The injection port has been set lower in the cell body to allow the sample under study to be sent directly into the mixer stream. The nitrogen line has been plumbed straight on up from the cell cap. The "Flush", "Process" and "Injection" lines have been plumbed around the upper cell body and brought out of the heating jacket with the thermocouple leads. The heating jacket is controlled by a 1500 Watt control with separate cords to each side of the jacket. This system is rated to a maximum temperature of 725 K. The cell is provided with a custom designed magnetically-coupled mixing device to reduce the sample equilibration time and improve charge homogeneity. In order to make sure a known amount of materials were loaded into the view cell, there was a complicated plumbing procedure for the cell as shown in Figure 4.2.2. The advantages of a variable-volume x-ray beryllium cell apparatus are:

- The experimental design and procedures are straightforward;
- The phase transitions are determined visually (using x-ray), the phase inversions are easily detected;
- Heavy oil/bitumen and generally opaque fluid can be studied; and
- The pressure of the mixture can be continuously adjusted at a fixed composition and temperature.

The disadvantages are:

- The compositions of the equilibrium phase are not determined.

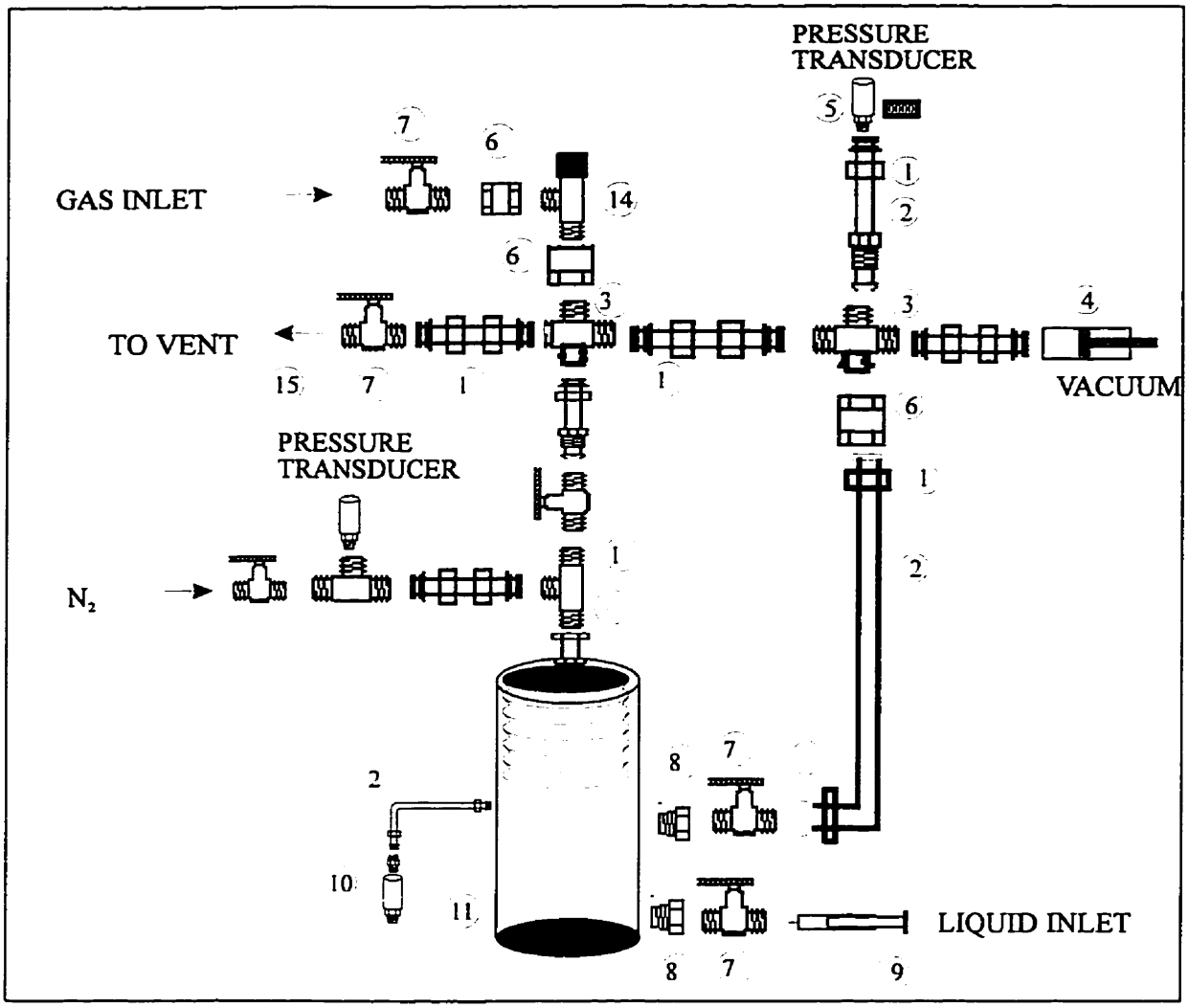

ITEM	QUANT.	DESCRIPTION	PART NO.	SUPPLIER
1	14	SWAGE-LOC NUT FERRULE SET	SS-102-1	AVON VALVE
2		TUBING 1/16" O.D. X 0.04" I.D., STAINLESS STEEL	SS-104-1	AVON VALVE
3	1	UNION CROSS	SS-200-4	AVON VALVE
4	1	VACUUM PUMP	N/A	N/A
5	1	PRESSURE TRANSDUCER 1/4 NPT MALE 0-2000 PSI	1241-0005-2200	DURHAM
6	5	FEMALE CONNECTOR 1/16" SWAGE-LOK	N/A	N/A
7	6	BALL VALVE 1/16" SWAGE-LOK ENDS	SS-41S1	AVON VALVE
8	3	ADAPTER 1/16" O.D. TUBE X 1/8" TAPER SEAL	15-21AF1AM2	HOKS
9	1	SYRINGES	N/A	N/A
10	1	RUPTURE DISC	N/A	N/A
11	1	HIGH TEMPERATURE BERYLLIUM CELL	0100-040-450	DB ROBINSON
12	1	HYDROGEN TANK, 2200 PSI	N/A	CANOX
13	1	NITROGEN TANK, 2200 PSI	N/A	CANOX
14	1	UNION TEE 1/16" SWAGE-LOK ENDS	SS-100-3	AVON VALVE
15	1	TO ATMOSPHERE	N/A	N/A

Figure 4.2.2 Plumbing detail schematic

4.3 Specifications and Features

Maximum pressure:	27.5 MPa
Maximum Temperature:	725 K
Wetted Materials:	Beryllium S-200-F; Type 316 SS
Stirrer Speed:	Variable from 300 RPM to 2600 RPM
Sample Port Size:	0.067"
Sample Port Connection:	1/8 HIP
Power Requirements:	Heating Jacket: 230 Volt, 50/60 Hz, 1500 Watt
	Mixer Speed Controller: 120/230 Volt, 50/60 Hz, 1500 Watt

The x-ray cell is equipped with a high speed, high temperature, magnetically-coupled mixer. With a special high temperature bearing cage, magnets, bearings and other high temperature materials, this mixer is designed to run continuously at maximum speed, temperature and pressure. The mixer motor is a high temperature, brush type, electric motor with a 10 to 100% hand speed control.

The cell's solid beryllium cylinder is for use with high-power x-ray apparatus. The cylinder measures 5" O.D. x 2" I.D. x 5" long. Arranged around the cell are four HIP ports for the injection and sampling of working and control fluids. With stainless steel caps on both top and bottom, the top cap incorporates an expanding bellows to allow variable cylinder volume (Figure 4.3.1). Eight tension through-bolts, of a high temperature alloy, and sealing caps with Flexitalic stainless spiral-wound gaskets complete the assembly.

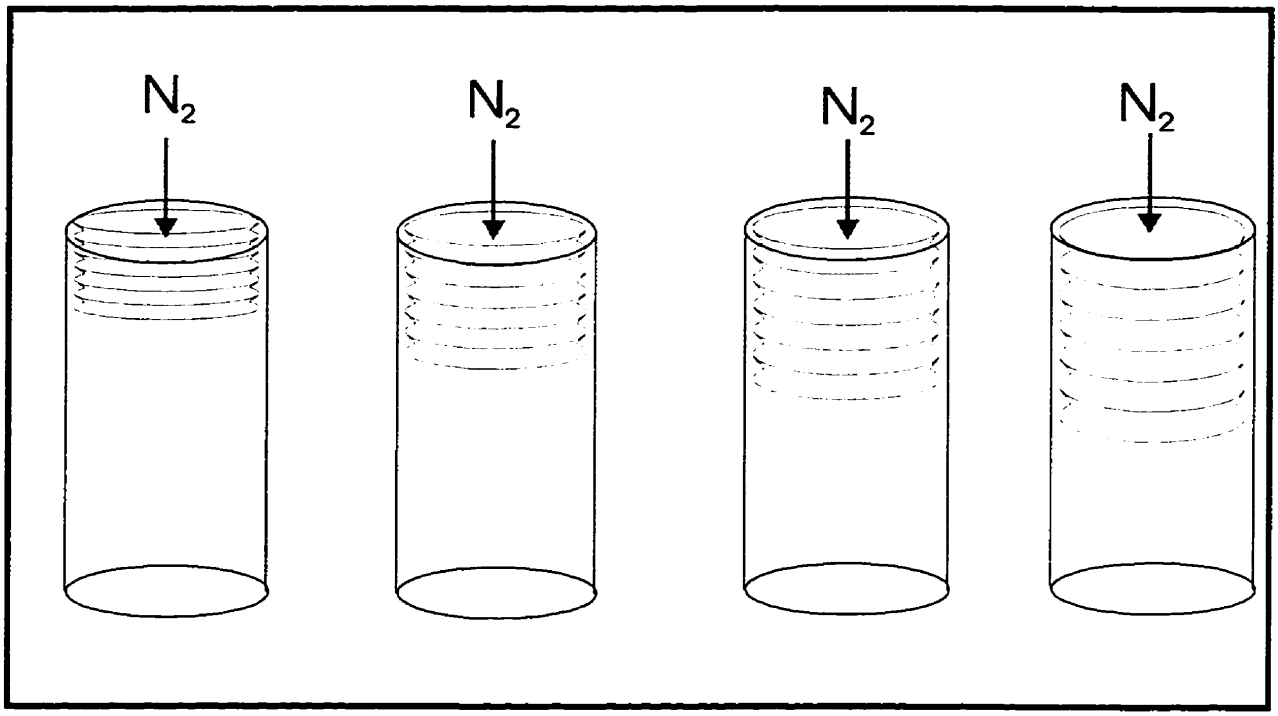

Figure 4.3.1 Stainless steel bellows

4.4 *Heating Jacket Control System*

Heating is provided by a custom-designed heating jacket. It is refractory-insulated vestibule type (1500 Watt, 230 Volt), with a stainless steel covering and a programmable controller. The x-ray cell is heated with radiant heaters encased in a heating jacket. Temperature is controlled by a time proportioning controller and thermocouple sensing element. The controller is housed in an enclosure. The radiant heaters are connected to the rear of the control enclosure by a pair of interchangeable cable connectors.

The control enclosure houses the time proportioning temperature controller. A lead indicator on the controller panel cycles on and off as power is switched to the heaters. To protect the radiant heaters, a ramping setpoint controller is used. Ramping the setpoint reduces the possibility of applying full power to the heaters for sustained periods. Applying full power to the heaters for sustained periods may result in premature failure.

The two built-in Boron Nitride windows measure 1" x 4". Even at maximum temperature, these windows may be removed by a suitably gloved hand for improved x-ray penetration or inspection. Special insulation bushings limit the heat loss through the mixer driveshaft and provide thermal isolation of the motor, the driveshaft bearing assembly and other lower assembly components.

4.5 Density Calibration with Cell B

The new cell was calibrated in the same manner as the old cell. The new calibration curve involved taking a series of 8 images at different time intervals for a specific substance and then averaging the values to account for the variability coming from the x-ray source and equipment noise. The data were then compiled and analyzed. The results are plotted on a semi-log graph of intensity versus the density of various hydrocarbons, Figure 4.5.1. From a linear least squares fit to the data, the intensity versus density relationship was found to be ln(Y)= 0.9 d + 4.621. The slope of line for the new cell is 0.90 (see appendix A).

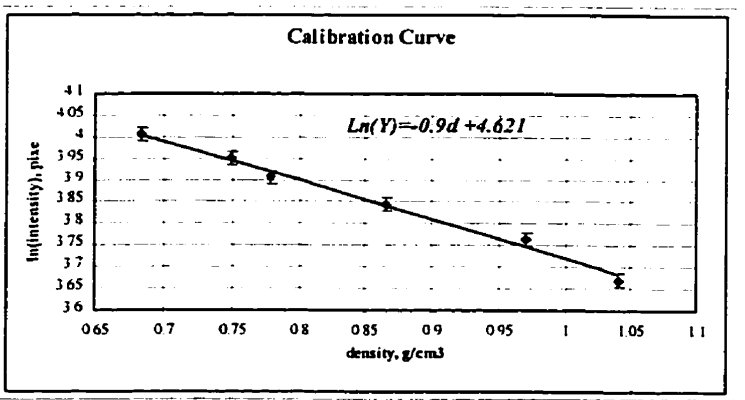

Figure 4.5.1 Calibration curve for the x-ray cell B

4.6 Methods for Determining Phase Boundaries

The procedure for measuring a specific type of phase equilibrium for a ternary system depends on the number of coexisting phases. The Gibbs phase rule applied to a ternary system results in F= C - π +2= 5-π. For a three-phase equilibrium, F=2, therefore two field variables can be adjusted (bivariant equilibrium). Thus, setting the temperature to a certain value only the pressure remains free. A data point is obtained in the following manner. The cell is initially loaded with a measured amount of liquid or solid and purged five times or more at room temperature with the gas of interest at ~ 0.4 MPa to remove any trapped air. Gas is then transferred into the cell from a high-pressure cylinder. The feed can be compressed to the desired operating pressure by displacing a nitrogen-driven bellows fitted within the cell. For the case of vapour-liquid equilibrium in the LV-L phase boundary a point is obtained in the following manner. At a fixed temperature the mixture in the cell is compressed to a single phase at high pressures. The pressure is then slowly decreased until a second phase appears. If a liquid solute is being studied, the vapour-liquid phase transition is determined in this manner. The decompression step is performed very slowly. If the pressure of the system is within ~ 0.2 MPa of the phase-split pressure, the rate of decompression is usually maintained at ~ 0.006 MPa/sec. The actual phase transition for the liquid solute is in the pressure interval between this two-phase state and the previous single, fluid-phase state. The entire procedure is then performed several times to decrease the pressure interval from two phases to one phase, so it falls within an acceptable range. The system temperature is now raised and the entire procedure is repeated to obtained more vapour-liquid equilibrium (VLE) information without having to reload the cell. In this manner, without sampling, an isopleth (constant composition at various temperatures and pressures) is obtained. Typically the image of the mixture in the cell is projected onto a video monitor using an image intensifier and a Pulnix camera. The arrangement of the experimental set-up is shown in Figure 4.6.1. In Figure 4.6.2 several two and three phase situations for ternary mixtures, as they may appear in the view cell, are drawn schematically. The advantage of a variable-volume x-ray beryllium cell apparatus is that the pressure of the mixture can be continually adjusted at a fixed composition and temperature.

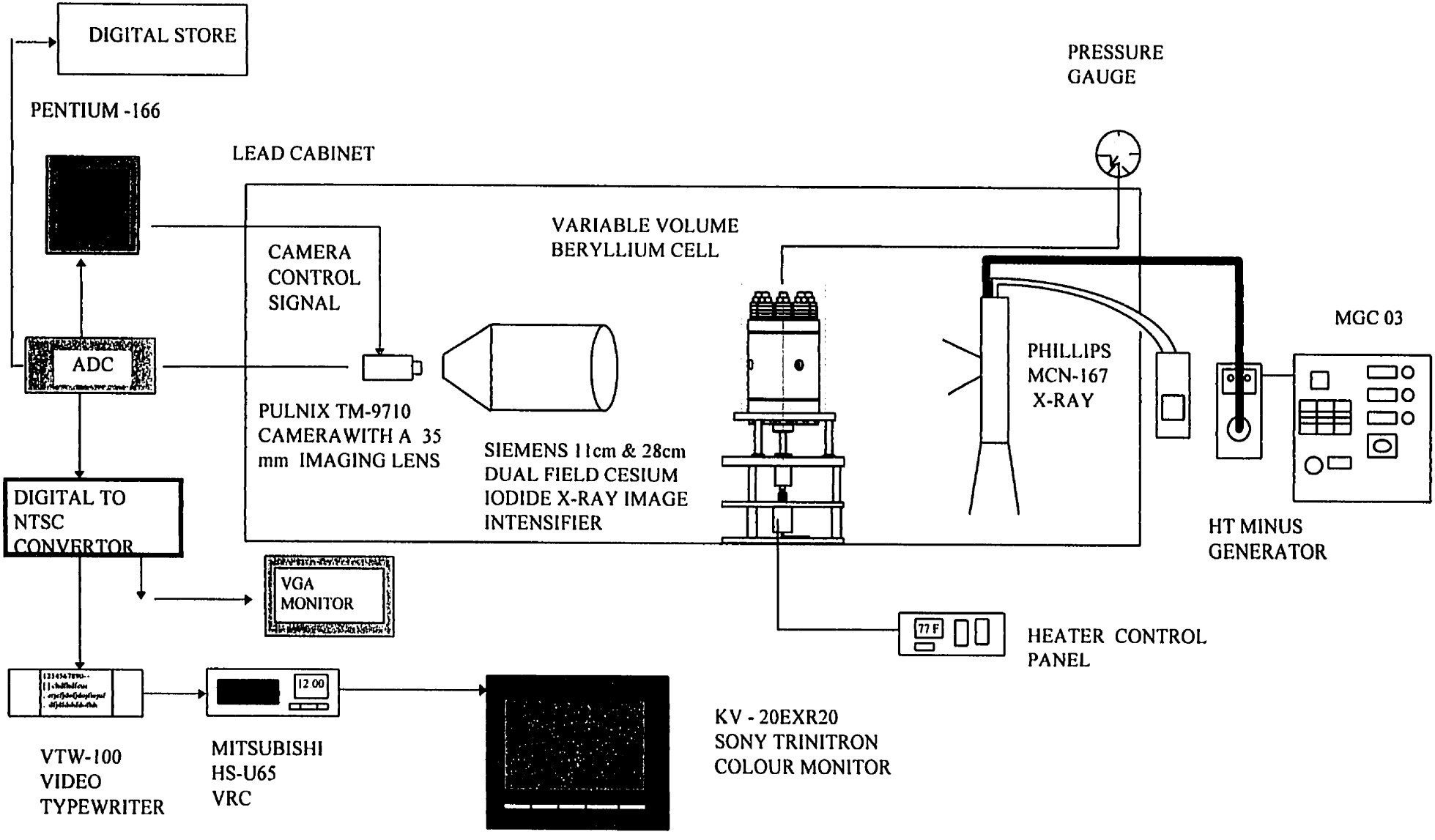

Figure 4.6.1 - New Experimental set-up

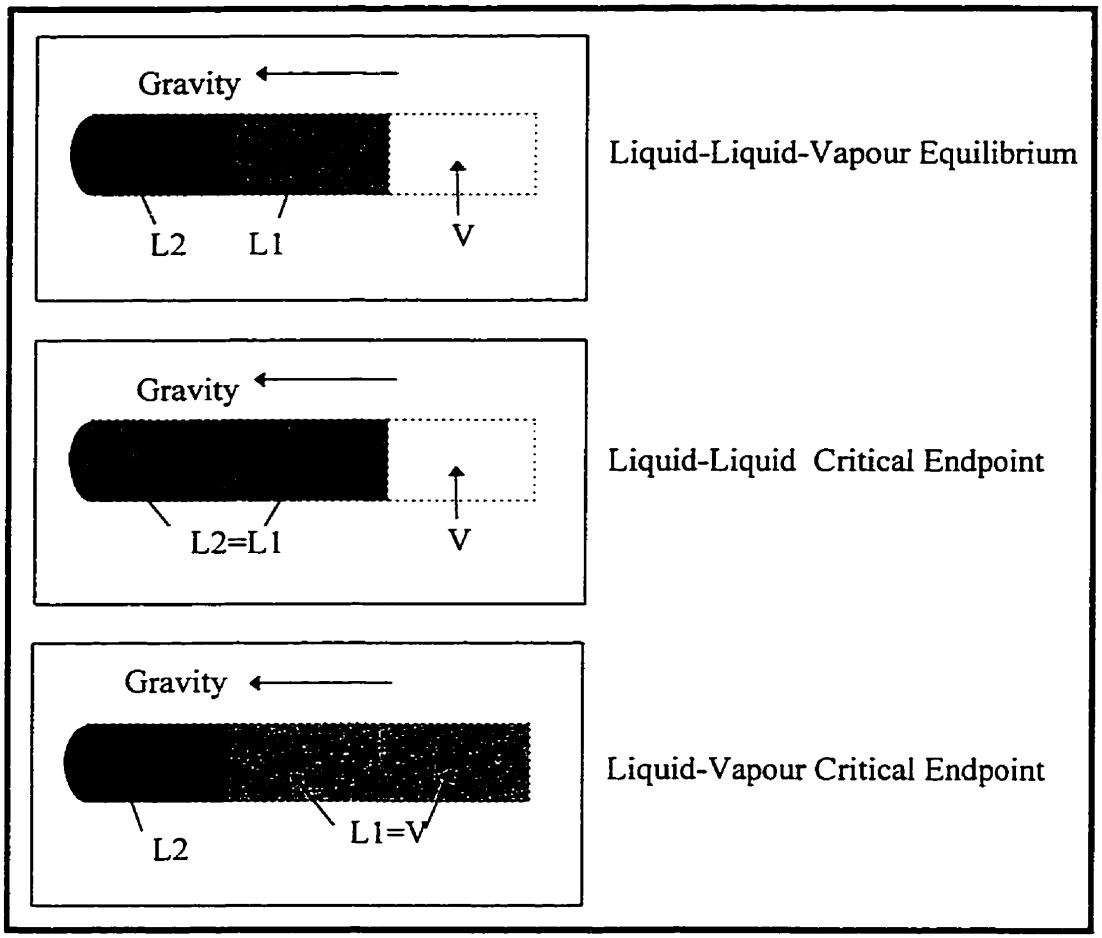

Figure 4.6.2 Some cases of fluid phase equilibria in the mixtures as may be observed with the imaging system

Chapter 5

RESULTS & DISCUSSION

5.1 Phase Behaviour of Athabasca Bitumen + n-Dodecane / Toluene + Hydrogen

A series of experiments was performed with these model heavy oil systems to identify the pressure and temperature region where multiple phases co-exist. The system athabasca-bitumen-vacuum-bottom (ABVB) + n-dodecane + hydrogen was chosen because the critical temperature of n-dodecane was within the temperature range of operating conditions used in heavy oil upgrading processes and because n-dodecane is a model aliphatic diluent. The total volume of mixture used in experiments was chosen to ensure that the phase behaviour of the system would be visible by the image intensifier. The initial hydrogen pressure was calculated to ensure that the pressure at high temperature would not exceed the maximum allowable working pressure of 7 MPa. Experiments were conducted at various temperatures between 298 and 701 K and pressures between 1.05 and 6.96 MPa. The primary information obtained was whether or not multiple phases were observed at the test pressures and temperatures and the density of liquid and solid phases present. Another series of experiments was performed with the system ABVB + toluene + hydrogen where toluene is a model aromatic solvent. For most of the experiments, the mass compositions for the two systems were held constant and equal (ABVB (2 mole % or 24.6 wt %) + dodecane (47

mole % or 73.8 wt %) + hydrogen (51 mole % or 1.6 wt %)). The ABVB (2 mole % or 24.8 wt %) + toluene (62 mole % or 74.3 wt %) + hydrogen (36 mole % or 0.9 wt %) system exhibited only LV phase behaviour in the temperature range 425 K to 725 K and the pressure range 1 MPa to 7 MPa whereas the ABVB + n-dodecane + hydrogen system exhibited complex reversible and irreversible phase behaviour, under the same conditions.

A list of the experiments performed and the key results are given in Table 5.1.1 and Table 5.1.2. Representative sample digitized images showing liquid-vapour and liquid-liquid-vapour phase behaviour are shown in Figure 5.1.1. A number of experiments were repeated because of reactor leaks. Example of pressure-temperature trajectories are shown in Figure 5.1.2 and 5.1.3. Because cell "A" has a constant volume, a series of experiments were required to construct each P-T diagram where the composition was held constant but the total mass added to the cell was varied. Run# 2 exhibited very complex phase transitions, i.e., phase transitions such as solid-liquid-vapour to liquid-vapour to liquid-liquid-vapour to solid-liquid-liquid-vapour to solid-liquid-vapour. The pressure-temperature trajectory for run# 2 is shown in Figure 5.1.4. Runs# 4, 20, and 22 exhibit liquid-vapour phase behaviour.

Table 5.1.1 Observed phase transitions for ABVB + *n*- $C_{12}H_{26}$ / C_7H_8 + H_2 mixtures

Run#	Mass of ABVB (g)	Mass of Dodecane (g)	Mass of Toluene (g)	Mass of Hydrogen (g)	wt % of ABVB	Phase Transition
2	125	150		1.92	45	SLV→LV→LLV →SLLV→SLV
4	37.5	150		1.92	25	SLV→LV
6	75	225		2.88	25	SLV→LV→ LLV→LV
7	62.5	187.5		2.40	25	SLV→LV→ LLV→LV
8	50	150		1.92	25	SLV→LV→ LLV→LV
9	87.5	262.5		3.36	25	SLV→LV→ LLV→LV
10	68	204		2.61	25	SLV→LV→ LLV→LV
11	62.5		187.5	2.39	25	SLV→LV
12			257			LV→V→LV
13	50		150	1.91	25	SLV→LV
16	75		225	2.87	25	SLV→LV
17	100		300	3.82	25	SLV→LV
20	30	90		1.15	25	SLV→LV
22	40	120		1.54	25	SLV→LV
23	45	135		1.73	25	SLV→LV→ LLV→LV

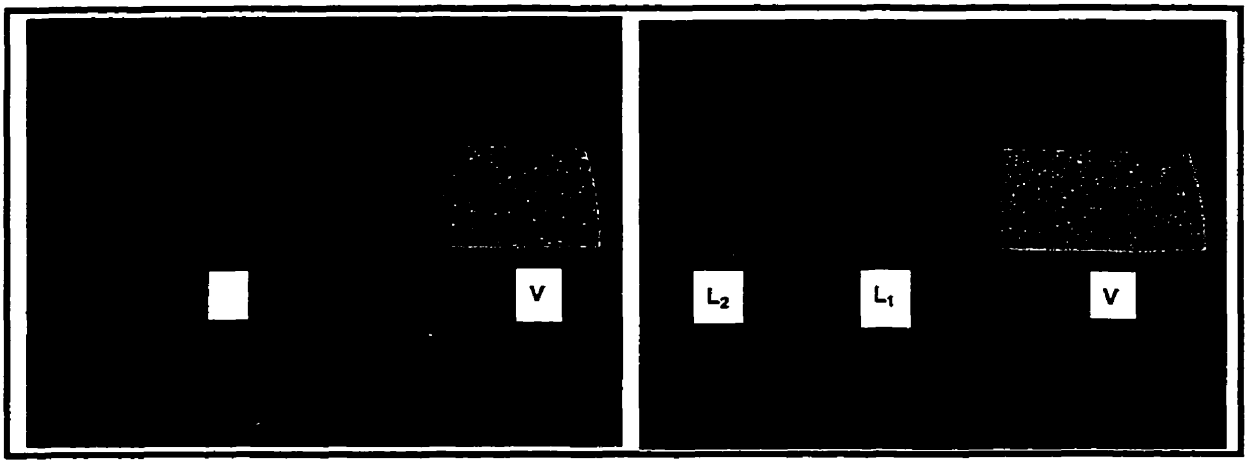

Figure 5.1.1 Representative digitized images showing liquid-vapour and liquid-liquid-vapour phase behaviour

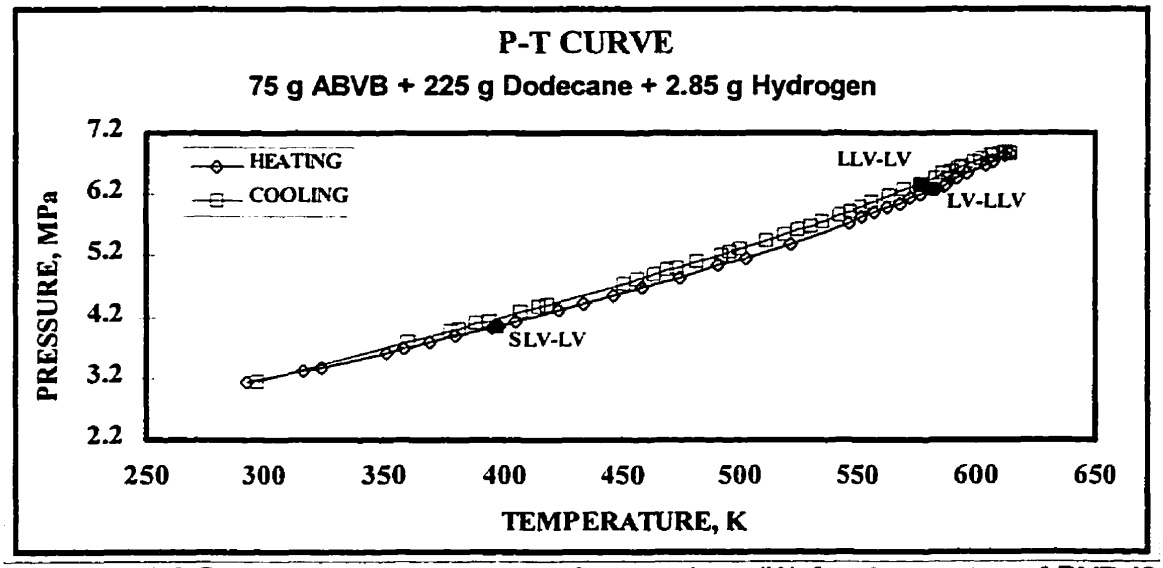

Figure 5.1.2 Pressure-Temperature trajectory (run #6) for the system ABVB (2 mole %) + *n*- $C_{12}H_{26}$ (47 mole %) + H_2 (51 mole %).

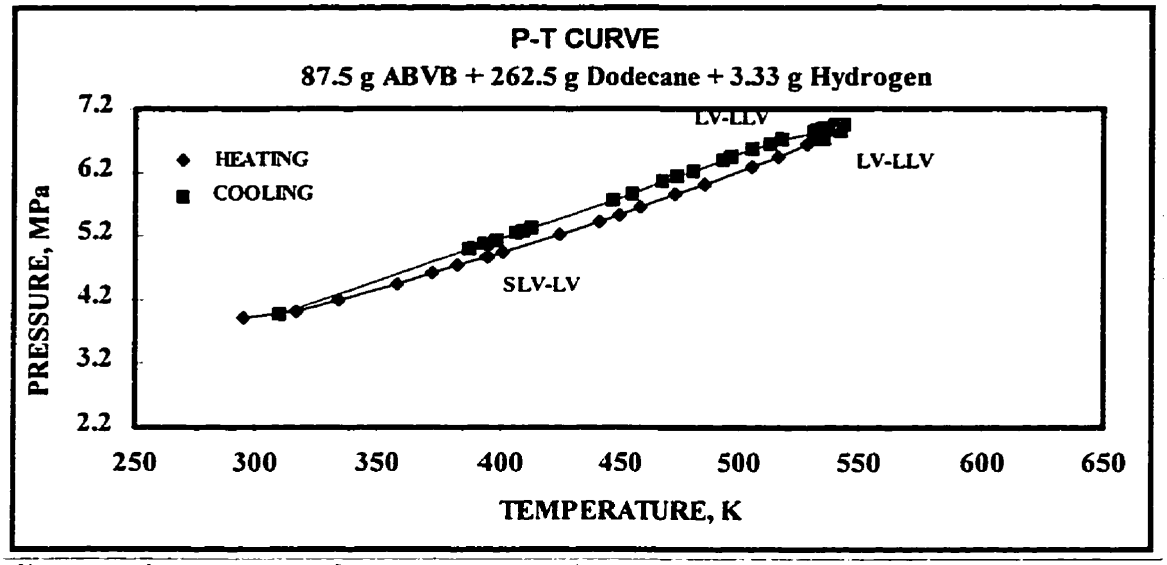

Figure 5.1.3 Pressure-Temperature trajectory (run #9) for the system ABVB (2 mole %) + *n*- $C_{12}H_{26}$ (47 mole %) + H_2 (51 mole %).

Table 5.1.2 Observed phase transitions for ABVB + n-dodecane + hydrogen

	Phase Transition	Temperature, K	Pressure, MPa
Run# 2	SLV to LV	413	2.67*
	LV to LLV	648	5.20
	LLV to SLLV	669	5.6
	SLLV to SLV	682.5	5.89
Run# 6	SLV to LV	396.9	4.05*
	LV to LLV	580.5	6.31
Run# 7	SLV to LV	401.9	3.26*
	LV to LLV	596	5.25
Run# 8	SLV to LV	453	2.81*
	LV to LLV	580.5	4.01
Run# 9	SLV to LV	394.7	4.89*
	LV to LLV	533.5	6.79
Run# 10	SLV to LV	403.0	3.52*
	LV to LLV	590.0	5.68

* Dissolution of solid. The ABVB + diluent mixtures are not at equilibrium initially.

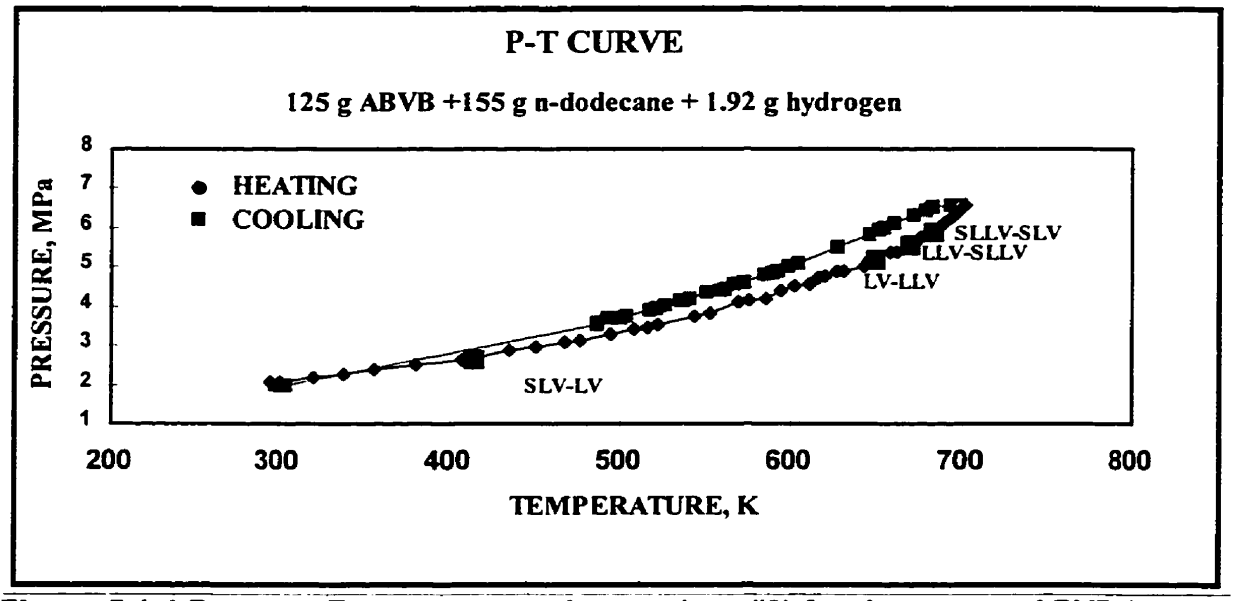

Figure 5.1.4 Pressure-Temperature trajectory (run #2) for the system ABVB (6 mole %) + *n*- $C_{12}H_{26}$ (45 mole %) + H_2 (49 mole %)

5.2 *Reversible & Irreversible Multiphase Behaviour For The System: ABVB + n-Dodecane + Hydrogen*

Observed reversible phase transitions for the mixture ABVB (2 mole % or 24.6 wt. %) + dodecane (47 mole % or 73.8 wt %) + hydrogen (51 mole % or 1.6 wt %) are shown in Table 5.2.1. Note the reproducibility of the $L_1V \rightarrow L_1L_2V$ boundaries for heating and cooling. Temperatures were repeatable to within 3 K and pressures to within 0.03 MPa. These data, in conjunction with experiments performed at lower pressures which showed only L_1V phase behaviour, were used to construct a partial phase diagram for this system in the temperature range 425 K to 725 K and the pressure range 2 MPa to 7 MPa as shown in Figures 5.2.1 and 5.2.2. The designation of the liquid phases as L_1 and L_2 is obtained from the density data, Tables 5.2.2 to 5.2.9, where L_1 is the less dense and L_2 the more dense phase.

Table 5.2.1 Reversible phase boundary data for ABVB (2 mole %) + dodecane (47 mole %) + hydrogen (51 mole %).[ABVB(24.6 wt. %), dodecane (73.8 wt. %), hydrogen(1.6 wt. %)]

$L_1V \rightarrow L_1L_2V$ ($L_1L_2V \rightarrow L_1V$)		$L_1L_2V \rightarrow L_1V$	
T/K	P/ MPa	T/K	P/MPa
546.34 (NA)	3.23 (NA)	611.34	3.99
580.5 (588.2)	4.01 (4.1)		
596 (NA)	5.25 (NA)		
590 (597)	5.68 (5.77)		
580.5 (583)	6.31 (6.27)		
533.5 (531)	6.79 (6.75)		

In addition to the reversible two phase L_1V and three phase L_1L_2V phase behaviour over parts of this P-T region shown for this system, irreversible bulk "solids dropout" arose within the L_2 phase which in this context co-exists with the L_1 and V phases. Bulk "solids dropout" did not arise in the absence of the L_2 phase, i.e., within the L_1V region, even at temperatures in excess of 700 K. These data provide a strong link between bulk "solids dropout" and multiphase behaviour. The irreversible phase behaviour (solids dropout) was detected by irreversible L_1L_2V to L_1V phase boundary measurements on cooling and confirmed by apparent density measurements of the L_2 phase. These issues are addressed in more detail in Section 5.7. Transitions between the multiphase regions were found to be reversible at temperatures less than 655 K.

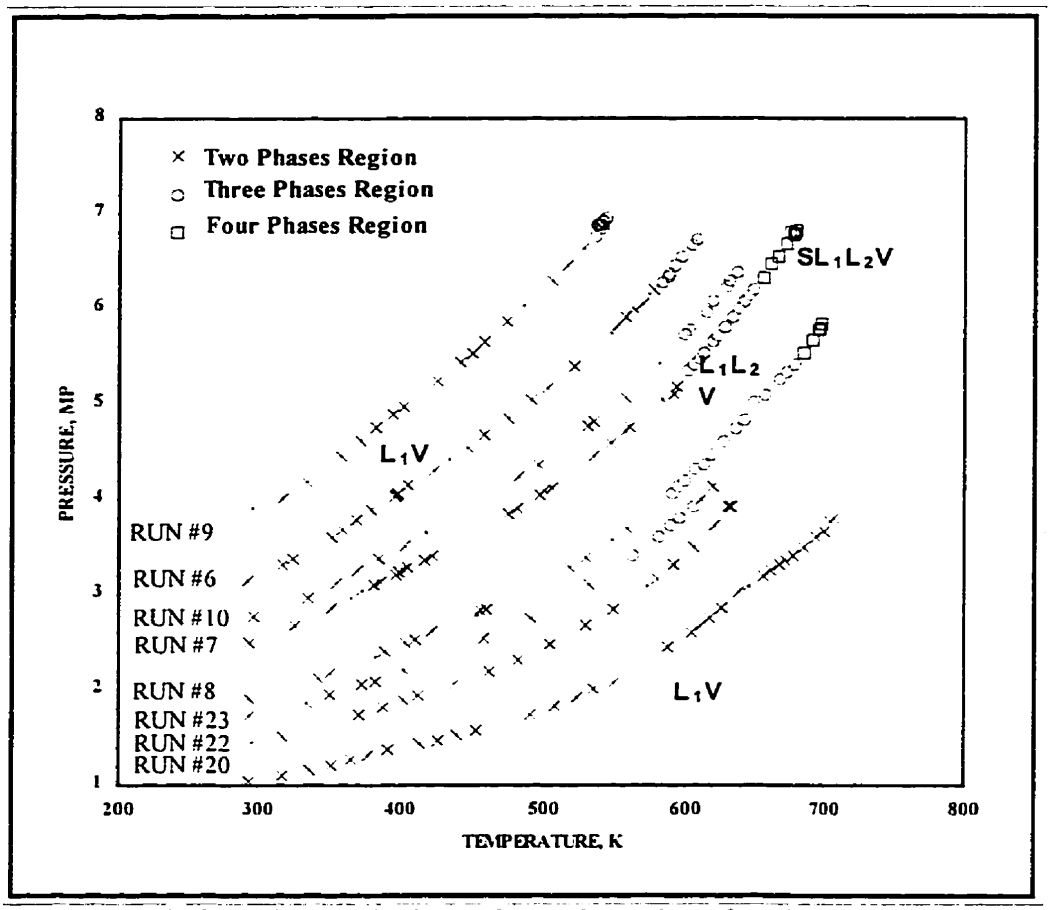

Figure 5.2.1 Experimental phase boundary data for the system ABVB (2 mole %) + *n*- $C_{12}H_{26}$ (47 mole %) + H_2 (51 mole %).

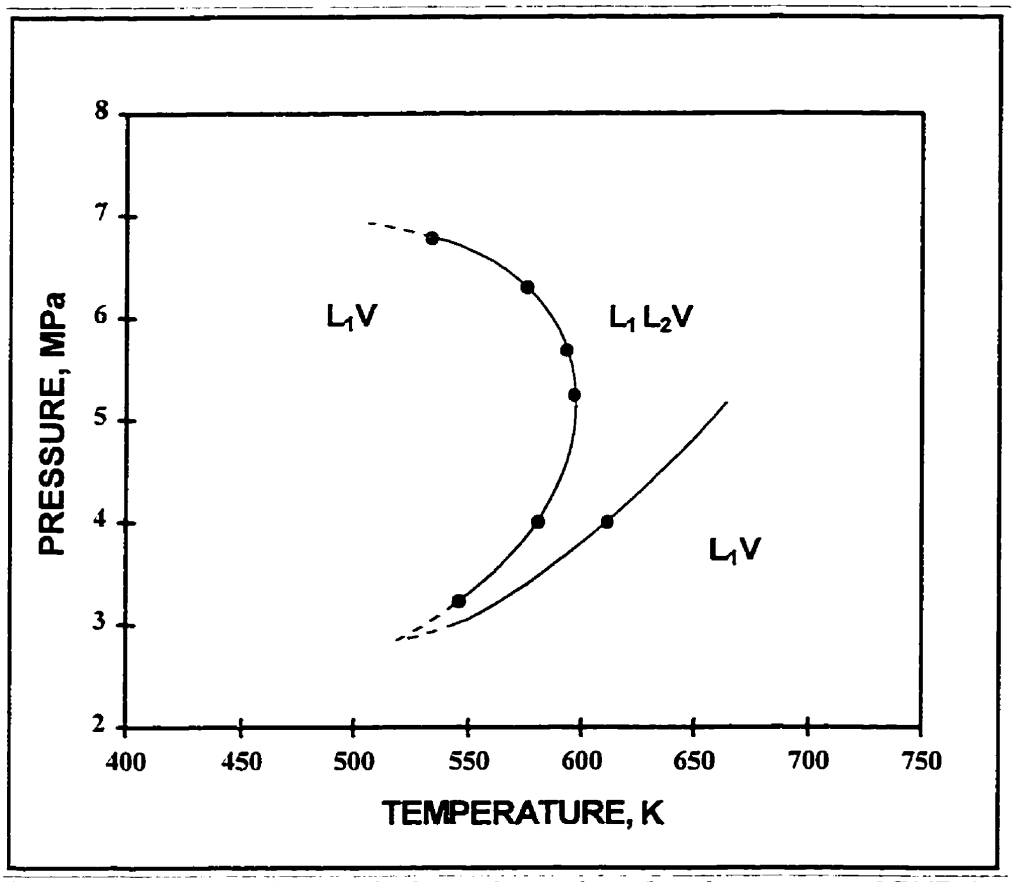

Figure 5.2.2 Experimental phase boundary for the system ABVB (2 mole %) + *n*- $C_{12}H_{26}$ (47 mole %) + H_2 (51 mole %). The shaded zone within the L_1L_2V region is the interval where unusual retrograde condensation occurs.

Table 5.2.2 Density analysis, 30 g ABVB + 90 n-dodecane + 1.15 g hydrogen (Run# 20).

Temperature (K)	Pressure (MPa)	Phase	Density of L_1 (g/cm^3)
535.8	2.01	LV	0.77
587	2.45	LV	0.79
610.7	2.69	LV	0.82
625.8	2.86	LV	0.83
671.9	3.36	LV	0.87
706.7	3.8	LV	0.89

Table 5.2.3 Density analysis, 40 g ABVB + 120 g n-dodecane + 1.54 g hydrogen (Run# 22).

Temperature (K)	Pressure (MPa)	Phase	Density of L_1 (g/cm^3)
462.5	2.2	LV	0.75
505	2.48	LV	0.77
549.7	2.85	LV	0.79
580	3.17	LV	0.80
605	3.49	LV	0.82
632	3.92	LV	0.85

Table 5.2.4 Density analysis, 45 g ABVB + 135 g n-dodecane + 1.73 g hydrogen (Run# 23).

Temperature (K)	Pressure (MPa)	Phase	Density of L_1 /L_2 (g/cm^3)
491	2.76	LV	0.77
595.8	3.8	LLV	0.82/1.02
605.8	3.93	LLV	0.83/1.03
611.3	3.98	LV	0.84

Table 5.2.5 Density analysis, 50 g ABVB + 150 g n-dodecane + 1.92 g hydrogen (Run# 8).

Temperature (K)	Pressure (MPa)	Phase	Density of L_1 /L_2 (g/cm^3)
595.2	4.1	LLV	0.81/1.06
635.8	4.7	LLV	0.86/1.08
673	5.33	LLV	0.89/1.15*
693	5.71	LLV	0.91/1.18*

*** Apparent liquid density.**

Table 5.2.6 Density analysis, 62.5 g ABVB + 187.5 g n-dodecane + 2.40 g hydrogen (Run# 7).

Temperature (K)	Pressure (MPa)	Phase	Density of L_1 /L_2 (g/cm^3)
500.8	4.12	LV	0.78
583.5	5.04	LV	0.79
605.2	5.41	LLV	0.80/1.06
623	5.71	LLV	0.85/1.07
641.3	6.07	LLV	0.86/1.08
648	6.20	LLV	0.87/1.08
660.8	6.47	LLV	0.89/1.17*
680.2	6.82	LLV	0.91/1.18*

*** Apparent liquid density.**

Table 5.2.7 Density analysis, 68 g ABVB + 204 g n-dodecane + 2.61 g hydrogen (Run# 10).

	Temperature (K)	Pressure (MPa)	Phase	Density of L_1 /L_2 (g/cm^3)
H	535.8	4.8	LV	0.78
H	602.4	5.77	LLV	0.81/1.08
H	619.7	6.07	LLV	0.84/1.09
H	631	6.29	LLV	0.86/1.10
H	644.1	6.65	LLV	0.88/1.11
C	616.3	6.2	LLV	0.83/1.08
C	604.1	5.98	LLV	0.81/1.07
C	568	5.43	LV	0.80
C	498	3.47	LV	0.78

H: HEATING ; C:COOLING

Table 5.2.8 Density analysis, 75 g ABVB + 225 g n-dodecane + 2.88 g hydrogen (Run# 6).

	Temperature (K)	Pressure (MPa)	Phase	Density of L_1 /L_2 (g/cm^3)
H	502.4	5.17	LV	0.78
H	563.6	5.99	LV	0.80
H	577.4	6.2	LV	0.81
H	583	6.27	LV	0.82
H	596.9	6.55	LLV	0.83/1.09
H	615.8	6.9	LLV	0.84/1.10
C	602.4	6.8	LLV	0.83/1.08
C	594.6	6.65	LLV	0.82/1.07
C	584.1	6.48	LLV	0.82/1.06
C	524	5.63	LV	0.81

H: HEATING ; C:COOLING

Table 5.2.9 Density analysis, 87.5 g ABVB + 262.5 g n-dodecane + 3.36 g hydrogen (Run# 9).

Temperature (K)	Pressure (MPa)	Phase	Density of L_1 /L_2 (g/cm^3)
536.3	6.78	LLV	0.80/0.99
541.3	6.89	LLV	0.81/1.01
543.6	6.96	LLV	0.82/1.01

5.3 *Unusual Retrograde Condensation for the system ABVB (2 mole %) + n- $C_{12}H_{26}$ (47 mole %) + H_2 (51 mole %)*

The shape of the low temperature boundary between the L_1V and L_1L_2V zones, in Figure 5.2.2 is characteristic of a dilute asymmetric mixture where a heavy liquid phase, L_2, appears then disappears within the light liquid phase, L_1, on isothermal compression. Such phase behaviour is referred to as unusual retrograde condensation, and is shown schematically in Figure 5.3.1 and is of both practical and theoretical interest. A small mole/mass fraction of ABVB appears to be the source of the complex phase behaviour.

The shaded zone within the L_1L_2V region, Figure 5.2.2, denotes the interval over which unusual retrograde condensation occurs. Unusual retrograde condensation is an

important though rare phenomenon arising in asymmetric mixtures [9,24,33]. This is only the second large scale occurrence reported [25]. However, based on our understanding of this phenomenon we can sketch the balance of the phase diagram, Figure 5.3.2. Both sketches are obtained by expanding a Type V binary to a multiple component case, Figure 5.3.3 and only differ with respect to composition. Figure 5.3.2a corresponds to a higher heavy hydrocarbon content case and is more likely than Figure 5.3.2b which corresponds to a less concentrated case. A third possibility shown in Figure 5.3.3d can be eliminated based on the data. However, in the absence of high pressure data, a definitive categorization cannot be made. At the highest concentrations of the heaviest component, the L-point is not observed and L_2V phase behaviour arises at low pressure. This case is not appropriate because such a mixture does not exhibit unusual retrograde condensation of a second heavier liquid. Decreasing the mole fraction of the heaviest component to moderate values reveals both L-points and the K-points. Figure 5.3.2a and 5.3.3e give the expected phase diagram of such a system. The possibility of unusual retrograde condensation of the second heavier liquid is found in the vicinity of the L-point. At the lowest concentration of the heaviest component, the K-point is not observed. Figure 5.3.2b and 5.3.3f give the expected phase diagram for such a system.

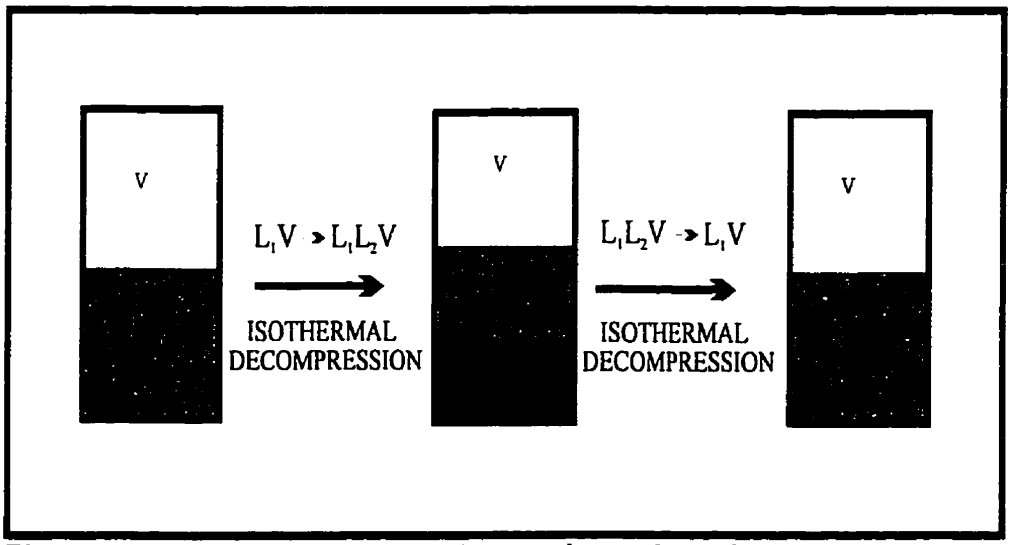

Figure 5.3.1 Unusual retrograde condensation, decrease pressure at constant temperature.

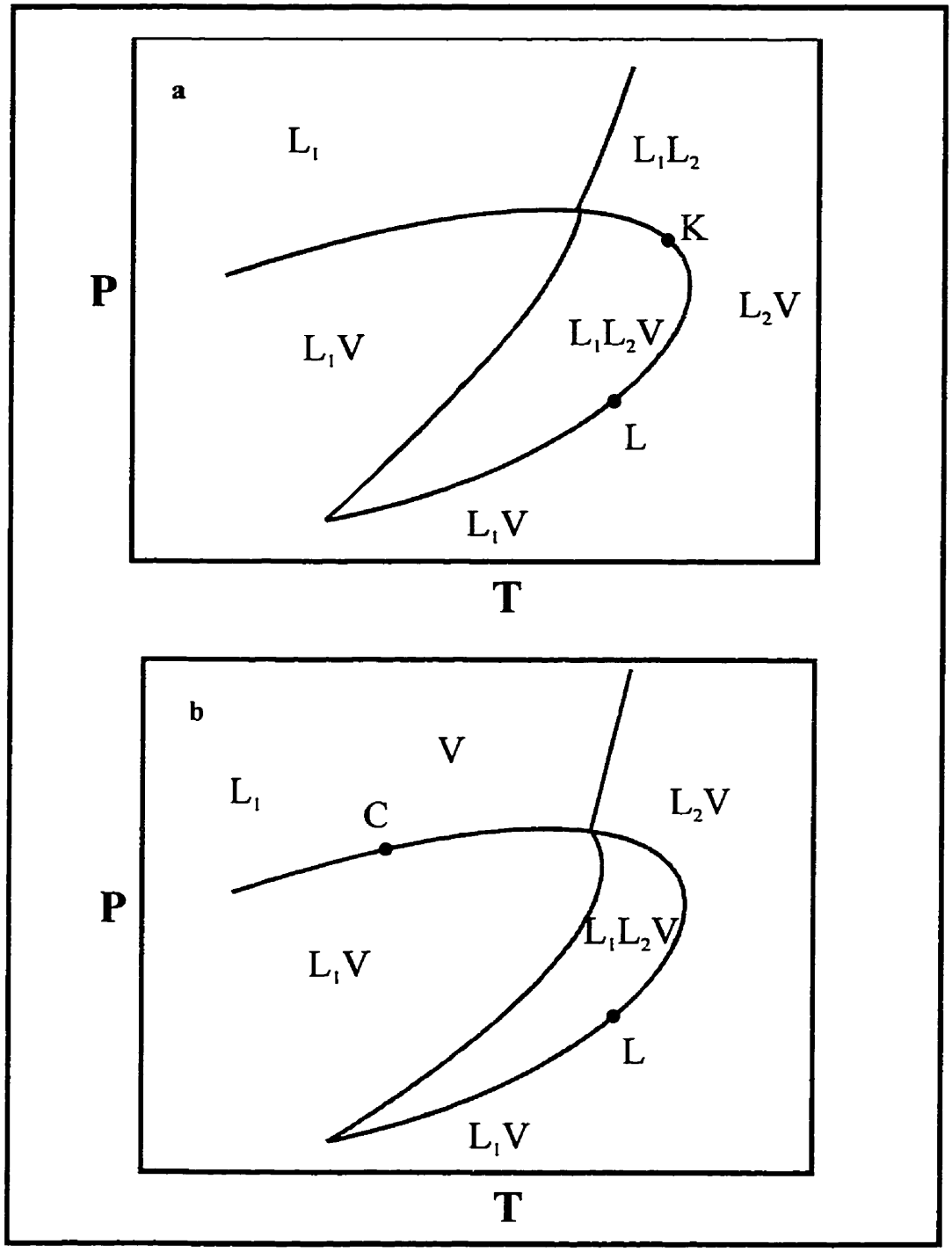

Figure 5.3.2 "a" and "b" sketches of possible complete phase diagrams consistent with the phase boundaries observed in Figure 5.2.2. The dashed box shows the possible location of the experimental observations.

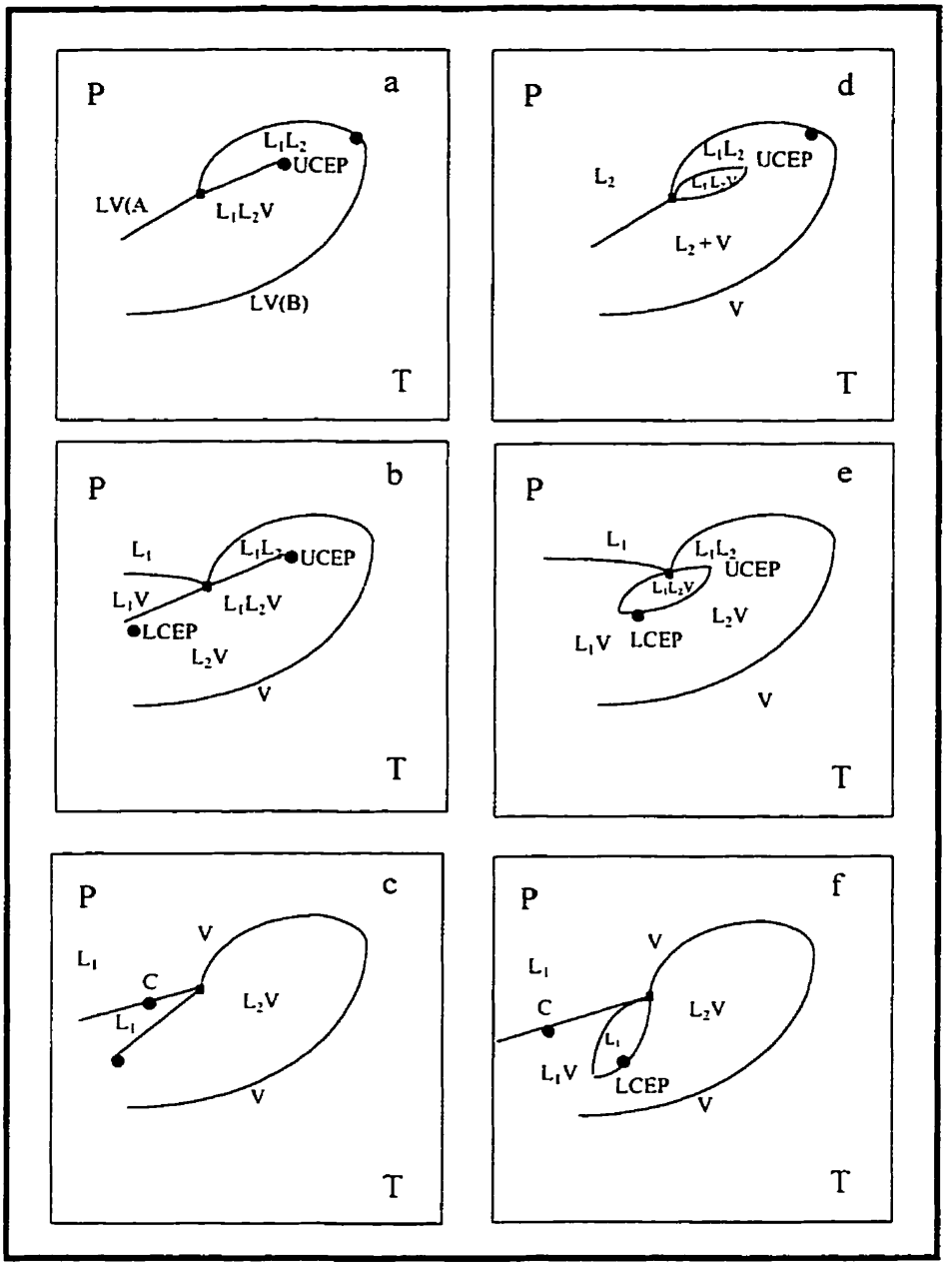

Figure 5.3.3 Expansion of P-T diagrams of Type V phase behaviour from binary mixtures to ternary mixtures .

5.4 The importance of Liquid Density Measurements in Phase Diagram Construction

Liquid density measurements play a critical role in defining phase diagrams such as the one depicted in Figure 5.2.2. Tables 5.2.2 to 5.2.9 display the data used to generate a plot of density versus pressure (Figure 5.4.1). By measuring liquid densities in the two phase regions adjacent to the L_1L_2V region as well as the two liquid densities within the L_1L_2V region, one can confirm visual assessments as to whether a less dense or more dense phase appears as the L_1L_2V region is entered. We can also identify the location of the phase boundary with precision. A sample liquid density diagram, constructed from a series of experiments at about 600 K, is shown in Figure 5.4.1.

For the system ABVB (2 mole %) + dodecane (47 mole %) + hydrogen (51 mole %) both observation and density measurements affirm that the two phase region below the L_1L_2V region is an L_1V region. Liquid density measurements also facilitate the identification of critical phenomena such as L-points. L points are critical points where the L_1 and L_2 phases become identical in the presence of a gas phase. Such singularities are key pivot points in defining mathematical models for complex phase behaviour. Figure 5.4.1 shows that if an L point exists along the lower bond of the LLV region it occurs at a temperature greater than 600 K.

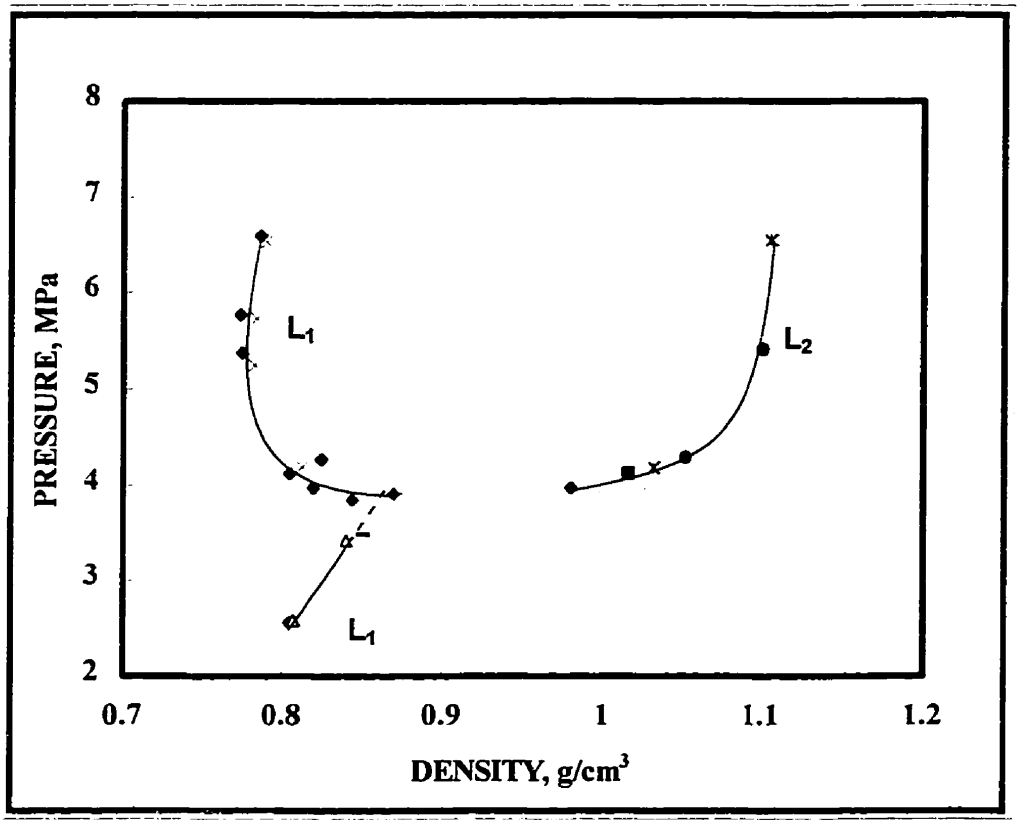

Figure 5.4.1 Example L_1 and L_2 densities as a function of pressure at 600 K +/-5 K for the system ABVB (2 mole %) + *n*- $C_{12}H_{26}$ (47 mole %) + H_2 (51 mole %).

5.5 Phase Behaviour for the System ABVB + Toluene + Hydrogen

A series of experiments was performed with the model heavy oil + aromatic solvent system (ABVB + toluene + hydrogen) at various temperatures between 298 and 700 K and pressures between 1.05 and 7 MPa. . A sample pressure-temperature trajectory is shown in Figure 5.5.1. The primary information obtained from these experiments was whether or not multiple phases were observed at the test pressures and temperatures and the density of liquid and solid phases present. The mass compositions were the same for the ABVB + toluene + hydrogen system. P-T measurements show that the ABVB (2 mole % or 24.8 wt %) + toluene (62 mole % or 74.3 wt %) + hydrogen (36 mole % or 0.9 wt %) system exhibited only LV phase behaviour in the temperature range 425 K to 725 K and the pressure range 1 MPa to 7 MPa, Figure 5.5.2.

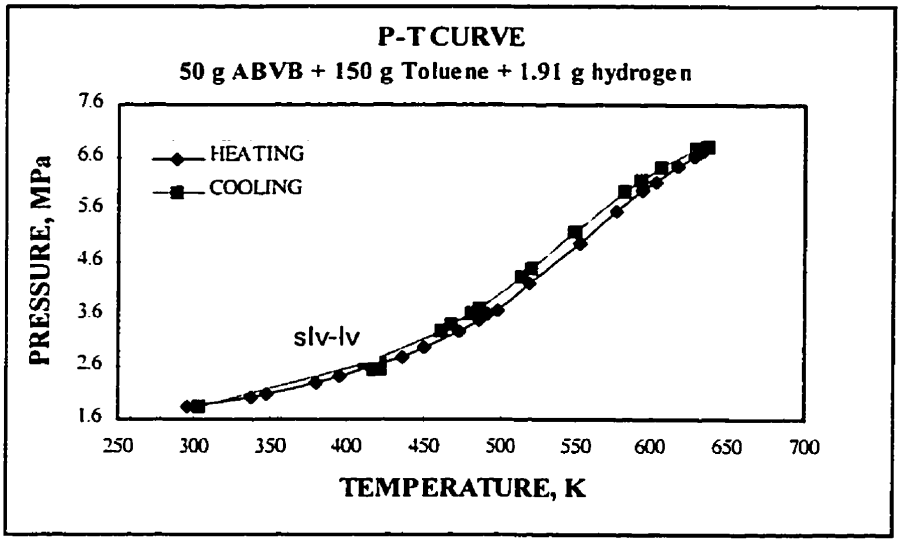

Figure 5.5.1 Pressure-Temperature trajectory (run# 13) for the system ABVB (2 mole %) + C_7H_8 (62 mole %) + H_2 (36 mole %)

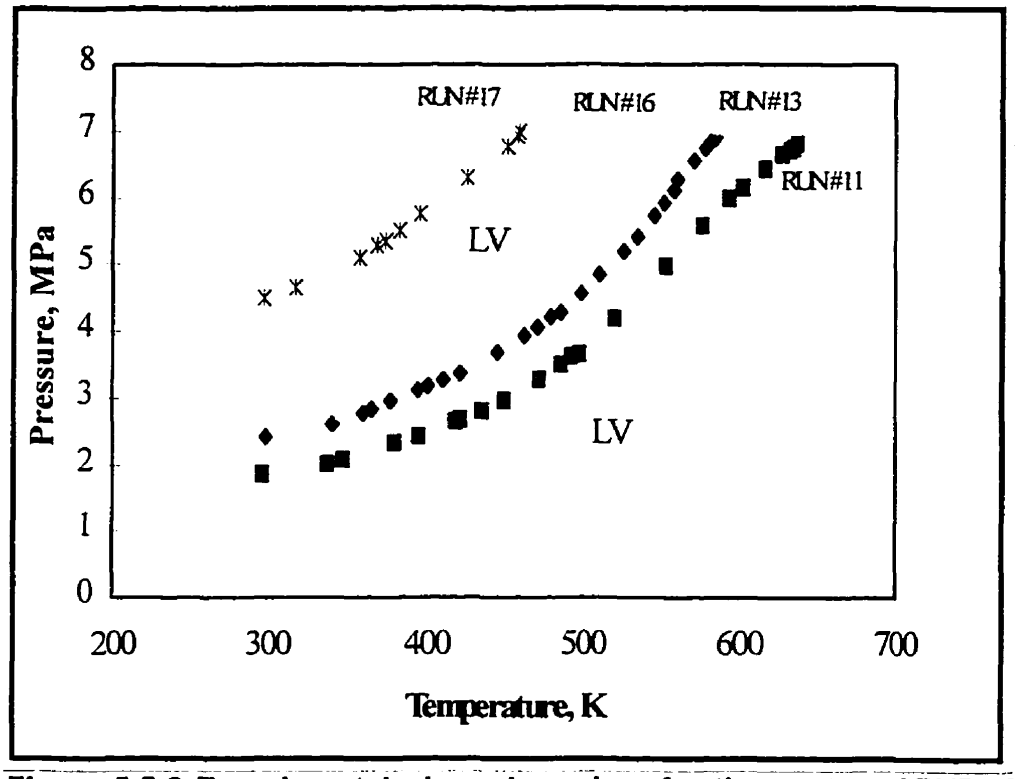

Figure 5.5.2 Experimental phase boundary for the system ABVB (2 mole %) + C_7H_8 (62 mole %) + H_2 (36 mole %).

5.6 *Experiments with the System Anthracene + n-Hexadecane + Hydrogen (Dispersed Solid Phase Detection)*

The phase behaviour of a typical accelerated aging agent for hydrogenation catalysts, anthracene + n-hexadecane + hydrogen, was investigated. The question that arises here is "does this system exhibit complex phase behaviour?". Catalysts (i.e., Ni-Mo or Ni-Al) used in the hydroprocessing of heavy oil refinery fuels often deactivate due to the deposition of coke. Although the mechanism of coke formation is not fully understood, it is commonly thought to arise due to dehydrogenation-condensation reactions involving polynuclear aromatics present in the feed. It has been shown in the previous sections that some common models such as ABVB in combination with an aliphatic solvent and light gas exhibit liquid + liquid + vapour phase

behaviour over wide ranges of temperature, pressure, and composition. This mixture may exhibit liquid + liquid + vapour phase behaviour in either the bulk fluid or within the catalytic pores themselves over the range of temperatures (575-653 K) and pressures (1.1-7 MPa) commonly used in accelerated catalyst aging experiments. If LLV phase behaviour occurs in either the bulk fluid or within the catalyst pores themselves, an anthracene rich liquid phase inside the catalyst has the potential to form coke. This may have an impact on the interpretation of experimental data collected from any such experiments.

A first experiment, based on preliminary calculations using the P-R EOS, was performed with a mixture comprising 10.0 mole % (15.0 wt %) anthracene + 45.0 mole % (84.0 wt %) n-hexadecane + 45.0 mole % (1.0 wt %) hydrogen (Run# 24). The results of this experiment are shown in Table 5.6.1. Phase transitions observed in this case for both heating and cooling are reliable because the mixture is kinetically inactive under the conditions employed. Only solid-liquid-vapour and liquid-vapour phase behaviour was observed in the temperature range 293 K - 652 K and pressure range of 2.14 MPa - 4.66 MPa. Further experiments have been planned with this system.

The only result of note is that the transition from solid-liquid-vapour to liquid-vapour was observed, directly, on heating while the reverse transition from liquid-vapour to solid-liquid-vapour was not observed directly on cooling. Assessment of liquid density and apparent liquid density data obtained off-line by analyzing video stills (Table 5.6.1 and Figure 5.6.1) reveals that there is a large shift in apparent liquid density on cooling, at the location of SLV-LV boundary found on heating. The shift is large - from 0.74 g/cm^3 to 0.91 g/cm^3 at ~ 448 K. Before heating, the anthracene is present as large particles which sit at the base of the liquid and it is possible to obtain a clear image of the liquid phase. The density jump is readily explained in terms of the reappearance of solid anthracene as a microcrystalline solid phase, which is readily observed at room temperature, where it is collected from the view cell. This result is important because we are now in a position to identify the presence of dispersed solid phase from apparent liquid density jumps.

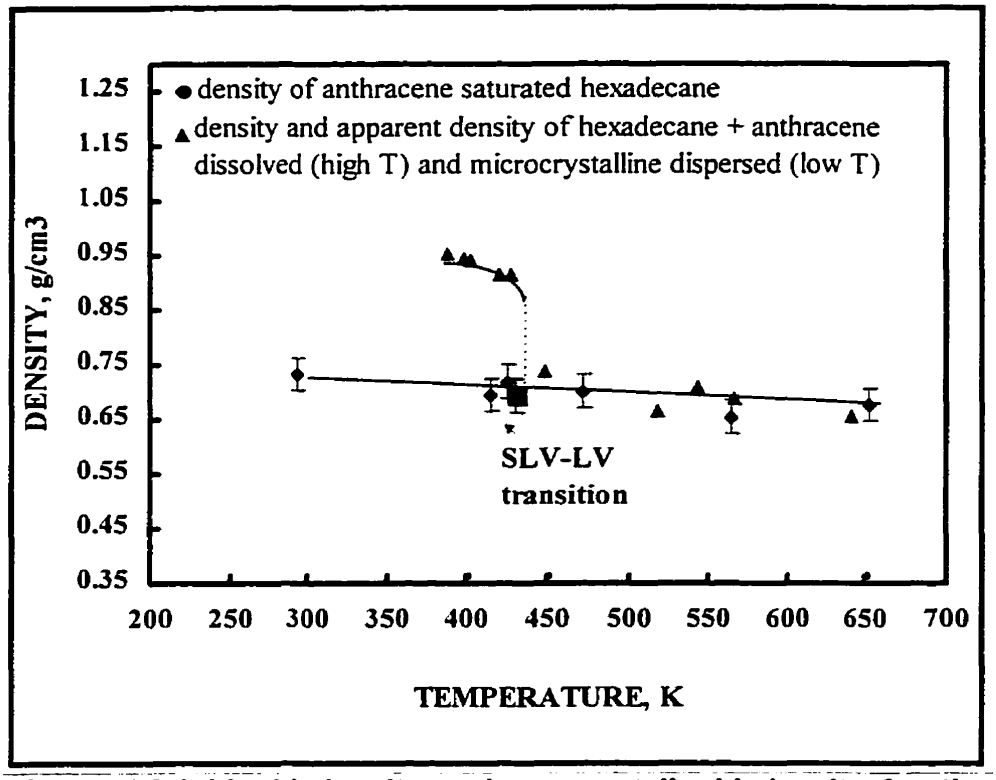

Figure 5.6.1 Liquid density and apparent liquid density for the system 10.0 mole % anthracene + 45.0 mole % *n*- $C_{16}H_{34}$ + 45.0 mole % H_2 . The appearance of a microdispersed solid anthracene phase within the liquid phase is identified by an apparent jump in the "liquid" phase density.

Table 5.6.1 Density of liquid and dispersed phase, 10.0 mole % anthracene + 45.0 mole % n-hexadecane + 45.0 mole % hydrogen (Run# 24). H: Heating, C: Cooling

	Temperature (K)	Pressure (MPa)	Phase	Density of Liquid (g/cm^3)	Apparent Density of the Dispersion (g/cm^3)
H	415	2.83	SLV	.69	
H	425	2.92	SLV	.73	
H	430	2.95	SLV-LV	.69	
H	472	3.23	LV	.70	
H	652	4.66	LV	.68	
H	566	3.94	LV	.69	
C	518	3.58	LV	.64	
C	449	3.06	LV	.74	
C	428	2.91	LV-SLV		.92
C	403	2.76	SLV		.96
C	398	2.72	SLV		.97
C	388	2.64	SLV		.98

5.7 *Identification Of Dispersed Phase Formation From Apparent Liquid Density Measurement (Irreversible Phase Transition (L_1L_2V to DL_1L_2V) for the System ABVB + Dodecane + Hydrogen*

The transmitted x-ray intensity used as the basis for phase density measurements provides an average value across a fluid segment. When a dispersed phase appears, a smaller fraction of the beam is transmitted, the balance is deflected or refracted from the path of the detector, and a higher apparent liquid density measurement results even if the volume fraction of the dispersed phase is small. An example is shown for the system 10.0 mole % anthracene + 45.0 mole % n-hexadecane + 45.0 mole % hydrogen in Figure 5.6.1. The large anthracene crystals present at room temperature were readily observed and separated easily from the liquid phase so that the anthracene saturated hexadecane liquid phase density could

be measured unambiguously. The transition from SLV to LV phase behaviour was also readily observed on heating. On cooling, the LV to SLV transition was not observed directly. The microcrystaline anthracene remained dispersed in the liquid phase at room temperature and it was only from the jump in apparent liquid density values that the transition from LV to SLV phase behaviour was detected.

This feature of the image analysis system was exploited to search for the appearance of dispersed solid phases within L_1 and L_2 for the model heavy oil systems. Such transitions were only found within the L_2 phase and are associated with irreversible solid phase formation. The two examples shown in Figures 5.7.1 and 5.7.2 show L_2 density and apparent L_2 density measurements obtained from two different experimental trajectories. With reference to Figure 5.7.1, there is clearly an apparent liquid density jump in L_2 at 655 K +/- 5 K and 6.3 MPa, which reflects the appearance of a dispersed phase, D, within L_2 as the fluid is heated. This phase does not redissolve on cooling, as indicated by the L_2 density data, and the apparent location of the L_1V-L_1L_2V boundary (now a DL_1V-DL_1L_2V boundary on cooling) is shifted to a lower temperature (by over 70 K). The dispersed phase is not produced reversibly, at least not within the time frame of these experiments, and once formed the phase persists, even at room temperature. There are fewer data available for the second example, Figure 5.7.2, but a similar transition is observed between 640 K and 670 K at ~ 5.2 MPa.

Run #2 exhibited very complex phase behaviour, i.e., phase transitions such as SLV $\rightarrow$ LV $\rightarrow$ LLV $\rightarrow$ SLLV $\rightarrow$ SLV. There was insufficient material to analyze the dispersed phase. However, in a prior study [13,47], a third persistent condensed phase arising under similar conditions was identified and analyzed. The mixture comprised the same components but the mole fraction of ABVB was greater (ABVB (8 mole %) + dodecane (44 mole %) + hydrogen (48 mole %)) and samples were retrieved. This third condensed phase, identified as asphaltenes, contained virtually all of the heavy metals present in the mixture as a whole [13] even though the mass fraction of this phase was small. In this case, we also attribute the apparent density jump to asphaltene precipitation.

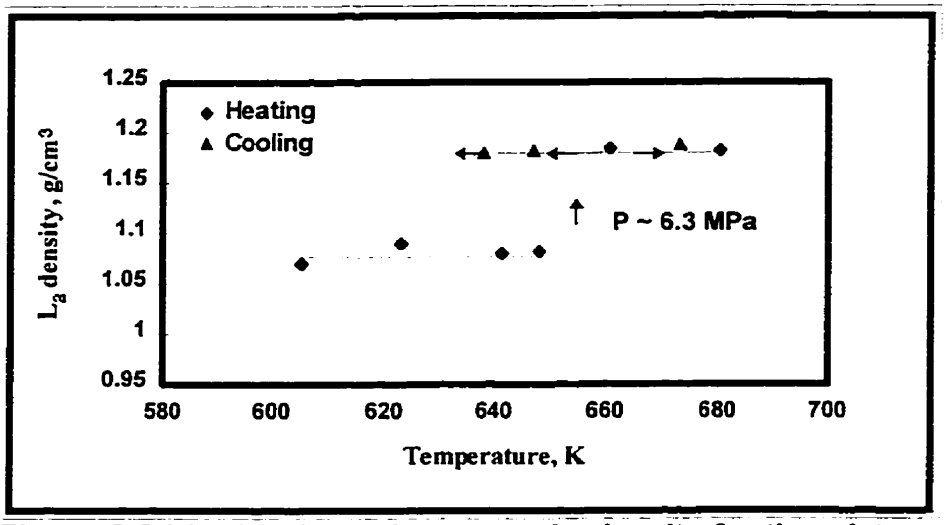

Figure 5.7.1 L_2 density and apparent L_2 density for the mixture of ABVB (2 mole %) + *n*- $C_{12}H_{26}$ (47 mole %) + H_2 (51 mole %), Run# 7.

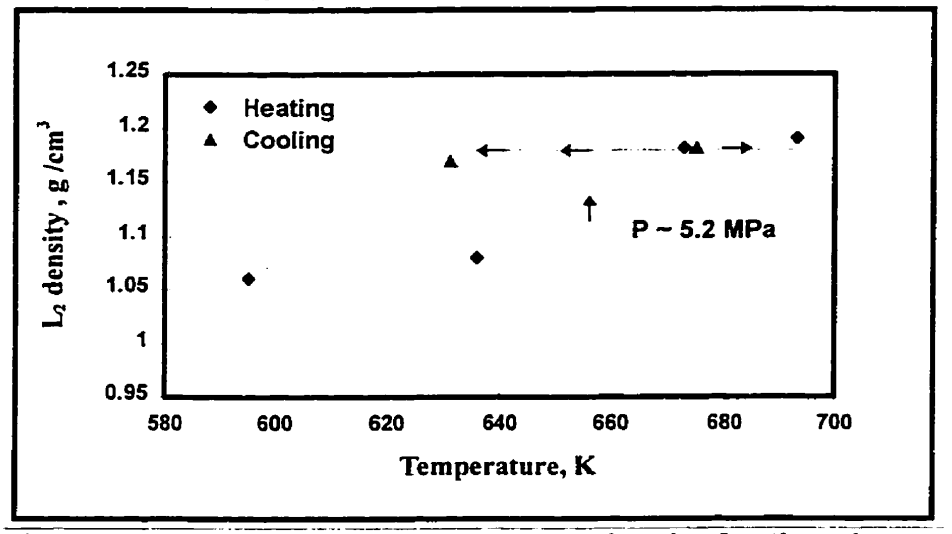

Figure 5.7.2 L_2 density and apparent L_2 density for the mixture of ABVB (2 mole %) + *n*- $C_{12}H_{26}$ (47 mole %) + H_2 (51 mole %), Run# 8.

5.8 A Mechanism For Asphaltene Precipitation

The question arises as to whether this irreversible phase transition results from kinetic or phase behaviour effects. While this researcher agrees that chemical reactions take place at elevated temperatures with these systems, the results cannot be fully explained by conventional reaction kinetics as noted in section 5.9. Reversibility is the most rigorous test for thermodynamic phase transitions. In order to have a phase transition phenomenon during the experiment, one would expect the paths to be reversible. For example: as the temperature for a mixture exhibiting solid at high temperatures is decreased, the solid that appears at a high temperature should redissolve.

According to Mansoori, 1996 [36] solids drop-out from bitumen depends upon the chemical composition of the bitumen. The ratio of polar/non-polar and light/heavy molecules and particles in bitumen (Figure 5.8.1) can also be contributing factors. In this work he refers to solubility, colloidal, and aggregation mechanisms. These are described below.

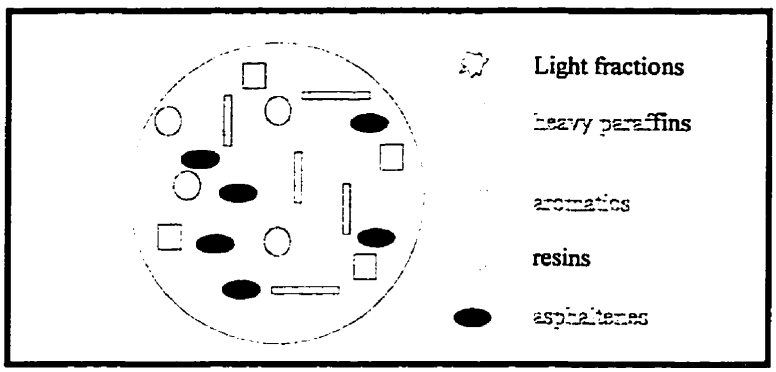

Figure 5.8.1 Microscopic depiction of heavy oil/ bitumen [36]

I. Solubility Effect

Deposition of heavy organics can be explained by an upset in the polydisperse balance of oil composition. Any change in (i) temperature, (ii) pressure , or (iii) composition (such as addition of a miscible solvent to oil as demonstrated by Figure 5.8.1) may

destabilize the polydisperse oil. Then the heavy and/or polar fractions may separate from the oil mixture into micelles, another liquid phase or into a solid precipitate.

II. Colloidal Effect

Some of the heavy organics (specially asphaltenes) separate from an oil phase into an aggregate (large particles) and which then will remain suspended in oil by some peptizing agents, like resins, which are adsorbed on their surface and keep them afloat as demonstrated by Figure 5.8.2.

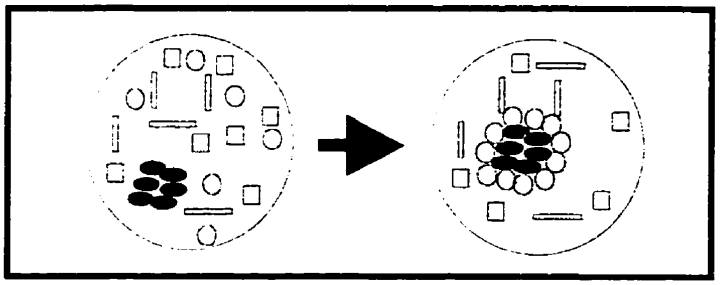

Figure 5.8.2 Peptization of asphaltenes precipitates by resin to form steric colloids

Stability of such steric colloids is considered to be a function of concentration of the peptizing agent in the solution, the fraction of heavy organic particle surface sites occupied by the peptizing agent, and the equilibrium conditions between the peptizing agent in solution and on surface of heavy organic particles. The amount of peptizing agent adsorbed is primarily a function of its concentration in the oil. A concentration variation of a peptizing agent (such as resins) can cause its adsorbed amount on the surface of heavy organic particles to change.

III. Aggregation Effect

The peptizing agent concentration in oil may drop to a point at which its adsorbed amount is not high enough to cover the entire surface of heavy organic particles. This permits

aggregation of heavy organic particles due to development of free active sites on their surfaces, and their eventual flocculation as shown by Figure 5.8.3. This may then permit the heavy organic particles to come together (irreversible aggregation), grow in size, and flocculate. The nature and shape of the resulting aggregates determines their effect on the behaviour of the petroleum fluids.

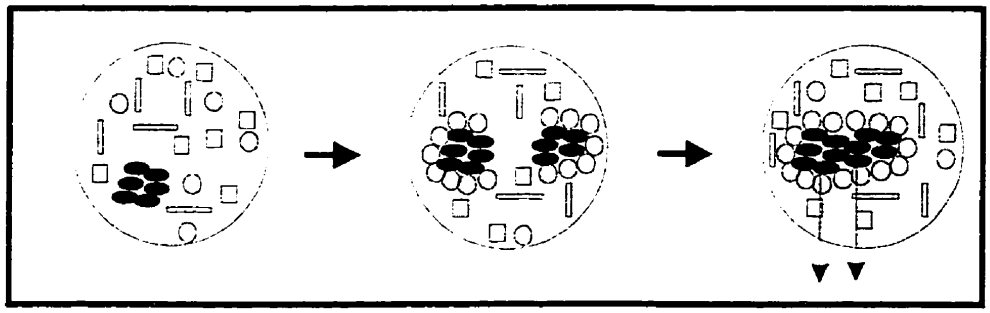

Figure 5.8.3 Aggregation and growth of heavy organic colloids and their eventual deposition

Various aggregating macromolecules follow different aggregation patterns. For example, the irreversible aggregates of asphaltene are considered to follow an aggregation growth pattern shown in Figure 5.8.4 [36].

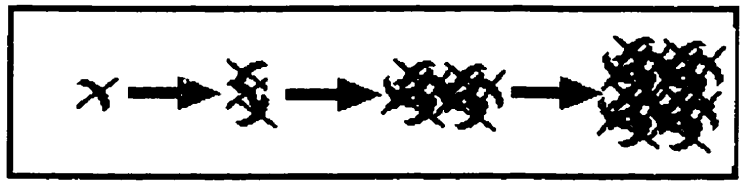

Figure 5.8.4 Irreversible aggregates of asphaltene [36].

In the present work, for the runs where phase transitions from liquid-vapour to liquid-liquid-vapour were observed, reversibility arose uniformly. Once the phase transition from liquid-vapour to liquid-liquid-vapour was observed, the reverse phase transition could be obtained by turning off the heater and allowing the temperature and pressure to decrease. At

655K and 6.3 MPa such mixtures are typically considered to be kinetically active. However, if we heat a mixture with the same composition but operate at a lower pressure so that the trajectory remains within the L_1V region, no evidence of dispersed phase formation arises even at 706 K and 3.8 MPa (Figure 5.8.5), because the density profile is reversible.

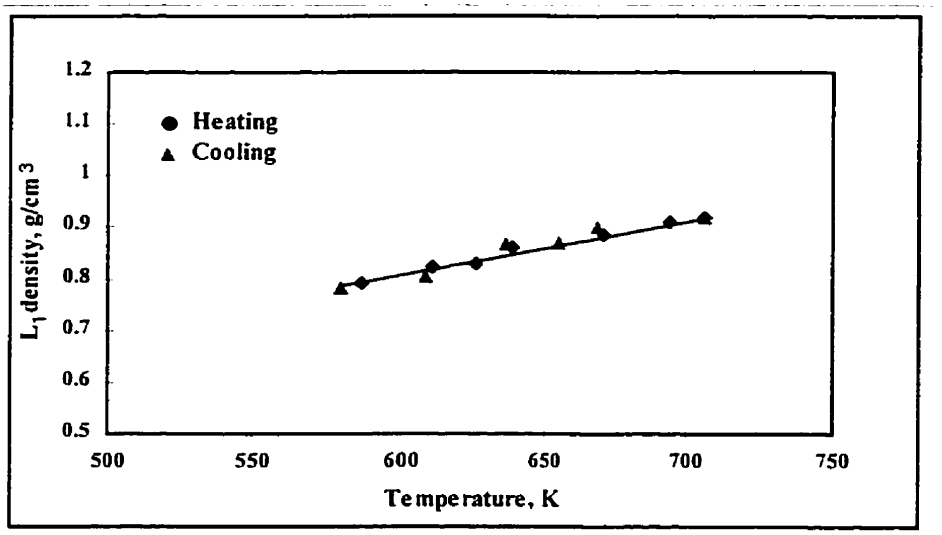

Figure 5.8.5 L_1 density for an experimental trajectory remaining below the L_1L_2V phase boundary. The mixture composition is ABVB (2 mole %) + *n*- $C_{12}H_{26}$ (47 mole %) + H_2 (51 mole %).

This result suggests that the origin of the transition is related to phase behaviour and not reaction kinetics as the mixture is more active kinetically at over 700 K than at 655 K in an otherwise similar reaction environment. None of the current reaction models for heavy oil processing can account for such an effect. Thus a mechanism for bulk asphaltene precipitation in heavy oil systems clearly supported by these findings is that precipitation arises as a consequence of an irreversible phase transition occurring in the L_2 phase (Figure 5.8.6). Asphaltene precipitation did not arise in the absence of the L_2 phase, i.e., within the L_1V region, even at temperatures in excess of 700 K. Thus these data provide a strong link between asphaltene precipitation and multiphase behaviour, and indicate that asphaltene precipitation can arise purely from physical phenomena. With reference to the general phase

diagram, Figure 5.3.2, pressure-temperature regions most susceptible to this mechanism for asphaltene precipitation include parts of what would otherwise be the L_2V, L_1L_2 and L_1L_2V regions. The link with Mansoori's work is unclear at this juncture. Evidently, the irreversible appearance of solid corresponds must closely to the flocculation mechanism, in a general sense, but the details are rather different.

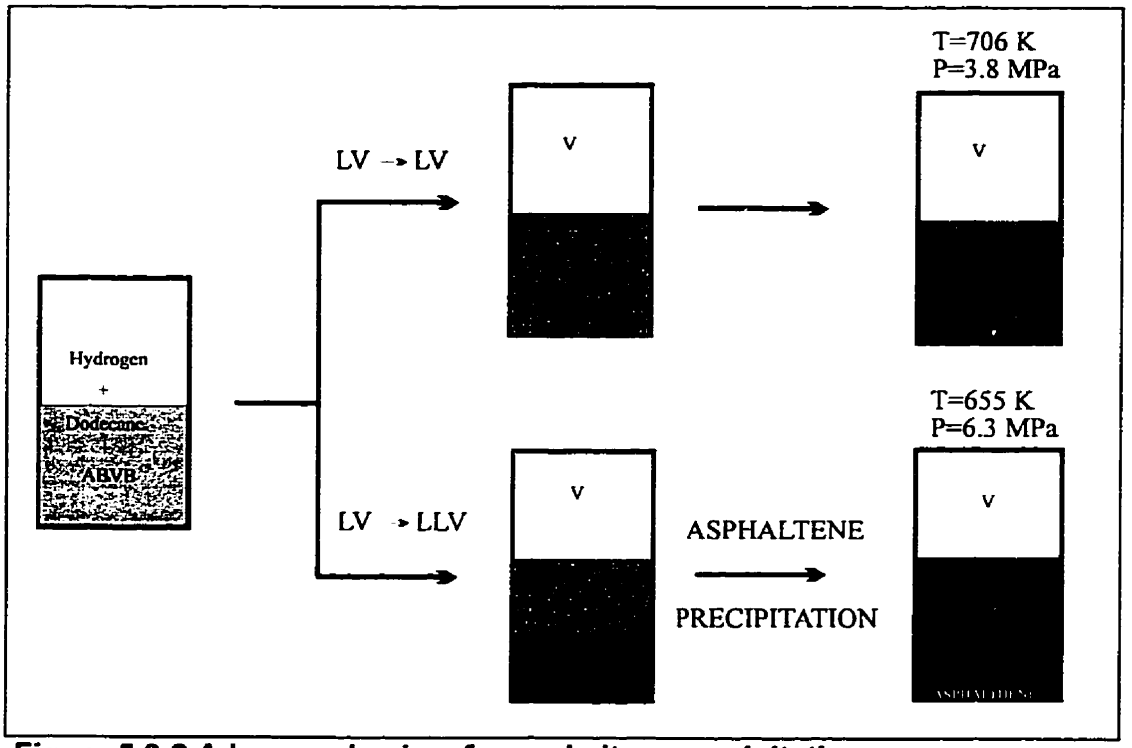

Figure 5.8.6 A key mechanism for asphaltene precipitation

5.9 Kinetics Versus Irreversible Phase Behaviour to Explain Solids Dropout from L_2 and not L_1

Kinetic arguments have been advanced to explain solids dropout from L_2 when it does not occur in L_1 even at higher temperatures. In this section this issue is explored. A kinetic argument can be advanced by expressing the rate of the polymerization/ condensation reaction as a simple n^{th} order irreversible reaction and by employing an Arhennius expression for temperature correction of coefficients.

Consider:

- Case I: where the heavier second liquid phase, L_2 , is not present, T_1
- Case II: where the heavier second liquid phase is present, T_2

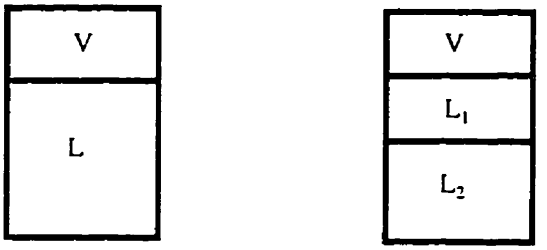

Case I Case II

In Case II, the concentration of ABVB in phase L_2 is higher than in phase L_1 . Let us denote the rate of asphaltene formation and concentration of ABVB in Cases I and II as r_1 and r_2 and C_1 and C_2, respectively. Thus

$$r_2 / r_1 \propto \exp[-E_{act} /R[1/T_2 - 1/T_1]] ([C_2] / [C_1])^n \qquad (5.9.1)$$

Where E_{act} is the energy of activation. From our experiments we know $T_1 = 705$ K, $T_2 = 655$ K, $C_1 = 0.25$, and $1 \geq C_2$. Reported values for E_{act} are in the range of 5×10^4 cal/mol, [53] (values as low as 10^4 cal/mol have been reported [54]) and R= 1.99 cal/mol. K. Typically n is set at 0 or 1 in kinetic models for such cases thus, the rate of reaction in case II at 655 K can

only be up to three times the rate for case I at 706 K. In case II, the solid was formed soon after the temperature passed 655 K (within a minute or two). In case I the cell was at 706 K for at least 30 minutes and was at temperatures greater than 655 K for two hours with no evidence of solids dropout. Without choosing extreme values for E and n one does not arrive at a condition where $r_2 >> r_1$.

5.10 The Development of Physical Models for the Phase Behaviour of Heavy Oil or Bitumen + Hydrogen Systems

Based on the experimental data and the existing phase behaviour theories, we have adopted a general approach for defining the bounds of multiphase regions for all such fluid systems. Our approach is predicated on the evaluation of special critical points called K and L points - both experimentally and computationally. K points are points in pressure-temperature space where a light liquid and a vapour become identical and merge in the presence of a second more dense liquid phase. L points are similar except that the less dense liquid, L_1, and the more dense liquid, L_2, become identical and merge in the presence of a vapour phase. Such points are difficult to identify both computationally and experimentally.

For example, we have shown experimentally that ABVB + hydrogen, and ABVB + dodecane + hydrogen exhibit L_1L_2V phase behaviour. As hydrogen and dodecane are not fully miscible with ABVB these data imply that ABVB exhibits L_1L_2V phase behaviour and K and L points on its own. By assessing K and L points for a few ABVB + diluent + hydrogen mixtures, where the composition and mole ratio of hydrogen to diluent are fixed but the mole fraction of ABVB is varied, L and K loci can be constructed. These loci place lower and upper bounds on L_1L_2V phase behaviour regardless of the mole fraction of ABVB in the mixture. This point is illustrated in Figure 5.10.1.

While L_1L_2V phase behaviour does not extend to the apex of the triangular region, it certainly does not exist outside of it. The K and L points of ABVB arise at temperatures and pressures where on its own the fluid is active kinetically. It is not possible to assess them directly with any certainty. However, by changing the mole ratio of hydrogen to diluent a second set of L and K loci can be generated. These loci intersect the previous pair of loci at the K and L point of the ABVB as illustrated in Figure 5.10.2. Having identified the K and L points of ABVB in this manner, we only need to perform a single phase equilibrium experiment (to obtain interaction parameters, if not available elsewhere) in order to define the L_1L_2V space for each new diluent considered, again regardless of composition, because the theory and mathematical models can then impose well-defined limits on phase behaviour.

The identification of L and K points for ABVB would represent a major step forward in our understanding and thus our modelling capabilities for such systems. We only now possess a view cell capable of identifying K and L points experimentally, see Chapter 4. Formerly, we were unable to identify K points experimentally because the K points arose at pressures greater than the maximum allowable working pressure of the apparatus.

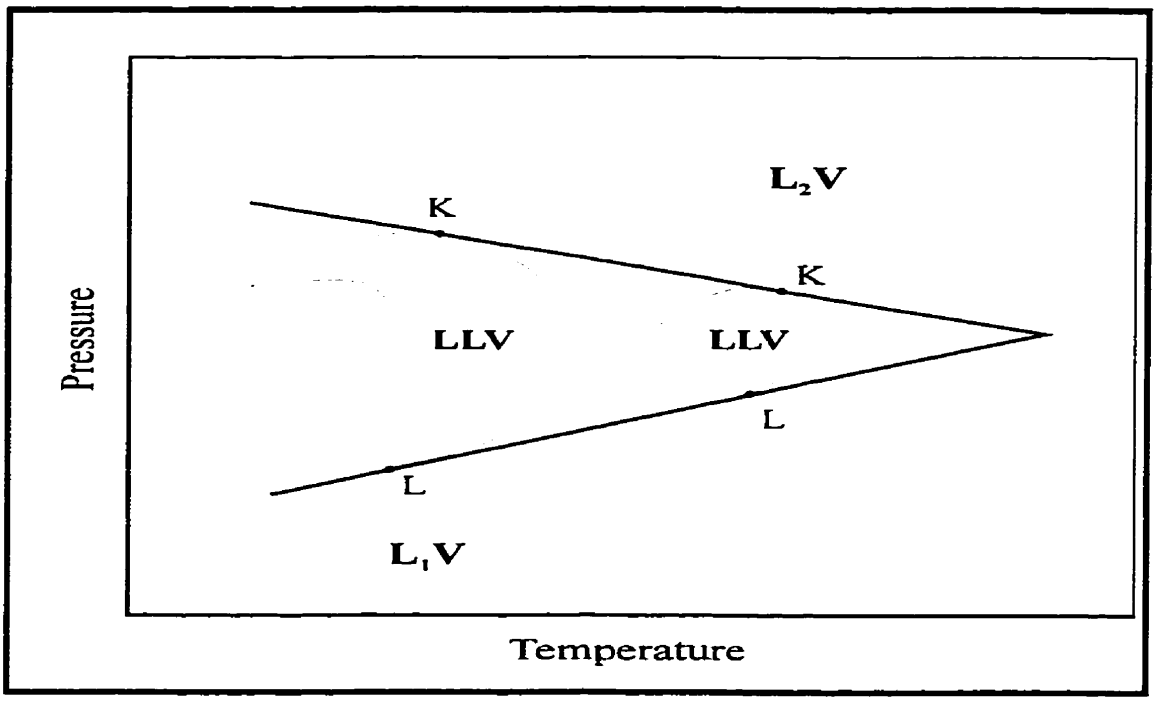

Figure 5.10.1 The K and L loci define the upper and lower bounds of the region where LLV phase behaviour is possible regardless of the amount of diluent and hydrogen mixture of fixed composition added.

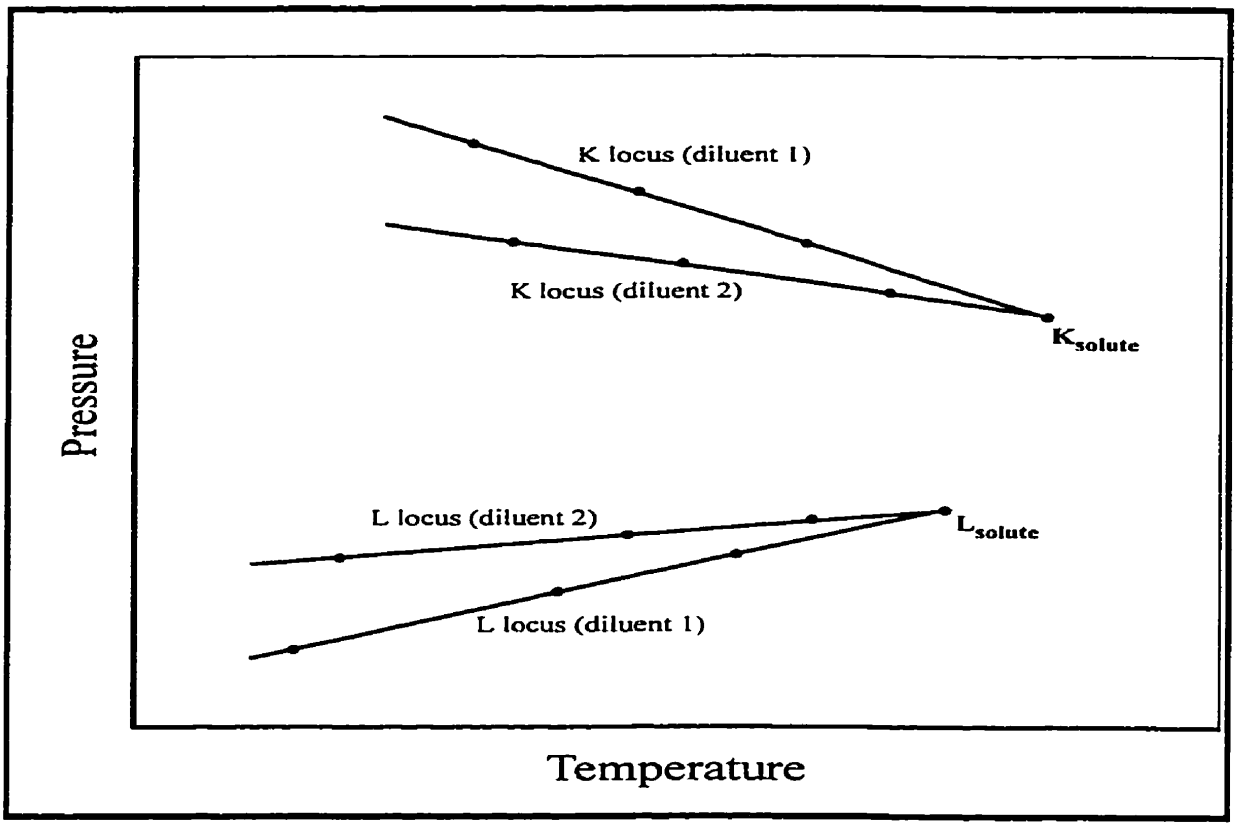

Figure 5.10.2 K and L loci for different diluent and solute compositions converge at the K and L points of the solute.

Figure 5.10.3 shows the L_1 and L_2 densities for the system ABVB (2 mole %) + dodecane (47 mole %) + hydrogen (51 mole %). It also shows the apparent L_2 densities for the system. Density measurement allowed us to show that the density of the liquid phase increases progressively from 0.77 to 0.9 g/cm^3 for the light liquid phase, L_1 , and from 1.0 to 1.18 g/cm^3 for the apparent density of the heavy liquid phase, L_2, as temperature rises. L_2 densities divide into three regions: at temperatures less than 540 K it is ~ 1 g/cm^3 , at temperatures between 590 to 640 K it is ~ 1.07 g/cm^3, and at temperature greater than 650 K it is ~ 1.18 g/cm^3. Tables 5.2.7 and 5.2.8 clearly show that the densities are increasing on heating and decreasing on cooling in the temperature range 540 to 640 K. While we cannot observe irreversible transitions directly, these appear to arise whenever the apparent density of L_2 exceeds ~1.15 g/cm^3. Once the apparent density of L_2 becomes this high, the solids produced do not redissolve on cooling.

One of the phenomena sought in the phase equilibrium experiments was L-points. We expected L_1 and L_2 densities to merge at high temperatures. They appear to diverge which is inconsistent with the theory presented above. What can account for this? One expects that the L_2 density would decrease as temperature increases and that the L_1 density would increase. We can attribute the jump in L_2 density at 540 K to reversible micelles formation along the lines of Mansoori [36] or Section 5.9 as long as we can demonstrate that micelles deflect x-rays in the same way as solids. This however is subject to experimental verification which is beyond the scope of this thesis. Small angle x-ray scattering is a technique used to determine micelles size [55]. If it proves to be the case then the L-point temperature for the mixture can be estimated by holding the L_2 density fixed at its low temperature value (~ 1 g/cm^3) and extrapolating the L_1 density to this value. One then obtains an over estimate for the L-point temperature of ~750 K. If micelles cannot be detected with x-rays then the experimental L_2 density results remain in conflict with phase behaviour theory.

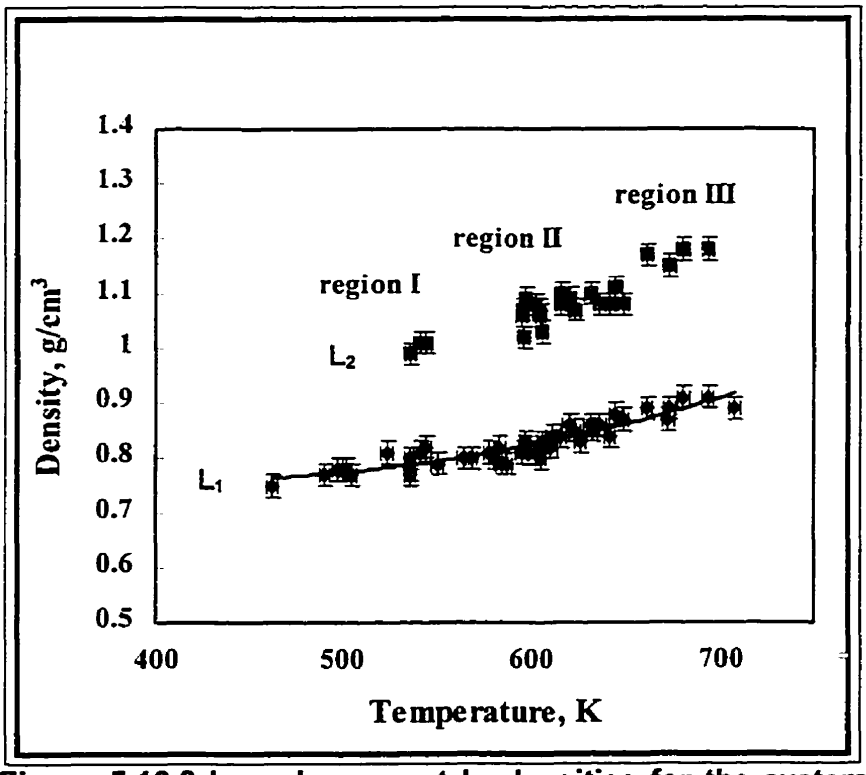

Figure 5.10.3 L_1 and apparent L_2 densities for the system ABVB (2 mole %) + dodecane (47 mole %) + hydrogen (51 mole %)

5.11 Complex Phase Behaviour and Heavy Oil Upgrading Processes

The phase diagrams, Figures 5.2.1 and 5.2.2, provide the first evidence of the reversible and irreversible nature of the complex phase behaviour that arises with heavy oil/bitumen mixtures under upgrading process conditions. The pressure - temperature phase diagram for ABVB (2 mole %) + n-dodecane (47 mole %) + hydrogen (51 mole %) is superimposed on the operating conditions for heavy oil / bitumen upgrading processes in Figure 5.11.1. The reader should note this diagram is intended for qualitative and comparative purposes only. The graph shows reversible and irreversible effects and demonstrates that observed complex phase behaviour falls within the pressures and temperatures of current industrial technologies and that solids dropout is an issue over much of the range. In several heavy oil upgrading schemes high and low pressure separators are used to fractionate product streams of which a portion is often recycled. Clearly if low pressure separators are operating in the region where three- or four-phase behaviour arises then vessels and transfer line plugging can be expanded and product (or recycle) streams would not behave as expected in subsequent process steps. In fixed bed processes a recycle stream which contained a "solid" phase or heavy liquid phase would be subject to an accumulation of the heavy material.

Small changes in operating conditions can lead to radically different yields and product distributions. There are many such processing problems in industry and Syncrude and Amoco (who share common LC-fining processing technology) have conferred with this laboratory to address such issues. We expect that these finding will have a significant impact on the design and operation of heavy oil/bitumen upgrading technologies as solids dropout in particular appears to arise within the L_2 phase only and may not be subject to kinetics per se. Furthermore, reaction kinetic and hydrodynamic models must now consider the existence of not just the typical two phases, liquid and vapour, but must incorporate the possible appearance of three and four organic phases and the attendent interfacial mass transfer resistances. There is much room here for further investigation.

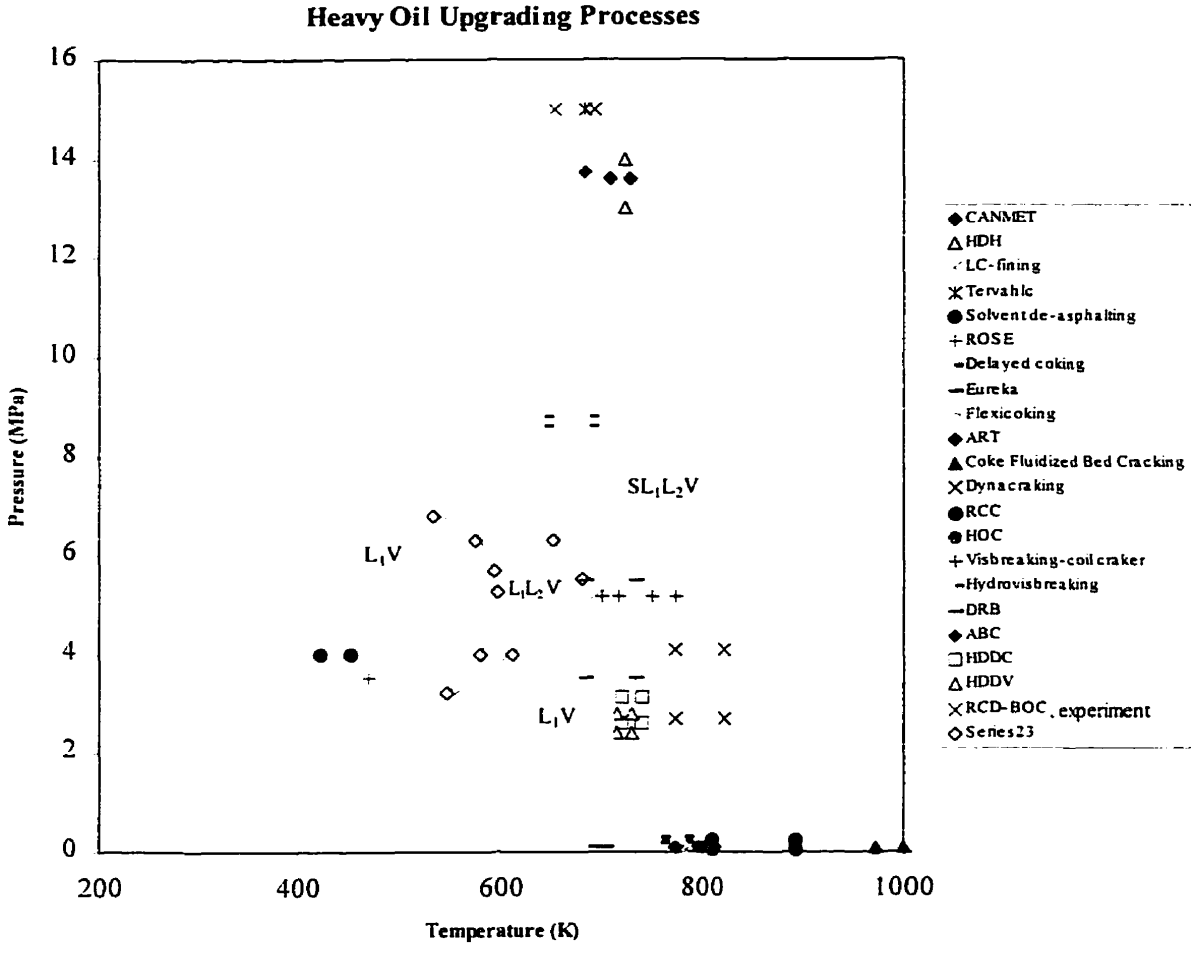

Figure 5.11.1 Heavy oil upgrading process operating conditions with a phase diagram for the mixture ABVB (2 mole % or 24.6 wt %) + *n*- $C_{12}H_{26}$ (47 mole % or 73.8 wt %) + H_2 (51 mole % or 1.6 wt %) superimposed show reversible and irreversible effects. Process operating conditions observed from Dukhedin-Lalla [47].

Chapter 6

CONCLUSIONS

1. Our results clearly demonstrate that ABVB + diluent + hydrogen exhibit complex reversible and irreversible phase behaviour at elevated temperatures. We expect that this finding will have a significant impact on the design and operation of heavy oil/ bitumen upgrading technologies because the possible impact of solid dropout and other multiphase behaviour on kinetics, hydrodynamics, separation processes, preheaters, etc. must now be considered.

2. ABVB + n-dodecane + hydrogen mixtures have been shown to exhibit reversible liquid-liquid-vapour and apparently irreversible solid-liquid-liquid-vapour equilibria under conditions associated with a number of upgrading and related processes. This phase behaviour is consistent with experimental phase behaviour of reservoir fluids as well. This similarity in phase behaviour suggests that the appearance of solid and liquid phases present in bitumen mixtures can be modelled in a similar manner.

3. An accurate though partial phase diagram for the system athabasca bitumen vacuum bottoms (ABVB) (24.6 wt. % / 2 mole %) + dodecane (73.8 wt. % / 47 mole %) +

hydrogen (1.6 wt % /51 mole %) was constructed in the temperature range 425 K to 725 K and the pressure range 2 MPa to 7 MPa. This fluid system is shown to exhibit two phase L_1V and three phase L_1L_2V phase behaviour over parts of this P-T region.

4. Transitions between the multiphase regions were found to be reversible at temperatures less than 655 K.

5. At temperatures greater than 655 K irreversible solids dropout arose within the L_2 phase. It did not arise in the absence of the L_2 phase, i.e., within the L_1V region, even at temperatures in excess of 700 K. These results clearly show an association between solid dropout and the L_2 phase.

6. These data provide a strong link between solids dropout and multiphase behaviour. A physical rather than kinetic basis for solids dropout at elevated temperature is suggested. The physical versus thermo-kinetic nature of the precipitation remains a subject of debate and detailed analysis of the "asphaltenes" is warranted.

7. The shape of the low temperature boundary between the L_1V and L_1L_2V zones is characteristic of dilute asymmetric mixtures where a heavy liquid phase, L_2, appears then disappears within the light liquid phase, L_1, on isothermal compression. Such phase behaviour is referred to as unusual retrograde condensation and is of both practical and theoretical interest. From volumetric and density measurements as well as the shape of the low temperature boundary of the liquid-liquid-vapour zone, a small mass fraction of ABVB appears to be the source of the complex phase behaviour in the system ABVB + n-dodecane + hydrogen.

8. The system ABVB + n-dodecane + hydrogen was found to exhibit retrograde condensation of the heavier liquid phase, over a broad range of pressures, and temperatures. This is only the second such large scale occurrence reported.

9. The modified analysis technique and new equipment accurately compensate for the problems that were encountered during previous attempts to make an accurate liquid density calibration curve. The x-ray imaging system has been utilized to determine densities of condensed phases of opaque hydrocarbon fluids at elevated temperatures and pressures with a precision of +/-0.02 g/cm^3. Such a precision is accurate enough for density shift connections in equations of state.

10. A variable volume view cell suitable for studying the phase behaviour of opaque hydrocarbon systems was developed. This device, created in collaboration with D. B. Robinson Ltd., will greatly simplify our experimental program and allow us to operate with much smaller samples of fluid over a broader range of conditions and more efficiently than was possible previously.

Chapter 7

RECOMMENDATIONS

Experiments

The main objective of this project was to examine the phase behaviour of heavy oil systematically in the presence of light gases as a step toward modeling the phase behaviour of such mixtures. Construction of an accurate phase diagram for a model heavy oil system, identification of retrograde phenomena, and irreversible phase behaviour are an important part of this work.

- Critical phenomena such as L-points and K-points should be identified.
- K and L points for the mixture of n-dodecane + hydrogen + varying amounts of ABVB should be identified so that the K and L points of ABVB on its own can be identified and fed to the mathematical modelling activities.
- Similar experiments are envisioned with other heavy oils to obtain K and L points (Guado, etc.).
- More experiments should be run in order to complete a phase diagram for the system anthracene + hexadecane + hydrogen.
- In order to determine whether or not micelles deflect x-rays, experiments with model systems should be performed.

Mathematical Models

Models that are able to predict or correlate parameters for the modeling of complex multicomponent systems are valuable because they can easily and quite readily predict the phase behaviour of a complex system on a broad range of compositions, temperatures, and pressures without the need for time-consuming and expensive phase equilibria experiments. Preliminary qualitative models have already been found by Cartlidge et al.[13]; however, the phase boundaries are displaced in P-T space by 40 K and 4 MPa. The data used for the above model were themselves preliminary and too imprecise to achieve reasonable modelling parameters. Data from this work which has been published by Abedi et al. [18] for athabasca bitumen vacuum bottoms (2 mole %) + dodecane (47 mole %) + hydrogen (51 mole %) is available and reproducible to 3 K and 0.03 MPa. These data are more accurate than the data used for the above model and thus offer the prospect of finding suitable parameters by regression i.e., this thesis lays the foundation for modelling.

One approach is to model the phase behaviour of ABVB (2 mole %) + dodecane (47 mole %) + hydrogen (51 mole %) using the Peng-Robinson equation of state and the tangent plane criterion. The ABVB can be modeled as two or three pseudo-components. Before any phase modelling calculations can be carried out, it is necessary to specify modelling parameters for the equation of state. If these values are not known they need to be estimated, and the accuracy of the model is greatly influenced by the accuracy of such parameters. The number of parameters required depends on the number of components and pseudo-components in the system. These parameters include:

- critical temperature for each component,
- critical pressure for each component,
- acentric factor for each component,
- interaction parameters between each pair of components.

Thus, for the four component system above, eighteen parameters are required: four critical temperatures, four critical pressures, four acentric factors, and six interaction parameters. There are well-established methods for estimating the properties of petroleum cuts. In spite of different structural and chemical properties of bitumen and oil, similar methods can

be used for bitumen [56], although parameter estimates vary appreciably with the method chosen [57].

So far accurate models have proven elusive and this quest has been spun off as two separate projects:

- **Clive Cartllidge Ph.D.** : On the prediction of solid phases and K and L points
- **Dan Minicucci M.A.Sc.**: Preliminary assessment of parameters and pseudo components for modelling ABVB + dodecane phase behaviour.

Equipment

The absorption of polychromatic x-rays can be used in the petroleum industry for determination of elemental compositions (C, H, S, N, heavy metals). This is an ideal application because the hydrocarbon matrices have very low absorption coefficients and because these coefficients do not change appreciably with changes in the hydrocarbon makeup of the matrix as absorption by hydrogen and by carbon is nearly at the same wavelengths [49]. Elemental composition determination is among the current duties of **H. Cai**, a post doctoral fellow.

Applications

Wholly new areas of study arise because reaction kinetic and hydrodynamic models, and separation schemes for heavy oil/bitumen must now consider possible appearance of three and four organic phases and the attendant interfacial mass transfer resistances.

REFERENCES

[1] Francis A.W., Ternery Systems of Liquid Carbon Dioxide, J. Phys. Chem., 58: 1099-1114, 1954.

[2] Francis A.W., Solvent Extraction with Liquid Carbon Dioxide, Ind. Eng. Chem., 47: 230-233, 1955.

[3] Chung K.H., Xu C., Hu Y., and Wang R., Supercritical fluid extraction reveals resid properties, Oil & Gas Journal, 1997.

[4] Oelderik J.M., Sie S.T., and Bode D., Progress in the Catalysis of the Upgrading of Petroleum Residue, Appl. Catalysis, Vol. 47, P. 1, 1989.

[5] Unger H., Sze M.C. and Driesen R.P., Hydrogenation of High Boiling Hydrocarbons. US Patents 4411768, Oct. 25, 1983.

[6] Van Driesen R.P., and Fornoff L.L., Upgrade Resids with LC-Fining, Hydrocarbon Proc., p. 91-95, Sept. 1985.

[7] Shelton J. L., and Yarborough L.: SPE-AIME Conf. Tulsa Okla, March 22-24, paper SPE 5827, 1976.

[8] Turek E. A., Metcalfe R. E., and Fishback, R. E., Phase Behaviour of Several CO_2 /West Texas Reservoir Oil Systems, SPERE, 505-516, 1988.

[9] Shaw J.M., de Loos Th., and de Swaan Arons J., Prediction of Unusual Retrograde Condensation in Model Reservoir Fluids, Fluid Phase Equilibria, 84: 251-266, 1993.

[10] Shaw J.M., de Loos Th., and de Swaan Arons j., An Explanation for Solid-liquid-liquid-vapour Phase Behaviour in Reservoir Fluids. In press Petroleum Science and Technology, 1997.

[11] Dukhedin-Lalla L., Yushun S., Rahimi P., and Shaw J. M., Phase Splitting of Complex Hydrocarbon Mixtures, Fluid Phase Equilibria, 53: 415-422, 1989.

[12] Dukhedin-Lalla L., A Study of Complex Phase Behaviour Arising In Heavy Oil / BitumenMixtures Using X-ray Imaging Ph.D. Thesis, U. of Toronto, 1996.

[13] Cartlidge C.R., Dukhedin-Lalla, L, Rahimi, P., and Shaw, J. M, Preliminary Phase Diagrams for ABVB + n-Dodecane + Hydrogen, Fluid Phase Equilibria, 117: 257-264, 1996.

[14] Wiehe I.A., A Phase-separation Kinetic Model for Coke Formation. Ind. Eng. Chem. Res., 32: 2447-2454, 1993.

[15] Wiehe I.A., Coking Kinetics and Limits. Conrad Workshop on Bitumen Upgrading Chemistry, Calgary, Alberta, June 7-8, 1995.

[16] Storm D. A., Barresi R. J., and DeCanio S. J., Colloidal Nature of Vacuum Residue. Fuel, 70: 779-787, 1991.

[17] Storm D. A., Microscopic Phase Separation of Asphaltenes in Temperature Range of 150-400^0 C, Conrad Workshop on Bitumen Upgrading Chemistry, Calgary, Alberta. June 7-8, 1995.

[18] Abedi S.J., Seyfaie S., and Shaw J.M., Unusual Retrograde Condensation and Asphaltene Precipitation in a Model Heavy Oil System, Petroleum Science & Technology, January 1998

[19] Van Konynenburg P.H., and Scott R.L., Critical Lines and Phase Equilibria in Binary van der Waals Mixtures. Phil. Trans. Roy. Soc., 298: 495-540, 1980.

[20] Griffiths, R.B. and Wheeler J.C., Critical Points in Multicomponent Systems. Phys. Rev. A, 2 (3) : 1047-1064., 1970.

[21] Widom B., Tricritical Points in Three and Four Component Fluid Mixtures, J. Phys. Chem., 77 (18): 2196-2200, 1973.

[22] Rowlinson J.S., and Swinton F.L., Liquids and Liquid and Mixtures, 3nd ed. Butterworths, London,1982.

[23] Schneider G.M., In Chemical Thermodynamics, Vol. 2, McGlashan M.L. Ed., The chemical society, London, , Chapter 4, 1978.

[24] Gregorowicz J., de Loos Th., and de Swaan Arons J., Liquid-liquid-vapour Phase Equilibria in the System Ethane + propane + eicosane: Retrograde Behaviour of the Heavy Liquid Phase. Fluid Phase Equilibria. 84: 225-250, 1993.

[25] Robinson D. B., The Interface Between Theory and Experiment. Fluid Phase Equilibria. 52: 1-14, 1989.

[26] Boyle G.J., Retrograde Condensation from Lean Natural Gas, Paper Presented at the 2nd Conference on Natural Gas Research and Technology, Atlanta, Georgia, USA, 1972.

[27] Bergman D.F., Tek M.R. and Katz D.L., Retrograde Condensation in Natural Gas Pipelines, Project PR 26-69 of the Pipeline Research Committee, American Gas Association at the University of Michigan, Arlington, Virginia, USA, 1975.

[28] Katz D.L. and Kurata F., Retrograde Condensation, Ind. Eng. Chem. 32: 817-827, 1940.

[29] Kuenen J.P., Theorie der Vardampfung and verflussigung von Gemischen und der fraktionierten Destillation, Ed.: Barth, J.A., Leipzig, 1906.

[30] Van der Waals J.D. and Kohnstamm, P.H., Lehrbuch der Thermostatik, 2nd ed., Johann Ambrosius Barth, Leipzig, Germany,1927.

[31] Orr F.M. Jr. and Taber J.J., Displacement of Oil by Carbon Dioxide, Annual Report to the U.S. DOE Report No. DOE/BC/10331-4, 1981.

[32] Larsen L.L., Silva M.K., Taylor M.A., and Orr F.M., Temperature Dependence of LLV Behaviour in Carbon Dioxide/ Hydrocarbon System, SPE Reservoir Engineering, 105-114, 1989.

[33] Gregorowicz J., de Loos, Th., and de Swaan Arons J., Unusual Retrograde Condensation in Ternary Hydrocarbon Systems, Fluid Phase Equilibria , 73, 109-115, 1992a.

[34] Smits J.P., Master's Thesis, TU Delft, 1992.

[35] Cartlidge C.R., Automated Construction of Quartenary Phase Diagrams for Hydrocarbon Systems, Master's Thesis, University of Toronto, 1995.

[36] Mansoori G.A., Jiang S. T., Asphaltene Deposition and its Role in Petroleum Production and Processing, Kawanaka, Arabian J. Science & Engineering, 13, 17-34, 1988..

[37] Altamirano J.J., Flores M.A., Pie, O., Panivino, N., Arzate, C., Kapellmann, G., Lopez, M.T., Espinosa, and S., Rosales, S., Caracterization fisico-quimica de asfaltenos procedentes de loscrudos Maya e Itsmo, Revista del Instituto Mexicanodel Petroleo, 18, 32-44, abril-junio, 1986.

[38] Yen T.F., Multiple Structural Orders of Asphaltenes, Asphaltenes and Asphalt, 1. Developments in Petroleum Science,40. Edited by Yen T.F. and Chilingarian G.V., Elsevier Science B.V., 1994.

[39] Suzuki T., Ito Y., Takegami Y. and Watanabe Y., Chemical Structure of Tar-Sand Bitumens by 13C and 1H NMR Spectroscopy Mehtod, Fuel 61, 402-410, 1982.

[40] Speight J.G., The Stucture of Petroleum Asphaltenes-Current Concepts, Alberta Research Council, Information Series 81, 1978.

[41] Ali L.H., Method for the Calculation of Molecular Weights of Aromatic Compounds, and its Application to Petroleum Fractions, Fuel, 50, 298-307, 1971.

[42] Park S.J. and Mansoori G.A., Aggregation and Deposition of Heavy Organics in Petroleum Crudes, International Journal of Energy Sources, 10, 109-125, 1988.

[43] Kawanaka S., Park S.J., Mansoori G.A., Organic Deposition from Reservoir Fluids, SPE Reservoir Engineering Journal, 185-192, May 1991.

[44] Mansoori G.A., Modeling of asphaltene and other heavy organics depositions, J. Petroleum Science & Engineering, 17, 101-111, 1997.

[45] Koots J.A. and Speight J.G., Relation of Petroleum Resins to Asphalthenes, Fuel, 54, 179-184, 1975.

[46] Lambert M. C., Handbook of X-rays for Diffraction, Absorption and Microscopy, McGraw Hill, 1967.

[47] Dukhedin Lalla L., A Study of Complex Phase Behaviour Arising In Heavy Oil /Bitumen Mixtures Using X-ray Imaging, PhD thesis, University of Toronto, 1996.

[48] DE Bore D.K.G., Spectrochemica Acta, V. 44B, No. 11, PP. 1171-1190, 1989.

[49] Emmett F., Handbook of X-rays for Diffraction, Emission, Absorption, and Microscopy, McGraw Hill, Chapter 41, 1967.

[50] Dukhedin-Lalla L., Yushun S., Rahimi P. and Shaw J.M., "Phase Splitting of Complex Hydrocarbon Mixtures", Fluid Phase Equilibria, vol. 53, p.415-422, 1989.

[51] de Loos Th. W., van der Kooi H. J., and Ott P.L., Vapour-Liquid Critical Curve of the System ethane + 2-methylpropane, J Chem. Eng. Data, 31: 166-168, 1986.

[52] D.B. Robinson Design and Manufacturing Ltd., Operating and Maintenance Guide, 1997.

[53] Mazza A., G., Modelling of the Liquid-Phase Thermal Cracking Kinetics of Athabasca Bitumen and its Major Chemical Fractions, Ph.D. thesis, University of Toronto, 1987.

[54] Song F.M., Yang G.J., Han S.L., Huang Z.Q., and Qian J.L., Study of Coking Kinetics of Chinese Gudao Vacuum Residue, Fuel Science & Tchnology International, 13 (7), 819-835, 1995.

[55] Kajiwara K., Niki R., Urakawa H., Hiragi Y., Donkai N., and Nagura M, Micellar Structure of β-casein Observed by small-angle X-ray Scattering, Biochim. Biophys, Acta 955, 128-134, 1988.

[56]Tsonopoulos C., Heidman J.L., and Hwang S.C., "Thermodynamic and Transport Properties of Coal Liquids," John Wiley & Sons, Inc. 1986.

[57] Stamatakis S., Performance of Cubic EOS at High Pressures, International Conference, Poster # 9, Rueil-Malmaison, France, December 1997.

APPENDICES

Appendix A: Calibration

Density measurement Calibration for beryllium cell A

The density data that had been obtained in the past was found to have scatter. According to Dukhedin Lalla [47] all of the density data was bound by two curves (Figure A1). The upper bound was given by $y=-1.475x + 5.2186$ and the lower bound was given by $y=-1.606x + 6.158$. In an effort to account for the deviation, two ideas were considered. One of the first explanations considered was the notion that the recording equipment may not have been accurate enough. Thus, in an attempt to reduce the deviation and increase precision, improvements in the x-ray equipment and image analysis software were implemented. Another idea that was postulated was that the discrepancies may have been due to fluctuations coming from the x-ray source. The previous analysis method only involved taking one x-ray image measurement of a sample. One measured value in the presence of system fluctuations meant that the measured value obtained would also contain a large fluctuation. Thus, a modified analysis technique was devised. The modified analysis technique involved taking a series of 5 images at different time intervals for a specific substance and then averaging the values to account for the variability coming from the x-ray source. Experiments were performed on 14 different organic hydrocarbons using a glass cell. The data was then compiled and analyzed. The results are plotted on a semi-log graph of intensity versus the density of various hydrocarbons. The straight line profile exhibited by the different hydrocarbons indicated that a constant absorption coefficient, μ, was a valid assumption. Since the results were satisfactory, the experiments were repeated in the beryllium view cell. In all other respects the operating conditions were identical. Table A1 displays the data to determine a density intensity relationship and Figure A2 is plot of intensity versus density on semi-log plot. The plot demonstrates a linear relationship.

The calibration curve consisted of only 14 points. In order to verify that the straight line profile obtained from the organic hydrocarbon data was accurate enough to predict the density of any hydrocarbon based on the amount of x-rays that passed through the hydrocarbons more experiments were needed. A large library of video taped experiments, which were performed by Dukhedin-Lalla in an attempt to make a calibration curve were available. These video images were re-analyzed and used to confirm the new calibration curve using the new analysis technique. The videos contained lengthy recorded images of

various hydrocarbons (heavy oil system) at different temperatures, pressures, and densities. The videos of the different hydrocarbons were analyzed in the same manner as the 14 room temperature organic hydrocarbons used in the new calibration curve. The data from the hydrocarbons that were re-analyzed on the videos were listed in Tables A2 to A7 and Figures A3 and A4. The substances that were re-analyzed had experimental calculated values of density. The results confirm the assumption that μ remains constant for similarly structured hydrocarbons and further proved that the theoretical relationship that relates x-ray intensity to density was valid.

Table A1 Gray intensity versus density

	density	Ave. Intensity	Ln(intensity)
benzyl Alcohol	1.045	54.9	1.739
ethylbenzyl	0.865	63.2	1.800
methylbenzoate	1.086	53.9	1.731
dodecane	0.75	67.28	1.827
toluene	0.87	61.7	1.790
1-phenyldecane	0.85	63.32	1.801
heptane	0.68	70.01	1.845
hexadecane	0.77	65.38	1.815
o-xylene	0.9	61.9	1.791
decane	0.73	68.4	1.835
indene	0.994	57.75	1.761
pyridin	0.98	59.3	1.773
cyclohexaacetate	0.97	58	1.763
butylbenzene	0.86	60.7	1.783
decahydronaphthalene	0.88	63.3	1.801
cyclohexane	0.779	65.3	1.814

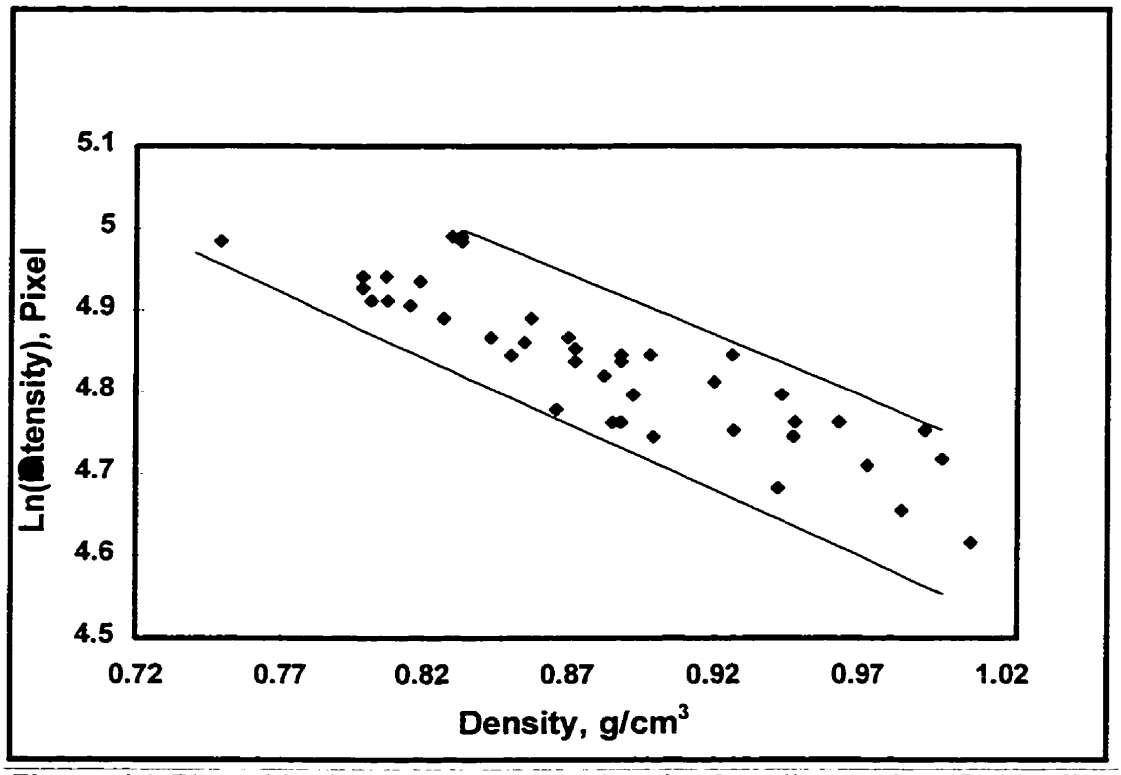

Figure A1 Plot of Ln(intensity) versus density for all samples (Dukhedin-Lalla)

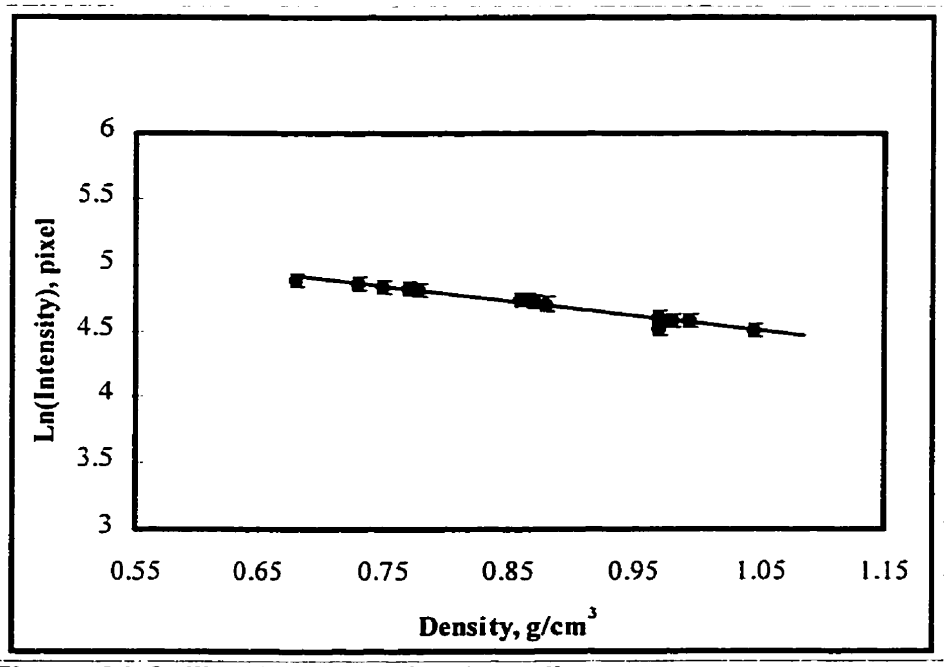

Figure A2 Calibration curve for the cell

Table A2 30g Athabasca Bitumen + 150 n-Dodecane + 1.9 MPa Hydrogen

Temperature (K)	Pressure (MPa)	Density (g/cm^3)	Intensity	Ln(Intensity)
298	1.90	0.79	89.5	4.81
339	2.10	0.75	93.8	4.85
400	2.48	0.73	96.2	4.88
494	3.17	0.69	99.7	4.91
530	3.48	0.68	101.7	4.93
561	3.86	0.67	107.1	4.98
587	4.21	0.67	104.2	4.96
611	4.55	0.68	101.1	4.93
630	4.86	0.69	100.8	4.92
648	5.17	0.74	92.5	4.84
698	6.27	0.87	79.9	4.69

Table A3 350g Athabasca Bitumen + 2.07 MPa Hydrogen

Temperature (K)	Pressure (MPa)	Density (g/cm^3)	Intensity	Ln(Intensity)
344	2.48	1.01	63.7	4.57
415	2.90	0.99	64.6	4.58
469	3.23	0.94	67.8	4.63
526	3.53	0.92	68.4	4.64
574	3.86	0.89	73.6	4.71
589	4.00	0.89	71.8	4.68
605	4.07	0.87	76.2	4.74
623	4.21	0.90	74.2	4.72
648	4.31	0.86	78.6	4.78
674	4.41	0.85	76.9	4.75

Table A4 285 ml CHNOO2 + 2.07 MPa Hydrogen

Temperature (K)	Pressure (MPa)	Density (g/cm^3)	Intensity	Ln(Intensity)
326	2.26	0.93	77.5	4.65
390	2.69	0.89	77.5	4.65
494	3.41	0.84	81.9	4.71
534	3.72	0.83	85.0	4.75
566	3.99	0.81	86.5	4.76
592	4.21	0.81	86.1	4.76
615	4.41	0.80	84.1	4.73
623	4.50	0.79	88.1	4.78

Table A5 75g Athabasca Bitumen + 150g n-Dodecane + 1.97 MPa Hydrogen

Temperature (K)	Pressure (MPa)	Density (g/cm^3)	Intensity	Ln(Intensity)
298	1.97	0.72	105.3	4.88
430	2.72	0.75	104.6	4.87
619	4.62	0.73	107.5	4.90
673	5.45	0.76	103.6	4.86
702	6.27	0.77	94.9	4.78

Table A6 187g Athabasca Bitumen + 112g n-Dodecane + 2.86 MPa Hydrogen

Temperature (K)	Pressure (MPa)	Density (g/cm^3)	Intensity	Ln(Intensity)
300	2.91	0.70	102.0	4.89
409	3.74	0.77	93.8	4.81
508	4.72	0.71	99.7	4.87
579	5.62	0.72	104.3	4.92

Table A7 150g GVR + 2.07 MPa Hydrogen

Temperature (K)	Pressure (MPa)	Density (g/cm^3)	Intensity	Ln(Intensity)
297	2.07	1.00	75.2	4.32
544	5.52	0.92	79.6	4.38
673	4.34	0.87	82.5	4.41

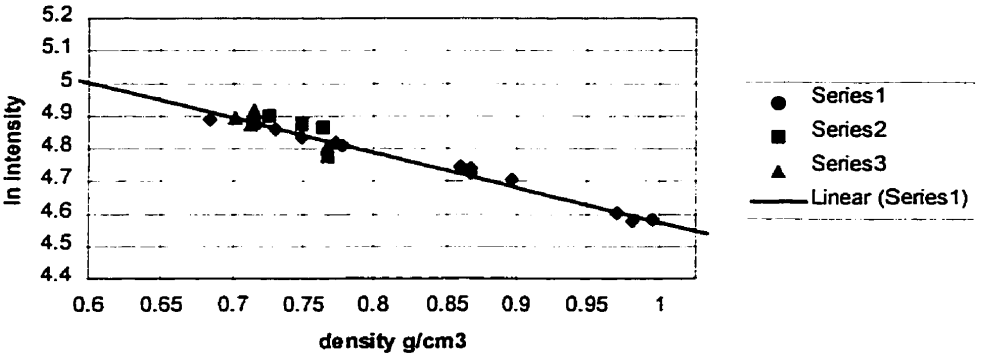

Figure A3 Series 1=calibration data ; Series 2= 75g ABVB ; Series 3= 187g ABVB; Series 5= 150g GVR

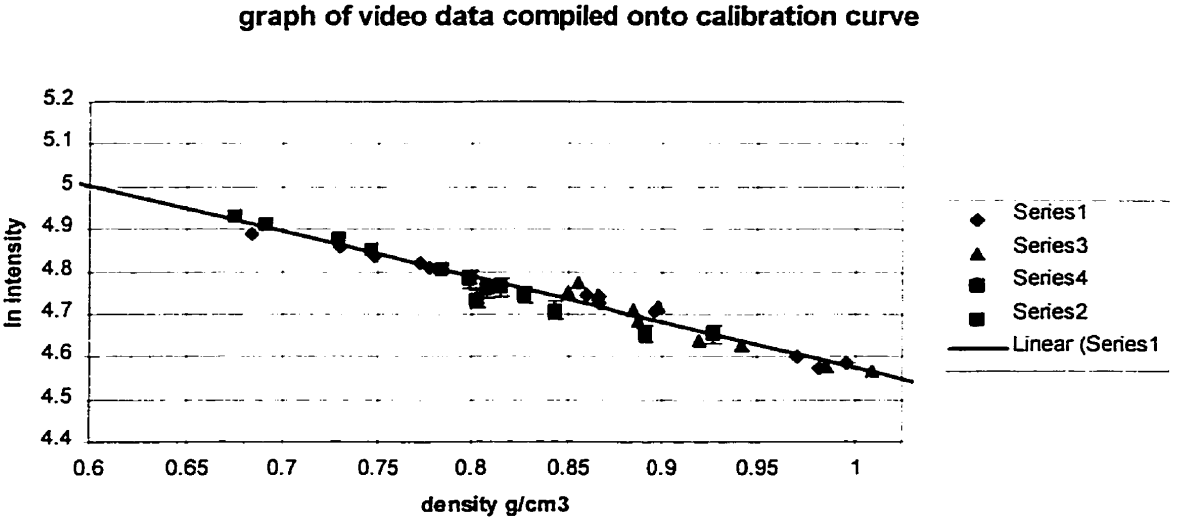

Figure A4 Series 1=calibration data ; Series 2= 30g ABVB ; Series 3= 350g ABVB; Series 5= 150g CHN002

Appendix B: Experimental Considerations

Calibration of the Pressure Transducer

The span and the zero of the pressure transducer output was adjusted using a hydraulic oil pressure tester. The hydraulic oil pressure tester was borrowed from the Department of Chemical Engineering Unit Operations Lab at the University of Toronto. The first thing that was done was to activate the pressure transducer conditioner-indicator. This was done because the unit needed to be running for approximately one hour before it would give stable readings. The pressure transducer was subsequently attached to the tester. The zero was then adjusted with no load acting on the transducer.

The adjustment of the span succeeded the zero. This was achieved by stacking enough weights on the piston to total 13.8 MPa. The weights had to be spun so that friction would not interfere with the reading. At this point the span was set. Thereafter, weights were taken off and a calibration curve constructed for the entire range between 0 and 13.8 MPa.

Temperature Measurement Precision

Since the pressures that were investigated with this apparatus ranged from 0.02-13.8 MPa, the error that an inaccurate temperature measurement would create was found to be significant. If the temperature measurement varied from the actual by ±1 °C, that variation would then have contributed approximately a 0.3% error in calculating the amount of hydrogen in the system (estimate of error based on Ideal Gas Law). Therefore, it was of the utmost importance to know the temperatures of the view cell as accurately as possible. This was accomplished using a thermocouple that had a precision of 0.1 °C. Separate measurements were made inside and outside the beryllium cell.

Pressure Measurement Precision

As previously mentioned the pressures ranged from 0.02 - 13.8 MPa. The pressure needed to be well known for each part of the experimental procedure because the calculations involving equations of state could only be as accurate as the pressure that was measured. The pressure transducer accuracy was quoted to be ± 0.01 MPa. Therefore, for an absolute pressure of 0.1 MPa, the error in the measurement is approximately 10% and for a pressure of

13.2 MPa the error is approximately 0.08%. To minimize this error the experiments were conducted through a full range of pressures with a larger concentration of readings at the 13.2 MPa range. Pressure was measured to ± 0.01 MPa with pressure transducers which were frequently calibrated against a dead-weight gauge.

Appendix C: Volume Calibration

Determination of Apparatus Volumes

The purpose of this part was to determine the volumes of various pieces of apparatus so that the amount of hydrogen added to the view cell could be calculated.

View Cell Volume Calibration -- Room Temperature Experiments

The 10 cc glass/stainless steel syringe was used as a weighing receptacle for the toluene that was to be injected into the topmost view cell port. The syringe was weighed when it was both full and empty during an injection. By filling up the reactor in this way the exact mass of toluene needed to fill the reactor was found by making a density calculation ($\rho_{toluene}$ =0.866) .

View cell Volume Calibration -- Image Analysis

A known mass of toluene was injected into the top port of the view cell with a syringe while the view cell was located inside the x-ray box in its frame. After the injection was made the valve was immediately closed. The image was then recorded on the VCR for approximately 2 minutes. This was repeated for each injection until there was a range of recordings that swept the entire height of the beryllium window with the corresponding mass measurements noted on the recording.

Fittings and Tubing Volume Calibration

The volumes of all other fittings and miscellaneous items were determined by the manufacturer's dimensions given in the manufacturer's catalogues except for the pressure transducer which was measured by the researcher. However, extra thought was needed with the NPT fittings because of the large volumes that they tended to hold inside them. To calculate this volume accurately the researcher measured the length of the male NPT end both before and after insertion into the female end. This procedure then enabled a new internal volume to be calculated for the female portion.

Volume Considerations

The stainless steel tubing and fittings which connect each of the main items in the apparatus were chosen to give the minimum volume because these fittings were subjected to temperature fluctuations within the room which heated or cooled the gas in those lines which then in turn affected the system pressure.

This problem was minimized by using 1/16" O.D. stainless steel tubing and 1/16" Swage-lok™ fittings whenever possible. The 1/16" tubing was the smallest sized tubing readily available and Swage-lok™ fittings have very small fluid volumes associated with them.

Beryllium Cell Ports

The small ports(~1/16") of the view cell created a problem consisting of slow and messy liquid filling. Therefore, a syringe with a needle tip was used to inject the liquid into the cell.

Appendix D: Assembly Instructions

Swage-lok™ Flaring

The Swage-lok™ flares are sealed correctly when the two machined surfaces sit properly. Flaring is relatively simple to perform and is best done with components set in their permanent location.

One first had to make sure that the ends of the piece of tubing that were to be used were debarred and filed smooth. If not the probability for a leak would have been very great at that joint. Second one had to insert the piece of tubing into the fitting which had both front and back ferrules already attached to it by a nut. Between the nut and the fitting (i.e. a tee or a male connector) there existed a front ferrule which was seated against the flared part of the fitting and a back ferrule which was seated onto the front ferrule and to the back of the nut. One had to then insert the tube into the orifice on the back end of the nut. As it is pushed it would slide through both ferrules. Thereafter, the nut needed to be rotated clockwise by a wrench. This work forced the ferrules to bite into the piece of tubing and prevented the piece of tubing from being removed from the nut and ferrules during disassembly.

After a significant amount of resistance is encountered you stop tightening the nut and check the connection with liquid leak detector.

Pipe Thread Connections

Pipe thread connections (otherwise known as NPT- national pipe thread) are sealed from the outside environment by a few threads of surface contact. Pipe thread is not the best type of sealing arrangement for this apparatus because it was not rated for as high pressures as were other types. Since NPT has been a common industrial choice the pressure transducer, cell, and rupture disc were all NPT. When the researcher worked with an NPT joint he always applied some pipe dope or Teflon tape to the male threads. After applying either sealant the researcher screwed the fitting in until the resistance to motion in the clockwise direction was significant. The joint was then leak tested.

Leak Testing

After pressurizing the system starting from a low pressure the researcher listened for any leaks and felt for any drafts. When a leak was found originating from a Swage-lok™ or a HIP fitting then the fitting was just tightened in position with a wrench with pressure still on the system. Once tightened, the fitting was sprayed with SNOOP (liquid leak detector) and it was monitored for any bubbles. If the leak was not stopped tightening, the researcher checked the flare for faultiness. If the leak originated from an NPT fitting, the researcher depressurized the system and checked for cross threading. If it was in working order it was then tightened and checked with SNOOP.

After all the leaks were fixed by checking every joint with SNOOP (when the system was pressurized to 6.6 MPa) the researcher pressurized the system to approximately 6.6 MPa. He then noted the time, temperature of the bulk gases, and the pressure of the system. If it held for 24 hours, it was deemed leak proof. If it did not, the researcher then isolated each section of the apparatus and tested each one individually. Anything that could not be fixed was replaced.

IMAGE EVALUATION
TEST TARGET (QA-3)

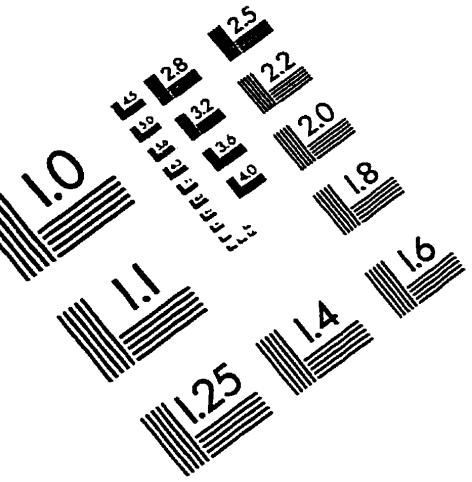

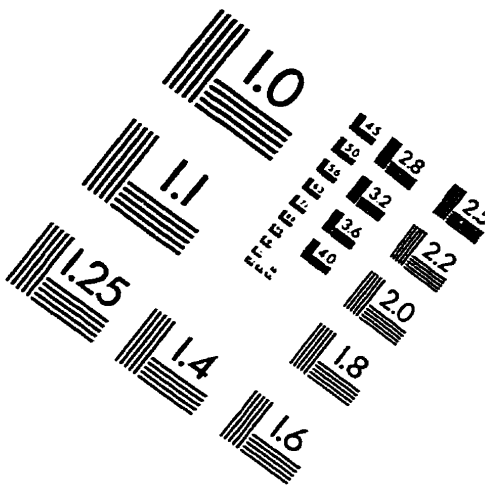

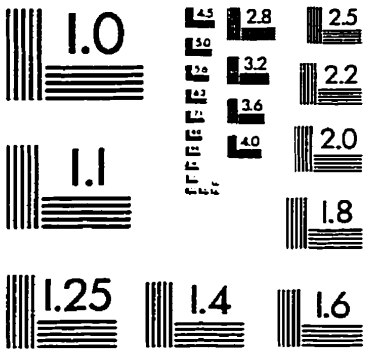

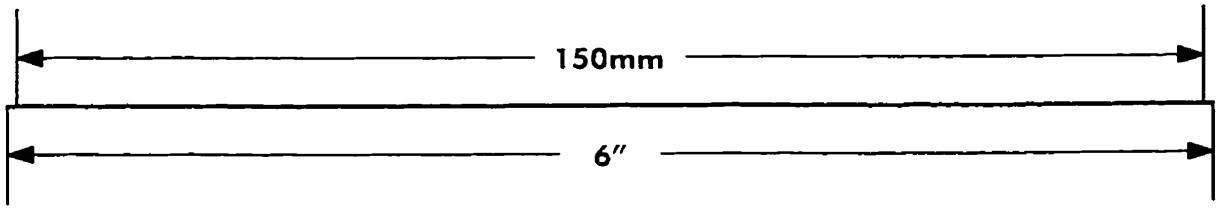

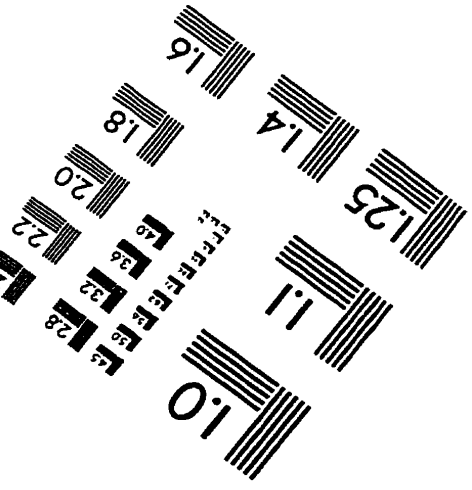

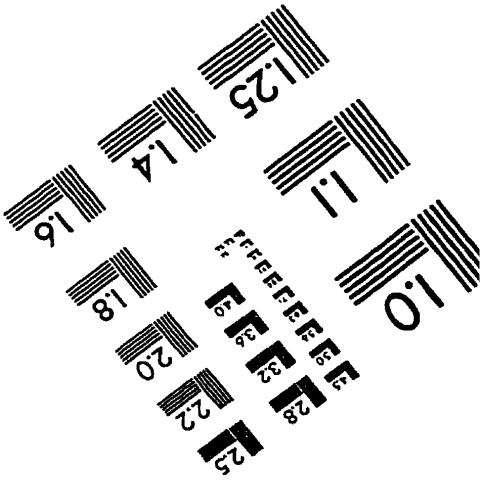

APPLIED IMAGE, Inc
1653 East Main Street
Rochester, NY 14609 USA
Phone: 716/482-0300
Fax: 716/288-5989